Research on Engineering Structures & Materials

Volume :4 Issue: 4
December 2018

p-ISSN: 2148-9807
e-ISSN: 2149-4088

R E S M

www.jresm.org

MIM RESEARCH GROUP

The International Journal of **Research on Engineering Structures and Materials (RESM)** is a peer-reviewed open access journal (p-ISSN: 2148-9807; o-ISSN: 2149-4088) published by MIM Research Group. It is published in February, June and September.

The main objective of RESM is to provide an International academic platform for researchers to share scientific results related to all aspects of mechanical, civil and material engineering areas.

RESM aims the publication of original research articles, reviews, short communications technical reports, and letters to the editor on the latest developments in the related fields.

All expenditures for the publication of the manuscripts are most kindly reimbursed by *MIM Research Group*. Thus, authors do not need to pay for publishing their studies in the journal.

The scope of the journal covers (but not limited to) behavior of structures, machines and mechanical systems, vibration, impact loadings and structural dynamics, mechanics of materials (elasticity, plasticity, fracture mechanics), material science (structure and properties of concrete, metals, ceramics, composites, plastics, wood, etc.,), nano-materials performances of new and existing buildings and other structural systems, design of buildings and other structural systems, seismic behavior of buildings and other structural systems, repair and strengthening of structural systems, case studies and failure of structural systems, safety and reliability in structural and material engineering, use of new and innovative materials and techniques in energy systems and mechanical aspects of biological systems (biomechanics and biomimetics).

The topics covered in RESM include:

- Structural Engineering
- Mechanical Engineering
- Material Engineering
- Earthquake Engineering
- Nano-technology
- Energy Systems

Abstracting and Indexing
Please visit http://www.jresm.org for more information.

Graphics and Design
Dr. H Ersen Balcioglu ersen.balcioglu@usak.edu.tr

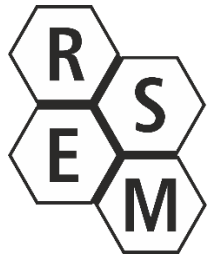

RESEARCH on ENGINEERING STRUCTURES & MATERIALS

Published by MIM Research Group

RESEARCH on ENGINEERING STRUCTURES & MATERIALS

Editorial Board

Editorial Office

Advisory Board Members

Irfan Ay	Balikesir University	Turkey
Fevzi Bedir	Gebze Technical University	Turkey
Tunde Bello-Ochende	Duke University	UK
Felipe Bertelli	Universidade Estadual de Campinas	Brazil
Alexei Biryukov	Donetsk National Technical University	Ukraine
Aslı Gunay Bulutsuz	Yıldız Technical University	Turkey
Şennur Candan	Bilecik University	Turkey
Habibe Demir	Iskenderun Technical University	Turkey
Ozgur Demircan	Ondokuz Mayıs University	Turkey
Nermin Demirkol	Kocaeli University	Turkey
Mehmet Emin Deniz	Batman University	Turkey
Sergey V. Dorozhkin	-	Russia
Elizaldo Domingues dos Santos	Universidade Federal do Rio Grande	Brazil
Erdogan Guk	Loughborough University	UK
Mehmet Gavgali	Atatürk University	Turkey
Gökhann Gece	Ankara University	Turkey
Khashayar Hosseinzadeh	Babol Noshirvani University	Iran
Serkan Islak	Kastamonu University	Turkey
Liércio AndreIsoldi	Universidade Federal do Rio Grande	Brazil
Mariatti Jaafar	Universiti Sains Malaysia	Malaysia
Draiche Kada	Universita Ibn Khaldoun de Tiaret	Algeria
Abdullah Cahit Karaoğlanlı	Bartın University	Turkey
Hamid Khan	National University of Computer and Emerging Sciences	Pakistan
K. Mahato	National Institute of Technology	India

Advisory Board Members

Upendra K. Mallela	Largy Services Limited	India
Faruk Mert	Gazi University	Turkey
V. Mohanavel	St. Peter's University	India
Sobhan Mosayebidorcheh	Babol Noshirvani University	Iran
Márcio Wrague Moura	Universidade Federal do Rio Grande	Brazil
Enea Mustafaraj	Epoka University	Albania
Seung Hoon Nahm	Center for Energy Materials Metrology	Republic of Korea
George Oguntala	University of Bradford	UK
Philip Oladijo	Botswana International University	Botswana
Serkan Özel	Bitlis Eren University	Turkey
Hayri Baytan Ozmen	Usak University	Turkey
Luiz Rocha	Universidade do Vale do Rio dos Sinos	Brazil
Binnur Sağbaş	Yıldız Technical University	Turkey
Gözde Sarı	Celal Bayar University	Turkey
Hakan Sarıkaya	Usak University	Turkey
Yakup Say	Munzur University	Turkey
Ramachandran Chidambaram Seshadri	Stony Brook University	USA
Mohsen Sheikholesmani	Babol Noshirvani University	Iran
Sushil Kumar Singh	Motilal Nehru National Institute of Technology	India
Faris Tarlochan	Qatar University	Qatar
Hamide Tekeli	Süleyman Demirel University	Turkey
Mehmet Topuz	Yüzüncü Yıl University	Turkey
Gül Tosun	Fırat University	Turkey

Advisory Board Members

Şaban Uysal	Karabük University	Turkey
Flavia Zinani	Universidade do Vale do Rio dos Sinos	Brazil

In This Issue

Research on Engineering Structures & Materials
MIM Reseach Group Publications
ISSN 2148-9807
http://www.jresm.org

Research on Engineering Structures & Materials
MIM Reseach Group Publications
ISSN 2148-9807
http://www.jresm.org

ABSTRACTING / INDEXING

The international journal of Research on Engineering Structures and Materials (RESM) is currently Absracted/Indexed by CrossRef, Google Scholar, Universal Impact Factor, Scientific Indexing Service, Research Bible, CiteFactor, Electronic Journal Library, Open Academic Journals Index, Global Impact Factor, Directory of Research Journals Indexing, Materials Science & Engineering Database (ProQuest) Engineering Journals (ProQuest), ULAKBİM TR Index (Tubitak) and under evaluation by many other respected indexes.

Research on
Engineering
Structures & Materials
journal homepage: http://jresm.org

RESEARCH GROUP

Research Article

Strength evaluation of a fire damaged concrete slab: combined correlation approach

Khaled Yaghi*, Housam Hammoud

Department of Civil & Environmental Engineering, American University of Beirut, Beirut, Lebanon

Article Info

Article history:
Received 27 Jan 2018
Revised 23 May 2018
Accepted 01 Jun 2018

Keywords:
Fire damaged concrete,
Strength evaluation,
Non-destructive testing,
Destructive testing,
porosity,
Pearson's correlation approach,
Combined correlation,
William's modification of the Hotelling test

Abstract

Strength evaluation of fire damaged concrete is not well studied although fire damaged concrete is encountered in many settings. There are limited studies that investigate the effect of physical properties on the strength of fire damaged concrete. In this paper, a fire damaged concrete slab element is evaluated based on non-destructive (rebound hammer and impact pulse velocity) and destructive (core and porosity) testing. Two correlation models are developed to assess the compressive strength of the slab element. The first model correlates the corrected core compressive strength to rebound number, impact pulse velocity and porosity. The second model correlates the corrected core compressive strength to rebound number and impact pulse velocity. Both correlation models are based on Pearson's statistical approach. The two correlations are compared based on William's modification of the Hotelling test and results indicate that rebound number, impact pulse velocity and porosity combined correlates more significantly to the corrected core compressive strength than rebound number and impact pulse velocity alone.

1. Introduction

Knowledge of the in-situ concrete properties is an important factor in understanding the integrity of a structural element in an existing or a newly constructed structure. Assessing the compressive strength property of concrete is important to decide on possible recommendations for repair or demolition and to design rehabilitation systems required to maintain the structural integrity of a structure [1].

Concrete strength is determined through various methods including non-destructive and destructive testing. Evaluating and assessing concrete compressive strength through correlations between non-destructive and destructive testing have been established by many previous researchers. Examples include works of [2], [3] and [4]. [2] provided a recommendation and guidance on the combination of different non-destructive and destructive tests in order to increase the accuracy of estimating the in-situ concrete strength. SONREB method was developed by RILEM Technical committee to establish a combination between rebound index and pulse velocity. This method was based on the application of a correction factor between a reference concrete (for calibration) and the concrete under test. A final calibration factor was calculated based on theoretical and

*Corresponding author: kry01@mail.aub.edu
DOI: http://dx.doi.org/10.17515/resm2018.40me0127
Res. Eng. Struct. Mat. Vol. 4 Iss. 4 (2018) 231-240

experimental data. It was concluded that the SONREB method is accurate as long as 90% of the values of the non-destructive test measurements conform to the destructive test measurements. [3] correlated Schmidt hammer testing and destructive core testing based on experimental results. Findings of [3] indicate that Schmidt hammer testing alone is not reliable for strength evaluation of concrete structures; correlations between Schmidt hammer and core testing is often required to make a sound evaluation. [4] correlated rebound hammer number, ultrasonic pulse velocity and core test based on Pearson's and Spearman's approaches, which gave good and reliable results.

Non-destructive tests are important methods to estimate concrete strength in fire damaged structures. This is attributed to the fact that fire damaged structures are structurally weak and minimal cores shall be taken in order not to diminish further the structural integrity of the structure under assessment. However; for fire damaged concrete, correlations between non-destructive tests and core tests alone does not provide reliable estimates of concrete strength; this is due to many other factors that can influence the strength of fire damaged concrete [2]. As concrete is exposed to fire, the percentage of voids increases and as a result the strength of concrete will decrease accordingly.

Examples of strength evaluation of fire damaged concrete include works of [5], [6], Dilek [7], [8] and [9]. [5] concluded that the properties of the constituent of material in RC beams, concrete and steel, progressively decrease by increasing temperature. [6] found that the shear strength of simply supported RC beams highly depends on the fire durations and thickness of concrete cover.

[7] assessed a fire damaged wall at the foundation level of a structure. The assessment included a non-destructive evaluation through ultrasonic pulse velocity test and several destructive core tests removed from the damaged wall. Dynamic Young's modulus and an air permeability index of 25 mm thick disks sawed from the cores were also determined and analysed. Non-destructive test results identified the presence of distressed layers of near-surface concrete, but could not provide information on the characteristics of these damaged layers. While destructive core testing did not identify the effects of the weakened layers of concrete. Loss of Young's modulus for the damaged layers of concrete was noticed in comparison to the Young's modulus of non-damaged concrete, and a significant increase in the air permeability of the fire exposed concrete surface was found. It was concluded that for thin layer damaged concrete core testing is not significant, while assessing dynamic modulus and air permeability index (API) tests proved to be more reliable.

[8] discussed a renewed version of hammer-drilling method to evaluate fire damaged concrete. This method was based on continuously monitoring the pulse transmission of the hammer-drill method to evaluate the mechanical properties of damaged concrete. The method analysed the amplitude of the reflected waves, which provides information on the local acoustic resistance of concrete, and calculates the time of flight of the pulses propagating from the tip of the drill-bit to a fixed ultrasonic receiver on the surface of the concrete member. It was concluded that amplitude of the transmitted pulse is strongly influenced by hard aggregate pebbles and is poorly sensitive to thermal damage which makes this parameter unsuited to this particular case. However, the velocity of the transmitted pulse was not influenced by coarse aggregate, and proved to be a sensitive indicator to the conditions of fire damaged concrete.

[9] addressed the effect of burning by fire flame on the behaviour and load capacity of rectangular reinforced concrete beams. Ultrasonic pulse velocity and rebound number tests were used to assess the impact of fire on the beams. Results showed reductions in

both ultrasonic pulse velocity and rebound number for beams, and that sudden cooling of concrete causes additional strength loss of concrete (air cooling vs water cooling). Experimental results also indicated that the crack width in concrete of fire damaged beam are higher than beams subjected to identical loads. Load deflection were more levelled signifying softer load-deflection behaviour than that of control beams, which were attributed to early cracks and low modulus of elasticity.

A thorough review of the literature indicates that strength evaluation of fire damaged concrete, which takes into account physical concrete properties, is not well studied although physical properties of concrete can highly influence the strength of fire damaged concrete. In this paper a correlation between porosity, impact pulse velocity, rebound number and core testing is established for fire damaged concrete slab and is statistically compared to the correlation excluding porosity. Correlation coefficients are calculated using Pearson's statistical approach.

2. Experimental

Slab element of a five-story residential structure that was subjected to an extensive fire, lasting for five hours, with a predicted maximum temperature of 500 °C, was studied. Destructive and non-destructive testing were recorded prior to demolition of the structure. Non-destructive tests included rebound hammer and impact pulse velocity, destructive tests included coring and porosity. Destructive tests consisted of the extraction of 30 cores from severally distributed points of the slab. Cores were tested in the laboratory for compressive strength and porosity. Non-destructive tests were carried out prior to the extraction of cores, and at the same locations of the extracted cores. Each non-destructive test was repeated at least twice to ensure repeatability and average values were reported.

2.1. Review of Destructive and Non-Destructive Testing Methods

Destructive and non-destructive testing methods for determining in-situ concrete strength are briefly presented. As well as the method for determining the percentage porosity of concrete.

Core testing is the most direct and accurate method in estimating the concrete strength in concrete structures. Core specimens are extracted from structural elements, and conditioned, then crushed to evaluate the compressive strength of the core. Before testing, cores are trimmed at the ends so that they are flat and perpendicular to the longitudinal axis of the core. The core ends are caped with a high alumina cement mortar, and tested in a dry state. Scatter in core test results can be found and is mainly attributed to variations in concrete characteristics and site stress distributions [4].

Rebound hammer test is the simplest way to estimate the concrete compressive strength. It is characterized by being the least expensive test, developing the smallest amount of structural damage, and practicality. Rebound hammer test only investigates the surface layer of concrete, and results might not represent the interior of the concrete. For that, rebound hammer is not an entirely accurate method. The surface of concrete is impacted by a steel hammer via a spring, and concrete compressive strength is estimated through the surface hardness rebound value. The amount of lost Kinetic energy during the impact of the steel hammer is measured, and this loss of energy is correlated with the strength and rigidity of concrete [10].

Impact pulse velocity test is used to determine the velocity of propagated waves along a known distance in a concrete specimen, two transducers are placed along that distance to calculate the velocity. The transducers are placed on opposite sides of the concrete element (direct transmission), adjacent sides of the concrete, or on the same face of the concrete element. For best results, the two transducers are place directly on opposite sides, so loss of sensitivity and accuracy is avoided. An appropriate coupling agent is placed on both the transducers face, and the concrete surface. The faces of the transducers are pressed firmly to the concrete surface until a stable transit time is displaced. The transit time is measured and the wave velocity is calculated. These values are used to correlate the properties of concrete through curves provided in the test device. Impact pulse velocity is affected by water/cement ratio, moisture content, presence of reinforcement, and cracks present in concrete.

Porosity test is used to calculate the percentage of voids present in a concrete specimen. Voids in fire damaged concrete occurs when water content reaches boiling point and evaporates through concrete, creating voids while escaping from entrapment. Percentage of voids increases proportionally with the increase in the exposure time of fire. Porosity index is an important factor to assess the degree of damage in a fire damaged structure.

2.2. Testing Program

Rebound hammer, impact pulse velocity, destructive core and porosity tests were carried out using instrumentation and testing procedures typically adopted in practice and following American Standard Testing Methods ([11], [12], [13], and [14] respectively).

Tests were carried out in severally distributed points along the slab. A reference grid system was created to uniformly distribute the testing locations on the slab. The grid system split the slab to 30 cells, and a grid naming was used to identify each test location as shown in Figure 1 below.

A precise survey was done using the ground penetrating radar test to locate the longitudinal and transverse reinforcing steel bars, before commencing with the tests. In this way, it was possible to avoid steel bars during core extraction.

Non-destructive rebound hammer test was carried out first, and ten readings were taken per cell. The mean rebound hammer value was recorded. Impact pulse velocity was measured for each cell, and a minimum of two readings were taken. The mean value of the two readings was recorded. One core was extracted from each cell (denoted by a black circle in Figure 1), and the compressive strength of each core was measured. Finally, porosity of each core was investigated by calculating the percentage of voids in the extracted core. Testing program is summarized in Table 1 below.

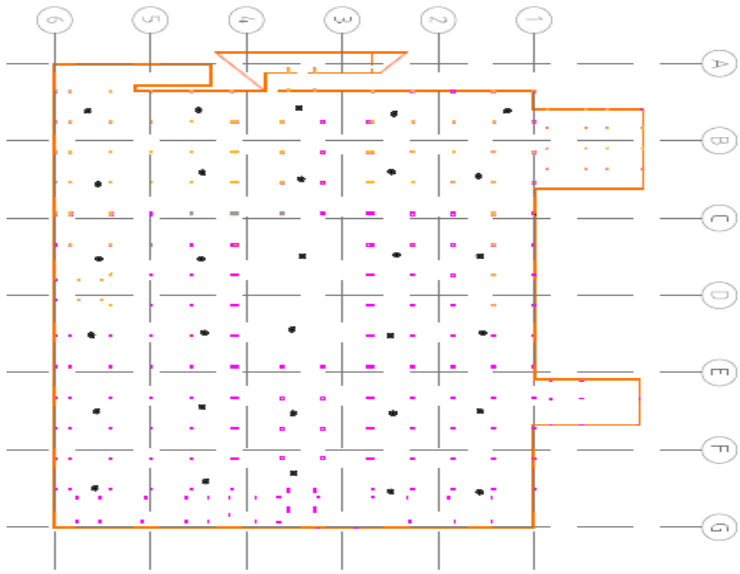

Fig. 1. Testing locations

Table 1. Testing program

Test	Number of Tests Performed
Core	30
Impact Pulse Velocity	30
Rebound Hammer	30
Porosity	30

2. Results and Analysis

Core compressive strength results were corrected to account for length to diameter ratio, diameter, moisture conditions and drilling factors, as per the recommendation of [15]. Extracted cores measured 10 cm in diameter and 20 cm in length and were soaked for 48 hours prior to crushing. Corrected core compressive strength values were calculated by multiplying each core compressive strength by a factor of 1.16. Non-destructive and destructive testing results are summarized in Table 2 below.

Coefficient of variation (CV) for each studied parameter was calculated. Higher CV values were found for the porosity parameter (27%) and rebound number (16%), while impact pulse velocity and core compressive strength returned lower values of CV (11% and 14% respectively). Usually it's normal to expect some scatter in the results taking into account the extent of fire reached to different parts of the slab, the within tests variability and the within member variability of concrete compressive strength. Overall variability of core compressive strength data is considered acceptable if compared to the value suggested by [15] of 13%.

Table 2. Destructive and non-destructive testing results

Grid	Corrected Core Compressive Strength (*MPa*)	Rebound Number	Impact Pulse Velocity (*km/s*)	Porosity
AB12	18.2	43	1.4	0.0773
AB23	24.1	49	1.6	0.053
AB34	21.2	38	1.34	0.0687
AB45	30.3	66	1.75	0.0211
AB56	24.5	50	1.55	0.0531
BC12	26.2	60	1.67	0.0413
BC23	19.4	47	1.3	0.0718
BC34	22.5	44	1.4	0.0698
BC45	26.1	56	1.39	0.0447
BC56	23.2	50	1.44	0.0616
CD12	22.7	57	1.4	0.0629
CD23	20.9	38	1.38	0.0773
CD34	24.6	59	1.53	0.0498
CD45	23.5	57	1.48	0.0564
CD56	27.1	44	1.35	0.0438
DE12	26.4	61	1.42	0.0438
DE23	19.4	38	1.2	0.0885
DE34	19.8	48	1.32	0.0902
DE45	22.3	50	1.52	0.0704
DE56	21.2	51	1.3	0.0773
EF12	18.7	45	1.22	0.0824
EF23	20.5	45	1.38	0.0768
EF34	24.2	39	1.67	0.0566
EF45	19.7	46	1.42	0.0777
EF56	25.3	52	1.76	0.0551
FG12	19.1	44	1.57	0.0655
FG23	22.9	45	1.45	0.0623
FG34	27.5	51	1.86	0.0444
FG45	24.2	53	1.54	0.0525
FG56	17.1	36	1.62	0.0919

Three graphs showing the relation of corrected core compressive strength, rebound number, impact pulse velocity and porosity respectively are shown in Figure 2 below.

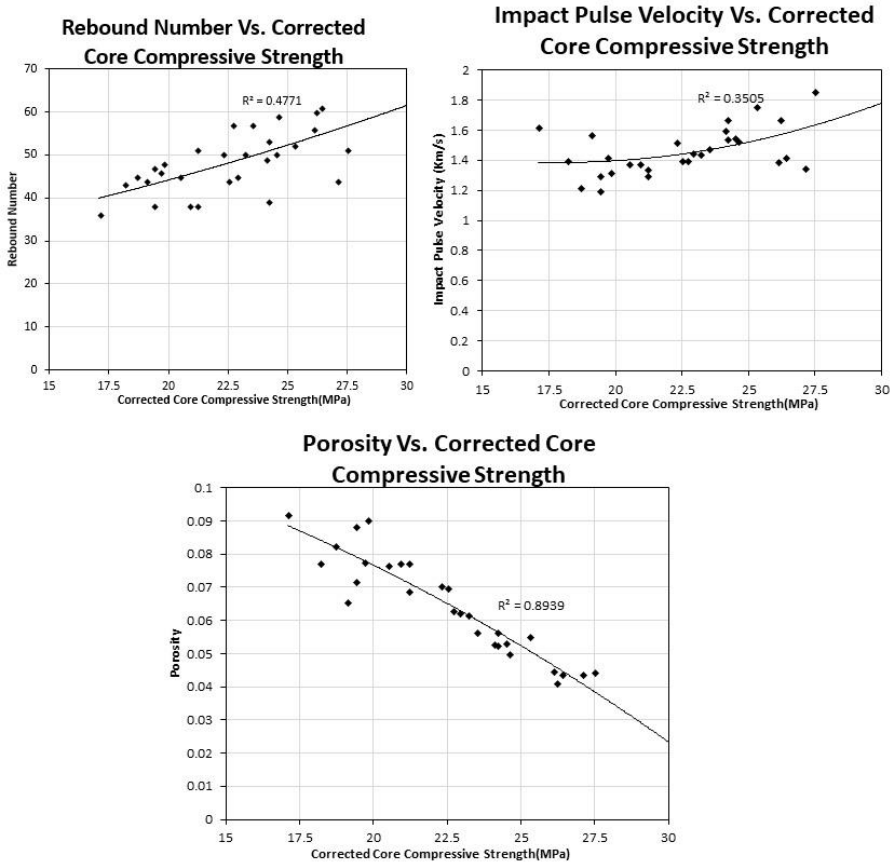

Fig. 2. Graphical representation of the results

2.1. Parson's Correlation Coefficients

To better assess the correlation between non-destructive and destructive test results, Pearson's correlation coefficients were determined. The aim is to find two relations between the studied variables in the forms:

$$f_c = a(RH)^b(V)^c(P)^d \quad (1)$$

$$f_c = a(RH)^b(V)^c \quad (2)$$

where: f_c – corrected core compressive strength; *a, b, c* and *d* – Pearson's correlation coefficients; *RH* – rebound number; *V* – impact pulse velocity; *P* – porosity.

Pearson's correlation coefficients along with some statistical parameters for the case including porosity in the correlation and the case excluding porosity from the correlation respectively are presented in Tables 3 and 4 below.

Table 3. Pearson's correlation coefficients (including porosity)

	Coefficients	Standard Error	t-Stat	P-Value	R square
a	5.6	0.31	5.48	9.32E(-6)	0.82
b	0.08	0.10	0.76	0.45	
c	0.03	0.13	0.22	0.83	
d	-0.38	0.06	-6.10	1.90E(-6)	

Table 4. Pearson's correlation coefficients (excluding porosity)

	Coefficients	Standard Error	t-stat	P-Value	R square
a	2.67	0.45	2.20	0.03	0.57
b	0.51	0.12	4.24	2.00E(-4)	
c	0.45	0.17	2.58	0.015	

It can be noted from Tables 3 and 4 above that statistical parameters vary widely between the two correlations. Standard error returned smaller values for the case including porosity in the correlation. P-values and t-stat parameter varied between coefficients of the two correlations. For instance, the intercept (a) in the correlation including porosity returned higher value of t-stat parameter and lower P-value than the intercept (a) in the correlation excluding porosity; whereas the rebound number coefficient (b) in the correlation including porosity returned a lower value of t-stat parameter and a higher P-value than the rebound number coefficient (b) in the correlation excluding porosity. Thus a general conclusion from the comparison of those statistical parameters cannot be made. The correlation including porosity returned higher R-square value (0.82) than the correlation excluding porosity (0.57). However; conclusions about the better correlation cannot be made by directly comparing R-square values.

2.2. Statistical Comparison Between the Two Correlations

Direct comparison between statistical parameters may not be always indicative on whether two correlations are significantly different from one another or not. To test whether the two correlations are significantly different, the correlations are transformed using William's modification of the Hotelling test with a significance level of 0.05. The r value is distributed as t with $(n-3)$ degrees of freedom [16]. The following null hypothesis is tested,

H_0: The correlation including porosity as a parameter in evaluating strength of fire damaged concrete is the same as the correlation excluding porosity. Results of William's modification of the Hotelling test are summarized in Table 5 below.

Table 5. Williams modification of the Hotelling test

r_{1-2}	r_{2-3}	r_{1-3}	t(n-3)	Critical t value at 0.05 significance level
0.8	0.75	0.91	1.96	1.7

where: r_{1-2} – correlation between porosity, rebound number and impact pulse velocity ; r_{2-3} – correlation between corrected core compressive strength, rebound number and impact pulse velocity; r_{1-3} – correlation between corrected core compressive strength, rebound number, impact pulse velocity and porosity; $t(n-3)$ – William's modification parameter.

Results of the Williams modification of the Hotelling test indicate that William's modification parameter is statistically significant at a 0.05 significance level. Thus the null hypothesis should be rejected and the correlations are significantly different at a 0.05 significance level. It can be concluded that, rebound number, impact pulse velocity and porosity combined correlate more significantly to the corrected concrete compressive strength of a fire damaged slab than rebound number and impact pulse velocity combined alone.

Conclusions

In this paper two strength evaluation models for a fire damaged concrete slab were studied. Strength evaluation models were based on correlations between non-destructive (rebound hammer and impact pulse velocity) and destructive (core and porosity) tests. The correlation coefficients were calculated using Pearson's correlation approach. A statistical comparison of the two correlations was conducted using William's modification of the Hotelling test. Based on the experimental findings the following conclusions could be made:

- Comparison between the strength evaluation models indicates that the two models are statistically different and the correlation model which includes porosity as a parameter to evaluate the strength of fire damaged concrete correlates more significantly to the corrected core compressive strength.
- Correlations between non-destructive and core testing alone may not be reliable in strength evaluation of fire damaged concrete.
- Introducing physical properties of concrete, such a porosity, may help increasing reliability of strength assessment of fire damaged concrete.

It should be noted that all correlations and analyses conducted in this paper are based on the destructive and non-destructive testing results conducted on a specific slab element of a five-story residential building that was subjected to an extensive fire. As a result, correlation models and results presented pertain to this structural element and may not be directly applicable to other fire damaged structural elements. However; findings and conclusions may be indicative on the general effect of physical properties of concrete, such as porosity, on the strength evaluation of fire damaged concrete.

References

[1] Yaghi, K.; Hammoud, H. Estimation of the design concrete strength from core tests: modified tolerance factor approach. J. International Journal of Engineering Research and Technology, 2016; 5(1).

[2] RILEM Draft Recommendation. Draft recommendation for in situ concrete strength determination by combined non-destructive methods. Materials and Structures, 1993; 26 : 43- 49. https://doi.org/10.1007/BF02472237

[3] Aydin, F.; Saribiyik, M. Correlation between Schmidt hammer and destructive compression testing for concretes in existing buildings. J. Scientific Research and Essays, 2010 5(13): 1644- 1648.

[4] Masi, A.; Chiauzzi, I. An experimental study on the within-member variability of in situ concrete strength in RC building structures. J. Construction and Building Materials, 2013; 47: 951- 961. https://doi.org/10.1016/j.conbuildmat.2013.05.102
[5] Cruz, C.R. Elastic properties of concrete at high temperature. J. PCA Res. Dev. Lab, 1996; 8: 37-45.
[6] El-Hawari, M.M.; Ragab, A.M.; El-Azim, A.A.; Elibiari, S. Effect of fire on shear behavior of RC beams. J. Appl. Fire Sci, 1997;65(2): 281- 287.
[7] Dilek, U. Assessment of fire damage to a reinforced concrete structure during construction. J. Performance of Constructed Facilities, 2007; 21 (4): 257-263. https://doi.org/10.1061/(ASCE)0887-3828(2007)21:4(257)
[8] Felicetti, R. Assessment of fire damaged concrete via the hammer-drill pulse transmission technique. 2013 RILEM Bookseries 6: 205- 212. https://doi.org/10.1007/978-94-007-0723-8_30
[9] Kadhum, M.M. Fire resistance reinforced concrete rigid beams. J. Civil Engineering and Construction Technology. 2014;5 (5): 35-48.
[10] Liu, J.C.; Sue, M.L.; Kou, C.H. Estimating the surface of concrete using surface rebound value and design parameters of concrete materials. Tamkang Journal of Science and Engineering, 2009; 12 (1): 1-7.
[11] ASTM. Test method for rebound number of hardened concrete. ASTM C805-02.
[12] ASTM. Standard test method for pulse velocity through concrete. ASTM C597-02.
[13] ASTM. Standard test method for obtaining and testing drilled cores and sawed beams of concrete. ASTM C42-03.
[14] ASTM. Test method for density, absorption, and voids in hardened concrete. ASTM C642-97.
[15] ACI Committee 214. Guide for obtaining core and interpreting compressive strength results (ACI 214.4R-10), American Concrete Institute.
[16] Kenny, D. Correlation and causality. Revised ed. Virginia Carrow: Storrs, Connecticut. 2004.

Research on Engineering Structures & Materials
journal homepage: http://jresm.org
Research Group

Research Article

Strength reduction factors for existing mid-rise RC buildings for different performance levels

Hayri Baytan Ozmen*[1], Mehmet Inel[2]

[1]*Department of Civil Engineering, Usak University, 64200 Usak, Turkey*
[2]*Department of Civil Engineering, Pamukkale University, 20070 Denizli, Turkey*

Article Info

Article history:
Received 31 Jul 2018
Revised 29 Sep 2018
Accepted 22 Oct 2018

Keywords:
Ductility,
Overstrength,
Reinforced concrete,
Response modification factor,
Response reduction factor,
Site class

Abstract

Many earthquake prone countries have significant amount of existing deficient buildings to be evaluated for seismic actions. Although nonlinear methods are more preferable for assessment of existing buildings, most of the practicing engineers are unfamiliar to these methods. Therefore, linear methods seem to be in use in the near future for assessment of great number of deficient existing buildings in a reasonable time. In linear methods, nonlinear behaviour is taken into account by a single parameter: strength reduction factor (R) which is used to greatly reduce the elastic force demand accounting for the nonlinear behaviour. This study evaluates the use of R factors for different ductility and performance levels of buildings with respect to different soil site class. It is observed that the R factors: decrease with increasing periods, are more sensitive for higher performance levels, may change more than 30% with respect to number of story or transverse reinforcement amount, and may change 20% depending on the site class. However, effect of site class is generally smaller and a clear trend is not observed. Exemplary R values for different ductility, performance levels and number of stories are provided in the study.

1. Introduction

Although nonlinear methods capture the real behaviour of structures better than linear ones, their use is somewhat limited due to additional modelling work. Most of practicing civil engineers in many countries are lack of the required knowledge about nonlinear principles. Therefore, elastic methods do not seem to be fully replaced by nonlinear ones in the close future. In elastic methods, nonlinear behaviour is taken into account by a single parameter: "strength reduction factor (R)" [1]. Thus this parameter has a critical role for the proper evaluation of buildings. In building codes, some values of the R factors are given for certain classes of structures but they are meant to be for new construction [2-5]. Such R factors may not be suitable for evaluation of deficient existing buildings with elastic methods. This study examines R factors to be used for existing mid-rise reinforced concrete buildings which are thought to be the major portion of the building stock under risk in developing countries. Turkey is selected to represent the developing countries. Eleven 4-story and eleven 7-story buildings are modelled with features common in Turkish building stock. The buildings reflect existing deficiencies in the building stock [6]. All buildings are modelled with two different transverse steel amounts accounting for seismic detailing to evaluate buildings with different ductility levels. Capacity curves of the building models are obtained by nonlinear static analyses. Displacement capacities at Immediate Occupancy (IO), Life Safety (LS) and Collapse Prevention (CP) performance

*Corresponding author: baytan.ozmen@usak.edu.tr
DOI: http://dx.doi.org/10.17515/resm2018.60ea3107

levels are determined. The "Equivalent" Single-Degree-Of-Freedom (SDOF) system models obtained from capacity curves are subjected to acceleration records of 83 different earthquakes, approximately 20 records for each of the USGS site classification to determine seismic demands [7]. Based on the obtained data, R values for different performance levels are suggested for existing buildings. This study is useful for better understanding R factors and proper elastic modelling of existing buildings for seismic assessment.

2. Strength Reduction Factor

Because of the economical and functional reasons, nearly all buildings are built to behave nonlinearly during the design seismic event. The static lateral force method accounts for nonlinear response of the structures by the use of "strength reduction factors" (R), which is also known as "response modification factor" [4, 5, 8, 9]. The elastic base shear demand ratio obtained from 5% damped acceleration response spectrum (C_e) are divided by R factor to greatly reduce the force demands to obtain design base shear force ratio (C_b) (Fig. 1, Eq. 1).

$$C_b = \frac{C_e}{R} \tag{1}$$

The commentary to the NEHRP Recommended Provisions describes the R factor as "an empirical response modification (reduction) factor intended to account for both damping and ductility inherent in a structural system at displacements great enough to approach the maximum displacement of the system [10]. Strength reduction factor is the most important factor in design or evaluation of the buildings using elastic methods since no other parameter affects the base shear demand as much as R. Therefore, proper selection of R factor has a key role in proper seismic assessment.

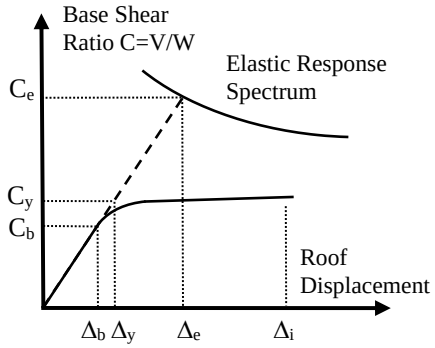

Fig. 1 Typical base shear ratio-roof displacement relationship

2.1. Components of R Factor

Since the reasons to use R factor are based on different phenomenon, the R factor has different components. Based on experimental data Uang and Bertero [11], Whittaker et. al. [12] described R factor as the product of three factors that accounted for over strength, ductility and damping:

$$R = R_o R_\mu R_\xi \tag{2}$$

In Eq. 2 R_o is over strength factor, R_μ is ductility factor and R_ξ is damping factor. Using data from earthquake simulation tests, the over strength factor (R_o) is calculated to be yield

base shear ratio (C_y) divided by design base shear ratio (C_b), ductility factor is the base shear ratio required for elastic response (C_e) divided by yield base shear ratio (C_y), and the damping factor was set to unity. In a later document a formulation for R is proposed [9] as:

$$R = R_o R_\mu R_R \tag{3}$$

The formulation given in Eq. 3 is same as the Eq. 2 (when R_ξ is 1.0) except the redundancy factor (R_R). This factor is intended to reflect the effects of redundancy of the structure such as structural indeterminacy and improved reliability due to multiple lines of load carrying mechanisms.

The proposed formulations do not specifically address the effects of plan and vertical irregularity in framing systems. Whittaker et al. [1] states that irregularity could be addressed by reducing the response modification factor by a regularity factor. EC8 reduces the behaviour factors by 20% for irregular buildings [3].

As seen above different formulations of R factor has been proposed in literature. This study concentrates on the over strength and ductility factors and assumes R is the product of these factors as given in Eq. 3 with R_R is equal to unity.

Although many studies are available about R factors, limited research has been done concerning R factors for different performance levels and soil site classifications. As reported by other researchers, local construction practices significantly affect R values [1]. Therefore, additional studies are important to better establish these factors for regions with varying construction practices. This paper focuses on the over strength and ductility factors for the existing buildings with different ductility classes and for different performance levels, and variation of these factors according to different soil site classification.

2.1.1 Over Strength Factor

The yield lateral strength of a building (V_y) generally exceeds its design lateral strength (V_b) because components are likely to be designed with capacities significantly greater than the design requirements, material strengths generally exceed specified nominal strengths, and displacement and detailing requirements often force the use of stronger components than that necessary for strength alone. For a structural system, over strength factor (R_o) vary as a function of seismic zone and building period [13]. Buildings located in different seismic zones will have different values of over strength due to the different ratio of gravity loads to seismic loads which results in values depending on seismic zones for the strength factor. Differences in local construction practices may also significantly affect the strength factor value [1].

Freeman [14] estimated strength factors of approximately 2.8 and 4.8 for four story and seven-story reinforced concrete moment frames, respectively. Uang and Maarouf [15] analyzed a six-story reinforced concrete perimeter moment frame building shaken by the 1989 Loma Prieta earthquake. The strength factor reported for the building is 1.9. Hwang and Shinozuka [16] studied a four-story reinforced concrete intermediate moment frame building located in seismic zone 2 as per the Uniform Building Code. The building has determined to have a strength factor of 2.2 if no limits to the damage to the structural system is imposed. Whittaker et al. [1] stated that the scatter in the reported values for the strength factor is significant.

For multistory multibay frames, overstrength factor is specified in EC8 as 1.30 [3]. ASCE7 gives an overstrength ratio of 3.0 for RC framed structures [2]. However, this ratio is intended for finding design forces in the members. Therefore, it is given as higher for

conservative purposes and does not conform to the logic of overstrength factor in scope of the study.

Mondal et al. [17] investigated the R factors of RC moment frame buildings designed and detailed following the Indian standards for ductile detailing at two performance levels. They reported overstrength factors of 2.70, 2.64, 2.39 and 2.26 for 2, 4, 8 and 12 story buildings based on fundamental mode shape lateral load distribution.

2.1.2 Ductility Factor

The ductility factor (R_μ) is a measure of the global nonlinear response of a structural system due to its plastic deformation capacity. It is measured as the ratio of the base shear considering an elastic response (V_e) / base shear considering an inelastic response (V_y). It is assumed that the elastic force demand on the system (V_e) can be reduced by the factor R_μ owing to the inelastic displacement capacity available with the system. In the last decades, significant studies have been conducted to investigate the ductility factor based on SDOF systems [18-22]. These relationships are based on statistical behaviour of inelastic SDOF systems under strong motion (with 5% damping) on rock or stiff soil.

EC8 gives behaviour factor as 3.0 and 4.5 times the overstrength ratio for medium and high ductility class buildings, respectively [3]. Therefore, these values may be assumed as suggested ductility factors. Mondal et al. [17] in the above mentioned study determined 2.01 and 2.05 ductility factors for 4 and 8 story RC buildings for a limit state based on ATC 40 Structural Stability level [23]. For another limit state based on element plastic rotation capacities, the figures are 2.32 and 2.51, respectively.

Nishanth et al. [13] examined the response reduction factors for moment resisting RC frames designed according to Indian codes. When their reported values for different seismic zones are averaged, the ductility factors for high ductility 4, 7, 10, 13, 16 story buildings are 1.76, 3.03, 3.73, 3.53, 2.95, respectively. Corresponding values for buildings with moderate ductility are 1.73, 2.71, 3.11, 2.75, 2.20. They concluded that the values of R as given by the codes are of higher degree.

2.1.3 Damping Factor

The damping factor (R_ξ) accounts for the effect of supplementary viscous damping and is mainly significant for structures with special energy dissipating devices. Without these devices, the damping factor is generally assigned a value equal to unity and not considered in the determination of the response reduction factor for the force-based evaluation [1, 24]. Since there are no energy dissipating devices in the considered models the R_ξ is taken as 1.0 in scope of the study.

2.1.4 Redundancy Factor

A redundant seismic structural system is composed of multiple vertical lines of lateral load resisting frames, which transfers earthquake-induced forces to the foundation. As there are generally multiple lines of frames in RC structural systems, they usually fell in the category of redundant structural systems. For redundant systems, the lateral load is shared by different frames depending on the relative stiffness and strength characteristics of each frame. Frames aligned in the same direction, form a redundant parallel system. Therefore, the reliability of the system will be higher than the reliability of individual frames of the structural system. If the frames are identical, the reliability will be equal to that of a single frame as they will fail simultaneously. If the frame properties are uncorrelated, the resulting system reliability will be higher. Four lines of strength and stiffness compatible vertical seismic framing in each principal direction of a building have been recommended as the minimum necessary for adequate redundancy [25, 26]. Whittaker et al. [1] gives exemplary values for R_R as 0.71, 0.86 and 1.0 for systems with 2, 3 and 4 lines of vertical

seismic framing, respectively. As there are more than 4 lines of framing in each direction of the considered models and due to the suggestion of ASCE7, R_R is taken as 1.0 in this study [2]. More information can be found in literature about redundancy factor [27-31].

3. Building Models

The major portion of the building stock in many developing countries are consists of deficient mid-rise reinforced concrete buildings [6]. In scope of the study, existing mid-rise reinforced concrete buildings inferior to code requirements are investigated. Two sets of RC buildings 4-story and 7-story are selected to represent mid-rise buildings located in the high seismicity region of Turkey (design ground acceleration of 0.4g). There are eleven buildings in each set. The selected buildings are typical beam-column RC frame buildings with no shear walls (Fig. 2). Since the majority of buildings in Turkey were constructed according to 1975 Turkish Earthquake Code [32], the 4- and 7-story buildings are designed according this code considering both gravity and seismic loads. Soil site class Z3 that is similar to class C soil of FEMA 356 (2000) is assumed [33]. Material properties are assumed to be 16 MPa for the concrete compressive strength and 220 MPa for the yield strength of both longitudinal and transverse reinforcement [6]. Strain-hardening of longitudinal reinforcement has been taken into account and the ultimate strength of the reinforcement is taken as 330 MPa.

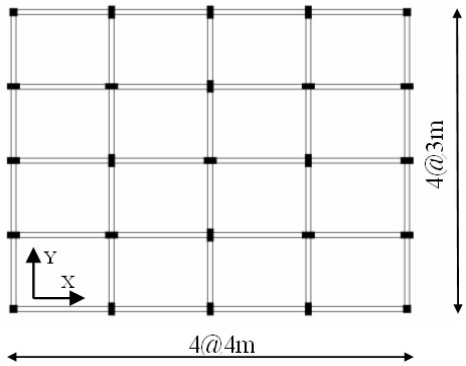

Fig. 2 Plan view of reference 4- and 7- story buildings

One of the important deficiencies in the existing building stock is the insufficient amount of transverse reinforcement. The transverse reinforcement amount may be considered to represent construction and workmanship quality or compliance to the code, since closer spacing of transverse reinforcement shows that the structure has ductile detailing and is code compliant and/or has better construction and workmanship quality [34]. Two different spacings are considered as 100 mm and 200 mm to investigate R factors of the buildings with different ductility classes [6]. More info about building models can be found at the study by Inel et al. [35].

3.1 Modelling Approach

Nonlinear static analyses have been performed using SAP2000 Nonlinear that is a general-purpose structural analysis program [36]. Three-dimensional model of each structure is created in SAP2000 to carry out nonlinear static analysis. Beam and column elements are modelled as nonlinear frame elements with lumped plasticity by defining plastic hinges at both ends of beams and columns. SAP2000 implements the plastic hinge properties

described in ATC 40 [23] or FEMA 356 [33]. As shown in Fig. 3, five points labelled A, B, C, D, and E define force-deformation behaviour of a plastic hinge.

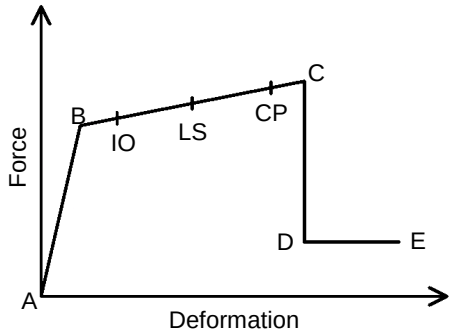

Fig. 3 Force-Deformation relationship of a typical plastic hinge

The definition of user-defined hinge properties requires moment–curvature analysis of each element. Modified Kent and Park model [37] for unconfined and confined concrete and typical steel stress–strain model with strain hardening (Mander [38]) for steel are implemented in moment–curvature analyses. The points B and C on Fig. 2 are related to yield and ultimate curvatures. The point B is obtained from SAP2000 using approximate component initial effective stiffness values as per TEC 2007 [4]; 0.4EI for beams and values depending on axial load level for columns as given in Eq. 4.

$$\begin{array}{ll} 0.4EI & for \quad N/(A_c \text{ x } f_c) \le 0.1 \\ (0.4+4/3\cdot(N/(A_c \text{ x } f_c)-0.1))EI & for\ 0.1 < N/(A_c \text{ x } f_c) < 0.4 \\ 0.8EI & for \quad N/(A_c \text{ x } f_c) \ge 0.4 \end{array} \tag{4}$$

fc is concrete compressive strength, N is axial load, A_c is area of section. For the $N/(A_c \text{ x } f_c)$ values between 0.1 and 0.4 linear interpolation is made.

The ultimate curvature is defined as the smallest of the curvatures corresponding to (1) a reduced moment equal to 80% of maximum moment, determined from the moment-curvature analysis, (2) the extreme compression fiber reaching the ultimate concrete compressive strain as determined using the relation provided by Priestley et al. [39], given in Eq. 5, and (3) the longitudinal steel reaching a tensile strain of 50% of ultimate strain capacity that corresponds to the monotonic fracture strain. Ultimate concrete compressive strain is given as:

$$\varepsilon_{cu} = 0.004 + \frac{1.4\rho_s f_{yh}\varepsilon_{su}}{f_{cc}} \tag{5}$$

where ε_{cu} is the ultimate concrete compressive strain, ε_{su} is the steel strain at maximum tensile stress, ρ_s is the volumetric ratio of confining steel, f_{yh} is the yield strength of transverse reinforcement, and f_{cc} is the peak confined concrete compressive strength.

The input required for SAP2000 is moment-rotation relationship instead of moment-curvature. Also, moment rotation data have been reduced to five-point input that brings some inevitable simplifications. Plastic hinge length is used to obtain ultimate rotation values from the ultimate curvatures. Several plastic hinge lengths have been proposed in the literature [39, 40]. In this study plastic hinge length definition given in Eq. 6 which is proposed by Priestley et al. [39] is used.

$$L_p = 0.08L + 0.022\, f_{yh} d_{bl} \geq 0.044\, f_{yh} d_{bl} \quad (6)$$

In Eq. 6, L_p is the plastic hinge length, L is the distance from the critical section of the plastic hinge to the point of contraflexure, d_{bl} is the diameter of longitudinal reinforcement.

Following the determination of the ultimate rotation capacity of an element, acceptance criteria are defined as labelled IO, LS, and CP on Fig. 2. IO, LS, and CP stand for Immediate Occupancy, Life Safety, and Collapse Prevention, respectively. This study defines these three points corresponding to 10%, 60%, and 90% use of plastic hinge deformation capacity [41]. In existing reinforced concrete buildings, especially with low concrete strength and/or insufficient amount of transverse steel, shear failures of members should be taken into consideration. For this purpose, shear hinges are introduced for beams and columns. Because of brittle failure of concrete in shear, no ductility is considered for this type of hinges. Shear hinge properties are defined such that when the shear force in the member reaches its strength, member fails immediately. The shear strength of each member is calculated according to TS 500 [42] that is similar to UBC 1997 [5].

Effect of infill walls are modelled through diagonal struts as suggested in TEC 2007 [4] and FEMA 356 [33]. Nonlinear behaviour of infill walls is reflected by assigned axial load plastic hinges on diagonal struts whose characteristics are determined as given in FEMA 356 [33]. Material properties are taken from TEC 2007 [4] to reflect characteristics of infill walls in Turkey; 1000 MPa, 1 MPa and 0.15 MPa were assumed as modulus of elasticity, compressive strength and shear strength values, respectively.

Reference 7 story model is composed of 200 nodes, 483 RC frame members, 168 infill wall elements and 910 plastic hinges. Reference 4 story model is composed of 125 nodes, 276 RC frame members, 96 infill wall elements and 520 plastic hinges. The given number of nodes are for the points where different members are connected. Note that the software further divides the frames to increase accuracy, if needed.

Range of some important properties of the building models is given in Table 1. Further information about building models and behaviour can be found in the study by Inel et al. [35]. Views of the reference 7 story models are given in Fig. 4. The infill wall elements are not included to in Fig. 4b decrease the complexity of the view.

Table 1 Natural period, weight and strength coefficient ranges of 4- and 7-story buildings

N	Period Range (s)	Seismic Weight Range (kN)	Yield Base Shear Ratio (V_y/W)
4	0.47-1.10	8456-10163	0.11-0.25
7	0.74-1.32	2912-20277	0.11-0.18

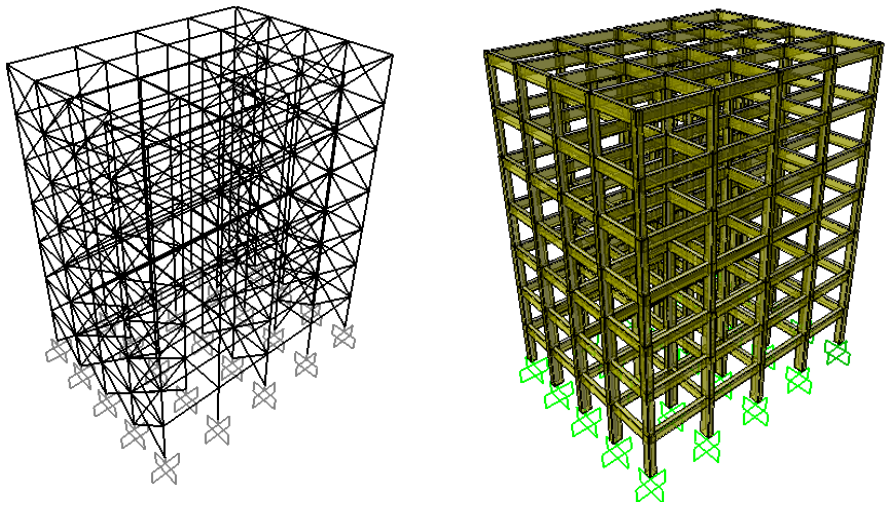

a) Wire frame view of the model

b) View of the model with 3D members (infill walls not visible)

Fig. 4 Views of the 7 story model

3.2 Nonlinear Static Analyses

In order to obtain capacity curves and displacement ductility (maximum roof displacement at which performance criteria still satisfied over yield roof displacement) values of the building models, nonlinear static analyses are carried out. The lateral forces applied at center of mass were proportional to the product of mass and the first mode shape amplitude at each story level under consideration. P-Delta effects were taken into account. Example capacity curves are provided in Fig. 5 for one of the 4-story models for 100 and 200 mm transverse reinforcement spacing. The vertical axis plots shear strength coefficient that is the base shear normalized by seismic building weight. The horizontal axis plots global displacement drift that is lateral displacement of building at the roof level normalized by building height. The figure indicates significant effect of transverse reinforcement spacing on displacement capacity.

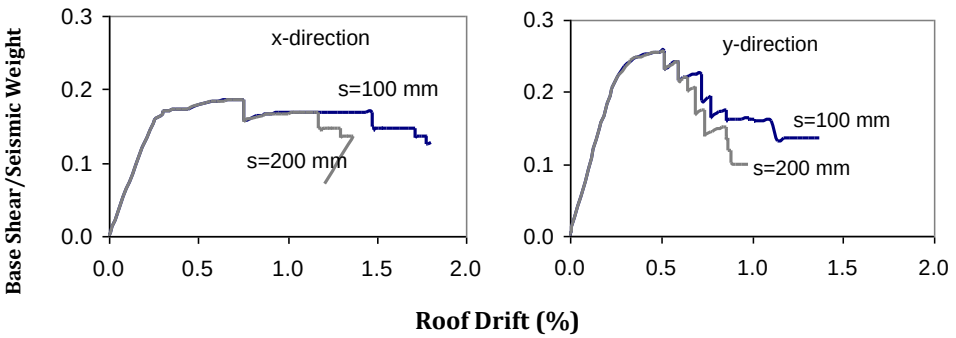

Fig. 5 Example capacity curves of reference 4-story building for 100 and 200mm transverse reinforcement spacing.

3.3 Performance Evaluation

Performance evaluation of the investigated buildings is conducted using Turkish Earthquake Code [4]. Three levels, Immediate Occupancy (IO), Life Safety (LS), and Collapse Prevention (CP) are considered as specified in this code and several other international guidelines [23, 33]. Criteria given in the code for three performance levels are listed in Table 2.

Table 2 Performance levels and criteria provided in Turkish Earthquake Code [4]

Performance Level	Performance Criteria
Immediate Occupancy (IO)	1. There shall not be any column or shear walls beyond IO level. 2. The ratio of beams in IO-LS region shall not exceed 10% in any story. 3. There shall not be any beams beyond LS.
Life Safety (LS)	1. In any story, the shear carried by columns or shear walls in LS-CP region shall not exceed 20% of story shear. This ratio can be taken as 40% for roof story. 2. In any story, the shear carried by columns or shear walls yielded at both ends shall not exceed 30% of story shear. 3. The ratio of beams in LS-CP region shall not exceed 20% in any story.
Collapse Prevention (CP)	1. In any story, the shear carried by columns or shear walls beyond CP region shall not exceed 20% of story shear. This ratio can be taken as 40% for roof story. 2. In any story, the shear carried by columns or shear walls yielded at both ends shall not exceed 30% of story shear. 3. The ratio of beams beyond CP region shall not exceed 20% in any story.

4. Nonlinear Response History Analyses

The capacity curve of each building obtained from pushover analysis was approximated with a bilinear curve using guidelines given in ATC 40 [23] and FEMA 440 [43] and reduced to equivalent SDOF systems. Then these SDOF systems are subjected to nonlinear response history analysis by using ground motion record sets. Earthquake records with different characteristics may significantly affect the results of analyses [44, 45]. In this study USGS soil site classification based on the average shear wave velocity to a depth of 30 m is used [7]. Site class A is the stiffest type with a shear wave velocity higher than 750 m/s, and D is the weakest site with a shear wave velocity lower than 180 m/s. The site B has a shear wave velocity between 750 m/s and 360 m/s whereas site C has a shear wave velocity between 360 m/s and 180 m/s. Four site classifications include 83 different records, approximately 20 records for each site class. All earthquake records are taken from PEER website [46]. Average values for some properties of selected ground motion records are given in Table 3.

Table 3 Average values for some properties of used ground motion records

Site class	Number of records	Magnitude	PGA (g)	PGV (m/s)	PGD (m)
A	20	7.00	0.40	0.30	0.11
B	23	6.71	0.39	0.36	0.11
C	20	7.02	0.40	0.43	0.19
D	20	7.05	0.26	0.36	0.20

5. Analyses Results

Displacement capacities of the buildings are evaluated for IO, LS and CP performance levels using nonlinear static analyses and criteria given in TEC 2007. Displacement ductilities are calculated dividing displacement capacities by yield displacement. Using response history analyses with the given displacement ductilities, R_μ of the building models are determined. Total of 88 capacity curves (eleven 4- and eleven 7 story buildings, two principal directions and 2 transverse reinforcement spacing) are analyzed for 83 acceleration records. Table 4 lists average values for yield base shear strength ratio (C_y), design base shear ratio (C_b), over strength factor (R_o), and ductility ratio (R_μ) for different performance levels, site class and transverse reinforcement spacing. Note that due to contribution of walls to the lateral strength, C_y values given in table may seem to be high for existing pre-modern code buildings.

Table 4 Average C_y, C_b values and R factors for different site class, spacing, performance level

Story	C_y	C_b	R_o	Site Class	R_μ						Exemplary R (R_o.R_μ) Values					
					IO		LS		CP		IO		LS		CP	
					s1	s2	s1	s2	s1	s2	s1	s2	s1	s2	s1	s2
4	0.16	0.11	1.45	A	1.18	1.15	2.36	1.62	3.59	2.81	1.7		3.6	2.4	5.5	4.2
				B	1.19	1.15	2.59	1.69	4.02	3.04						
				C	1.19	1.15	2.55	1.69	3.83	2.96						
				D	1.20	1.15	2.42	1.67	3.61	2.82						
7	0.14	0.09	1.57	A	1.10	1.03	1.63	1.34	2.51	1.92	1.7	1.6	2.7	2.1	4.4	3.2
				B	1.11	1.03	1.78	1.39	2.96	2.15						
				C	1.11	1.03	1.80	1.40	3.04	2.16						
				D	1.10	1.03	1.65	1.34	2.66	1.98						

Note: s1= s100 mm, s2= s200 mm

Base shear demands are calculated according to TEC 2007 [4]. Note that since the yield strength of the buildings is not significantly affected by amount of transverse reinforcement, C_y is given independent of transverse reinforcement. The change of C_y, R_o and R_μ and R values for CP performance level and 100 mm transverse reinforcement spacing with building period are given in Fig. 6. Similar trends are observed for all the other performance levels and transverse reinforcement spacing.

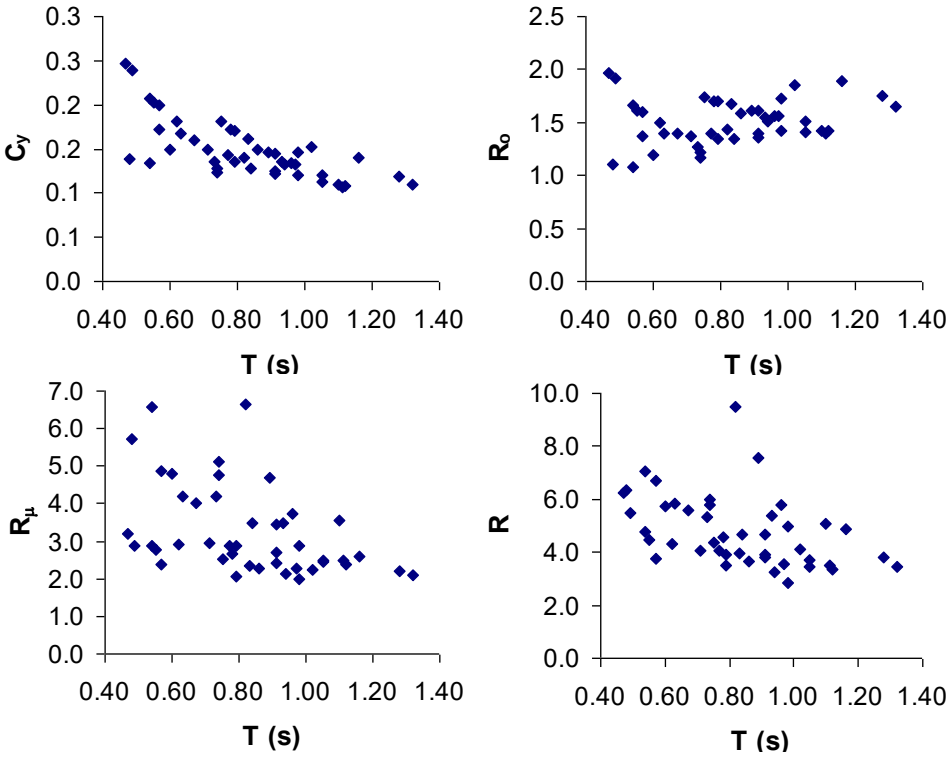

Fig. 6 Relationship of C_y, R_o, R_μ and R with period (for Collapse Prevention and s100 mm)

5. Conclusions

Total of 88 capacity curves of 22 buildings (eleven 4- and eleven 7 story buildings, two principal directions and 2 transverse reinforcement spacing) are used to examine R factors for existing buildings. Three different performance levels and 83 ground motion records of four different site classes are considered. Based on 21912 nonlinear response history results the following observations are made.

- Average yield base shear strength ratio of 4-story buildings are higher than that of 7-story ones. It is observed that C_y values become lower as the period gets higher (Fig. 6), as observed by other studies [47-49].
- Although 4-story buildings have higher yield base shear strength ratio, average over strength factor of 7-story buildings are higher than 4-story ones (Table 4). This can be explained by lower design base shear demands of 7-story buildings with higher periods located at descending branch of code spectrums. In scope of the building models of this study R_o values seem to scatter around 1.5 (Fig. 6). It is notable that 1.5 is the value implicitly used for overstrength in TEC 2007 Section 2.5 [4].
- All average ductility factors of 7-story buildings are lower than corresponding ductility factors of 4-story buildings (Table 4). This shows that as the number of story or period increases the ductility and ductility factors decreases (Fig. 6) as pointed out by other researchers [47, 48] and indicated by observed wide spread damage of higher buildings compared to lower ones after earthquakes [50-53].

- Even if R_o values are higher for 7-story buildings, R factors are lower than that of 4-story buildings, because higher R_o values are not enough to compensate the insufficiency in ductility factors. R also seems to be decreasing with increasing period. (Table 4, Fig. 6).
- IO level is just at the beginning of inelastic behaviour. Since R_μ is a factor regarding inelasticity, it does not change by the amount of transverse reinforcement for IO level.
- The effect of transverse reinforcement amount on the ductility ratio is significant for LS and CP levels (Table 4). The difference in ductility ratio of 100 mm and 200 mm transverse reinforcement spacing is up to 33% depending on performance levels and number of stories. This is in compliance with the findings of an experimental study by Rizwan et al. [54], which reports reductions of R values by 40 to 60% due to construction defects.
- Even if it is not accounted in the codes, or in many other studies in literature, site class may affect R values as observed by other researchers [22]. The dependence is more evident for higher performance levels (CP). Up to 20% difference in the average values of Rμ is observed (Table 4). However, in general the differences are smaller and a clear trend is not observed.
- Examples of R values for evaluation of existing buildings are provided in Table 4 for general use.

References

[1] Whittaker A, Hart G, Rojahn C. Seismic response modification factors. Journal of Structural Engineering ASCE, 1999; 125(4):438 – 44. https://doi.org/10.1061/(ASCE)0733-9445(1999)125:4(438)
[2] ASCE SEI/ASCE 7-05. Minimum design loads for buildings and other structures. Reston (USA): American Society of Civil Engineers; 2005.
[3] CEN Eurocode 8. Design Provisions for earthquake resistance of structures (European Prestandard ENV 1998). Brussels (Belgium): Comité Européen de Normalisation; 2004.
[4] Turkish Earthquake Code (TEC). Specifications for buildings to be built in seismic areas, Ministry of Public Works and Settlement, Ankara, Turkey, 2007.
[5] UBC, Uniform Building Code, Int. Conf. of Building Officials, Whittier, Calif, USA, 1997.
[6] Ozmen HB, Inel M, Senel SM and Kayhan AH. Load carrying system characteristics of existing Turkish RC building stock. International Journal of Civil Engineering, 2015;13(1): 76 – 91.
[7] USGS. www.usgs.gov, 2015
[8] ATC. Tentative provisions for the development of seismic regulations for buildings, Rep. No. ATC-3-06, Applied Technology Council, Redwood City, Calif, USA, 1978.
[9] ATC. Structural response modification factors, Rep. No. ATC-19, Applied Technology Council, Redwood City, Calif, USA, 1995.
[10] Federal Emergency Management Agency (FEMA). NEHRP recommended provisions for seismic regulations for new buildings. Rep. FEMA 302, Washington, D.C., 1997.
[11] Uang CM and Bertero VV. Earthquake simulation tests and associated studies of a 0.3-scale model of a six-story concentrically braced steel structure. Rep. No. UCB/EERC-86/10, University of California, Berkeley, Calif, 1986.
[12] Whittaker AS, Uang CM and Bertero VV. Earthquake simulation tests and associated studies of a 0.3-scale model of a six story eccentrically braced steel structure. Rep. No. UCB/EERC-87/02, University of California, Berkeley, Calif, 1987.
[13] Nishanth M, Visuvasam J, Simon J, Packiaraj JS. Assessment of seismic response reduction factor for moment resisting RC frames. IOP Conference Series: Materials Science and Engineering, 263 (3), art. no. 032034, 2017. https://doi.org/10.1088/1757-899X/263/3/032034

[14] Freeman SA. On the correlation of code forces to earthquake demands. Proc., 4th U.S.-Japan Workshop on Improvement of Build. Struct. Des. and Constr. Practices, Applied Technology Council, Redwood City, Calif, 1990.
[15] Uang CM and Maarouf A. Safety and economy considerations of UBC seismic force reduction factors. Proc., 1993 National Earthquake Conf., Central United States Earthquake Consortium, Memphis, 1993; 121–130.
[16] Hwang H and Shinozuka M. Effect of large earthquakes on the design of buildings in eastern United States. Proc., 5th U.S. National Conf. on Earthquake Eng., Earthquake Engineering Research Institute, Oakland, Calif., 1994; 223–231.
[17] Mondal A, Ghosh S & Reddy GR. Performance-based evaluation of the response reduction factor for ductile RC frames. Engineering Structures, 2013; 56: 1808 – 1819. https://doi.org/10.1016/j.engstruct.2013.07.038
[18] Newmark N, Hall W. Earthquake spectra and design. Engineering monograph; Earthquake Engineering Research Institute, Berkeley, California, 1982.
[19] Riddell R, Newmark N. Statistical analysis of the response of nonlinear systems subjected to earthquakes. Structural research series no. 468; Dept. of Civil Engineering, University of Illinois; Urbana, USA, 1979.
[20] Vidic T, Fajfar P, Fischinger M. A procedure for determining consistent inelastic design spectra. In: Nonlinear seismic analysis of reinforced concrete buildings, New York, USA; 1992.
[21] Krawinkler H, Nassar A. Seismic design based on ductility and cumulative damage demands and capacities. In: Nonlinear seismic analysis of reinforced concrete buildings, New York, USA; 1992; 27–47.
[22] Miranda E, Bertero V. Evaluation of strength reduction for earthquake resistant design. Earthquake Spectra, 1994; 10(2): 357 – 79. https://doi.org/10.1193/1.1585778
[23] ATC. Seismic evaluation and retrofit of concrete buildings, Rep. No. ATC-40, Applied Technology Council, Redwood City, California, 1996.
[24] Borzi B, Elnashai AS. Refined force reduction factors for seismic design. Engineering Structures, 2000;22(10): 1244 –1260. https://doi.org/10.1016/S0141-0296(99)00075-9
[25] Bertero VV. Evaluation of response reduction factors recommended by ATC and SEAOC. Proc., 3rd U.S. National Conf. on Earthquake Engineering, Earthquake Engineering Research Institute, Oakland, Calif., 1986: 1663 – 1673.
[26] Whittaker AS, Uang CM and Bertero VV. An experimental study of the behavior of dual steel systems. Rep. No. UCB/ EERC-88/14, University of California, Berkeley, Calif, 1990.
[27] ATC. A critical review of current approaches to earthquake-resistant design, Rep. No. ATC-34, Applied Technology Council, Redwood City, Calif, 1995.
[28] Husain M and Tsopelas P. Measures of structural redundancy in R/C buildings. I: Redundancy indices. Journal of Structural Engineering ASCE, 2004; 130(11): 1651 – 1658. https://doi.org/10.1061/(ASCE)0733-9445(2004)130:11(1651)
[29] Tena-Colunga A, and Cortés-Benítez JA. Assessment of redundancy factors for the seismic design of special moment resisting reinforced concrete frames. Latin American Journal of Solids and Structures, 2015; 12(12): 2330 – 2350. https://doi.org/10.1590/1679-78251800
[30] Zhu B and Frangopol DM. Effects of post-failure material behaviour on redundancy factor for design of structural components in nondeterministic systems. Structure and Infrastructure Engineering, 2015; 11(4): 466 – 485. https://doi.org/10.1080/15732479.2014.951864

[31] Abdi H, Hejazi F, Jaafar MS and Karim IA. Evaluation of response modification factor for steel structures with soft story retrofitted by viscous damper device, Advances in Structural Engineering, 2016; 19(8): 1275-1288. https://doi.org/10.1177/1369433216642036
[32] Turkish Earthquake Code (TEC). Specifications for buildings to be built in seismic areas. Ministry of Public Works and Settlement, Ankara, Turkey, 1975.
[33] FEMA 356. Prestandard and commentary for seismic rehabilitation of buildings, Federal Emergency Management Agency, Washington, D.C., 2000.
[34] Ozmen HB and Inel M. Effect of rapid screening parameters on seismic performance of RC buildings. Structural Engineering and Mechanics, 2017; 62(4): 391-399. https://doi.org/10.12989/sem.2017.62.4.391
[35] Inel M, Ozmen HB and Bilgin H. Re-evaluation of building damages during recent earthquakes in Turkey. Engineering Structures, 2008; 30: 412-427. https://doi.org/10.1016/j.engstruct.2007.04.012
[36] SAP2000, Computers and Structures Inc. Integrated finite element analysis and design of structures basic analysis reference manual. Berkeley (CA, USA).
[37] Scott BD, Park R, Priestley MJN. Stress–strain behavior of concrete confined by overlapping hoops at low and high strain rates. ACI Structural Journal, 1982; 76(1): 13–27.
[38] Mander JB (1984). Seismic design of bridge piers. Ph.D. Dissertation, University of Canterbury, New Zealand.
[39] Priestley MJN, Seible F and Calvi GMS. Seismic Design and Retrofit of Bridges, John Wiley & Sons, New York, 1996. https://doi.org/10.1002/9780470172858
[40] Park R and Paulay T. Reinforced Concrete Structures, John Wiley & Sons, New York, 1975. https://doi.org/10.1002/9780470172834
[41] Inel M, Bilgin H and Ozmen HB. Seismic capacity evaluation of school buildings in Turkey. Proceedings of The Institution of Civil Engineers-Structures and Buildings, 2008; 161(3): 147-159. https://doi.org/10.1680/stbu.2008.161.3.147
[42] TS500. Design and construction specifications for reinforced concrete structures, Turkish Standards Institute, Ankara, Turkey, 2000.
[43] FEMA 440. Improvement of nonlinear static seismic analysis procedures, Federal Emergency Management Agency, Washington, D.C., 2005.
[44] Ozdemir G, Bayhan B. Response of an isolated structure with deteriorating hysteretic isolator model. Research on Engineering Structures and Materials, 2015; 1: 1–10. https://doi.org/10.17515/resm2014.01st1216
[45] Demirtas B, Bayraktar A, Dumanoglu A. Model updating effects on the seismic behavior of tall buildings under far and near-fault ground motions. Research on Engineering Structures and Materials, 2017; 3(2): 99 – 112
[46] PEER. Pacific Earthquake Engineering Research Center, http://peer.berkeley.edu/ 2015
[47] Akkar S, Sucuoglu H, Yakut A. Displacement based fragility functions for low- and mid-rise ordinary concrete buildings. Earthquake Spectra, 2005; 21(4): 901-927. https://doi.org/10.1193/1.2084232
[48] Ozcebe G. Seismic assessment and rehabilitation of existing buildings, Tubitak Research Report. No: ICTAG YMAU I574, Ankara, Turkey, 2004.
[49] Khoshnoudian F, Ahmadi E, Kiani M and Hadikhan Tehrani M. Collapse capacity of soil-structure systems under pulse-like earthquakes, Earthquake Engineering & Structural Dynamics, 2015; 44(3): 481-490. https://doi.org/10.1002/eqe.2501
[50] Dogangun A. Performance of reinforced concrete buildings during the May 1 2003 Bingöl earthquake in Turkey. Engineering Structures, 2004; 26: 841-856. https://doi.org/10.1016/j.engstruct.2004.02.005
[51] Sezen H, Whittaker AS, Elwood KJ and Mosalam KW. Performance of reinforced concrete buildings during the August 17, 1999 Kocaeli, Turkey earthquake, and the

seismic design and construction practice in Turkey. Engineering Structures, 2003; 25: 103–114.https://doi.org/10.1016/S0141-0296(02)00121-9
[52] Ozhendekci N and Ozhendekci D. Rapid seismic vulnerability assessment of low-to mid-rise reinforced concrete buildings using Bingöl's regional data, Earthquake Spectra, 2012; 28(3): 1165-1187. https://doi.org/10.1193/1.4000065
[53] Ozmen HB, Inel M. Akyol E, Cayci BT & Un H. Evaluations on the relation of RC building damages with structural parameters after May 19, 2011 Simav (Turkey) earthquake. Natural hazards, 2014; 71(1): 63-84.https://doi.org/10.1007/s11069-013-0900-y
[54] Rizwan M, Ahmad N, Khan AN. Seismic performance of compliant and noncompliant special moment-resisting reinforced concrete frames. ACI Structural Journal, 2018; 115 (4): 1063-1073. https://doi.org/10.14359/51702063

Research on
Engineering
Structures & Materials
journal homepage: http://jresm.org

RESEARCH
GROUP

Research Article

Magnetohydrodynamic squeezing flow of casson nanofluid between two parallel plates in a porous medium using method of matched asymptotic expansion

M. G. Sobamowo

Department of Mechanical Engineering, University of Lagos, Akoka, Lagos, Nigeria

Article Info

Article history:
Received 15 Mar 2018
Revised 11 Apr 2018
Accepted 03 May 2018

Keywords:

Casson fluid, Squeezing flow,
Nanofluid,
Magnetic field, Parallel plates,
Method of Matched Asymptotic Expansion

Abstract

In this paper, unsteady squeezing flow of Casson nanofluid between two parallel plates embedded in a porous medium and subjected to magnetic field is analyzed. The developed systems of partial differential equations for the fluid flow models are converted to ordinary differential equations through suitable similarity variables. The obtained ordinary differential equation is solved using method of matched asymptotic expansion. The accuracies of the approximate analytical method for the small and large values of squeezing numbers are investigated. Good agreements are established between the results of the approximate analytical method and the results numerical method using fourth-fifth order Runge-Kutta-Fehlberg method. Thereafter, the developed approximate analytical solutions are used to investigate the effects of pertinent flow parameters on the squeezing flow phenomena of the nanofluids between the two moving parallel plates. The results established that the as the squeezing number and magnetic field parameters decreases, the flow velocity increases when the plates come together. Also, the velocity of the nanofluids further decreases as the magnetic field parameter increases when the plates move apart. However, the velocity is found to be directly proportional to the nanoparticle concentration during the squeezing flow i.e. when the plates are coming together and an inverse variation between the velocity and nanoparticle concentration is recorded when the plates are moving apart. It is hope that this study will enhance the understanding the phenomena of squeezing flow in various applications.

1. Introduction

The flow characteristics of fluid between two parallel plates have attracted many research interests. This is due to their several applications in engineering such as foodstuff processing, reactor fluidization, moving pistons, chocolate fillers, hydraulic lifts, electric motors, flow inside syringes and nasogastric tubes, compression, and injection, power transmission squeezed film, polymers processing etc. In such fluid flow applications and processes, the analysis of momentum equation is very essential. Following the pioneer work and the basic formulations of squeezing flows under lubrication assumptions by Stefan [1], there have been increasing research interests and many scientific studies on these types of flow. In a past work over some few decades, Reynolds [2] analyzed the squeezing flow between elliptic plates while Archibald [3] investigated the same problem

*Corresponding author: mikegbeminiyi@gmail.com
DOI: http://dx.doi.org/10.17515/resm2017.46ds0315

for rectangular plates. The earlier studies on squeezing flows were based on Reynolds equation which its insufficiencies for some cases have been shown by Jackson [4] and Usha and Sridharan [5]. Moreover, the nonlinear behaviours of the flow phenomena have attracted several attempts and renewed research interests aiming at properly analyzing and understanding the squeezing flows [5-14].

Casson fluid is a non-Newtonian fluid first invented by Casson in 1959 [15, 16]. It is a shear thinning liquid which is assumed to have an infinite viscosity at zero rate of shear, a yield stress below which no flow occurs, and a zero viscosity at an infinite rate of shear [17]. It is based on the structure of liquid phase and interactive behaviour of solid of a two-phase suspension. It has ability to capture complex rheological properties of a fluid, unlike other simplified models such as the power law [18] and second, third or fourth-grade models [19]. The non-linear Casson's constitutive equation has been found to describe accurately the flow curves of suspensions of pigments in lithographic varnishes used for preparation of printing inks. In particular, the Casson fluid model describes the flow characteristics of blood more accurately at low shear rates and when it flows through small blood vessels [20]. So, human blood can also be treated as a Casson fluid in the presence of several substances such as fibrinogen, globulin in aqueous base plasma, protein, and human red blood cells. Some famous examples of the Casson fluid include jelly, tomato sauce, honey, soup, concentrated fruit juices etc. Concentrated fluids like sauces, honey, juices, blood, and printing inks can be well described using the Casson model. Many researchers [21-30] studied the Casson fluid under different boundary conditions. Some find the solutions by using either approximate methods or numerical schemes and some find its exact analytical solutions. The solutions when the Casson fluids are in free convection flow with constant wall temperature are also determined. On the other hand, the flow behaviours of the Casson fluid in the presence of magnetic field and heat transfer is also an important research area. Therefore, Khalid et al. [31] focused on the unsteady flow of a Casson fluid past an oscillating vertical plate with constant wall temperature under the non-slip conditions. Application of Casson fluid for flow between two rotating cylinders is performed in [32]. The effect of magnetohydrodynamic (MHD) Casson fluid flow in a lateral direction past linear stretching sheet was explained by Nadeem et al. [33].

In the past and recent studies, different numerical and analytical approximate methods have been adopted to analyze the nonlinearity in the flow process [1-64]. It could be stated that the past efforts in analyzing the squeezing flow problems using approximate analytical methods have been largely based on the applications homotopy analysis method (HAM), Adomain decomposition method (ADM), differential transformation method (DTM), variational iteration method (VIM), variation of parameter method (VPM), optimal homotopy asymptotic method (OHAM) etc. However, the determination of the included unknowns (that will satisfy the second boundary conditions) accompanying the approximate analytical solutions of these methods in analyzing the nonlinear problems increases the computational cost and time. Further, numerical schemes are used for the determination of the unknown included parameters. Practically, this attests that the methods (HAM, ADM, VIM, VPM, DTM, OHAM, DJM, and TAM) can be classified as semi-analytical methods rather than pure approximate analytical methods such as regular, singular and homotopy perturbation methods. Also, these methods (HAM, ADM, VIM, VPM, DTM, OHAM, DJM and TAM) traded off relative simplicity and low computational cost for high accuracy as compared to the perturbation methods. Indisputably, the relatively simple, low cost, highly accurate and total analytic method is still required in analyzing the process and nonlinear equations.

The relative simplicity and low computational cost have made perturbation methods to be widely applied in nonlinear analysis of science, non-science and engineering problems. Although, the validities of the solutions of the traditional perturbation methods are limited to small perturbation parameters and weak nonlinearities, there have been various attempts in recent times to overcome these deficiencies [65-72]. Therefore, over the years, the relative simplicity and high accuracy especially in the limit of small parameter have made perturbation methods interesting tools among the most frequently used approximate analytical methods. Although, perturbation methods provide in general, better results for small perturbation parameters, besides having handy mathematical formulations, they have been shown to have good accuracies, even for relatively large values of the perturbation parameter [65-72]. In the class of the perturbation methods, the method of matched asymptotic expansion (MMAE) is mostly used to determine a uniform and accurate approximation to the solution of singularly perturbed differential equations and to find global properties of differential equations. Moreover, to the best of the author's knowledge, such perturbation method has not been used for the analysis of flow under consideration. Therefore, in this paper, method of matched asymptotic expansion is used to analyze the magnetohydrodynamic squeezing flow of Casson nanofluid between two parallel plates. The developed analytical solutions are used to study the effects of various parameters on the squeezing flow between two parallel plates.

2. Model Development and Analytical Solutions

Consider a Casson nanofluid flowing between two parallel plates placed at time-variant distance and under the influence of magnetic field as shown in the Fig. 1. It is assumed that the flow of the nanofluid is laminar, stable, incompressible, isothermal, non-reacting chemically, the nano-particles and base fluid are in thermal equilibrium and the physical properties are constant. The fluid conducts electrical energy as it flows unsteadily under magnetic force field. The fluid structure is everywhere in thermodynamic equilibrium and the plate is maintained at constant temperature.

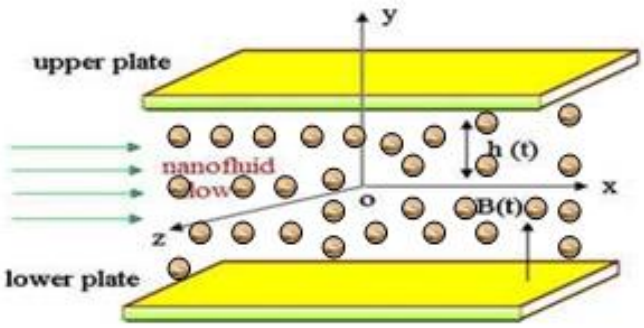

Fig. 1. Model diagram of MHD squeezing flow of nanofluid between two parallel plates embedded in a porous medium

Consider a Casson nanofluid flowing between two parallel plates placed at time-variant distance and under the influence of magnetic field as shown in the Fig. 1. It is assumed that the flow of the nanofluid is laminar, stable, incompressible, isothermal, non-reacting chemically, the nano-particles and base fluid are in thermal equilibrium and the physical properties are constant. The fluid conducts electrical energy as it flows unsteadily under magnetic force field. The fluid structure is everywhere in thermodynamic equilibrium and the plate is maintained at constant temperature.

Using the rheological equation for an isotropic and incompressible Casson fluid, reported by Casson [15,16], is

$$\tau = \tau_0 + \mu\dot{\sigma} \tag{1a}$$

or

$$\tau = \begin{cases} 2\left(\mu_B + \dfrac{p_y}{\sqrt{2\pi}}\right)e_{ij}, & \pi > \pi_c \end{cases} = \begin{cases} 2\left(\mu_B + \dfrac{p_y}{\sqrt{2\pi_c}}\right)e_{ij}, & \pi_c < \pi \end{cases} \tag{1b}$$

where τ is the shear stress, τ_o is the Casson yield stress, μ is the dynamic viscosity, $\dot{\sigma}$ is the shear rate, $\pi = e_{ij}e_{ij}$ and e_{ij} is the $(i,j)th$ component of the deformation rate, π is the product of the component of deformation rate with itself, π_c is a critical value of this product based on the non-Newtonian model, μ_B the is plastic dynamic viscosity of the non-Newtonian fluid and p_y is the yield stress of the fluid. The velocity as well as the temperature is functions of y, t only. Following the assumptions, the governing equations for the flow are given as

$$\frac{\partial u}{\partial x} + \frac{\partial v}{\partial y} = 0 \tag{2}$$

$$\rho_{nf}\left(\frac{\partial u}{\partial t} + u\frac{\partial u}{\partial x} + v\frac{\partial u}{\partial y}\right) = -\frac{\partial p}{\partial x} + \mu_{nf}\left(1+\frac{1}{\beta}\right)\left(2\frac{\partial^2 u}{\partial x^2} + \frac{\partial^2 u}{\partial x\partial y} + \frac{\partial^2 u}{\partial y^2}\right) - \sigma B_o^2 u - \frac{\mu_{nf} u}{K_p} \tag{3}$$

$$\rho_{nf}\left(\frac{\partial v}{\partial t} + u\frac{\partial v}{\partial x} + v\frac{\partial v}{\partial y}\right) = -\frac{\partial p}{\partial y} + \mu_{nf}\left(1+\frac{1}{\beta}\right)\left(2\frac{\partial v}{\partial x^2} + \frac{\partial^2 v}{\partial x\partial y} + \frac{\partial^2 v}{\partial y^2}\right) - \frac{\mu_{nf} v}{K_p} \tag{4}$$

where

$$\rho_{nf} = \rho_f(1-\phi) + \rho_s\phi \tag{5a}$$

$$\mu_{nf} = \frac{\mu_f}{(1-\phi)^{2.5}} \quad \text{(Brinkman model)} \tag{5b}$$

and the magnetic field parameter is given as

$$B(t) = \frac{B_0}{\sqrt{1-\alpha t}} \tag{6}$$

Under the assumption of no-slip condition, the appropriate boundary conditions are given as

$$y = h(t) = H\sqrt{1-\alpha t}, \quad u = 0, \quad v = -V_w$$
$$y = 0, \quad \frac{\partial u}{\partial y} = 0, \quad v = 0 \tag{7}$$
$$x = 0, \quad u = 0$$

On introducing the following dimensionless and similarity variables

$$u = \frac{\alpha x}{2\sqrt{1-\alpha t}} f'(\eta,t), \quad v = -\frac{\alpha x}{2\sqrt{1-\alpha t}} f(\eta,t), \quad \eta = \frac{y}{H\sqrt{1-\alpha t}}$$
$$Re = -SA(1-\phi)^{2.5} = \frac{\rho_{nf} H V_w}{\mu_{nf}}, \quad S = \frac{\alpha H^2}{2\nu_f}, \quad Da = \frac{K_p}{H^2}, \quad A = (1-\phi) + \phi\frac{\rho_s}{\rho_f} \tag{8}$$

One arrives at

$$\left(1+\frac{1}{\beta}\right) f_{\eta\eta\eta\eta} + Re\left(\eta f_{\eta\eta\eta} + 3f_{\eta\eta} + ff_{\eta\eta\eta} - f_\eta f_{\eta\eta}\right) - M^2 f_{\eta\eta} - \frac{1}{Da} f_{\eta\eta} = 0 \tag{9a}$$

Alternatively, Eq. (9a) can be written as it can be

$$\left(1+\frac{1}{\beta}\right) f_{\eta\eta\eta\eta} - SA(1-\phi)^{2.5}\left(\eta f_{\eta\eta\eta} + 3f_{\eta\eta} + ff_{\eta\eta\eta} - f_\eta f_{\eta\eta}\right) - M^2 f_{\eta\eta} - \frac{1}{Da} f_{\eta\eta} = 0 \tag{9b}$$

with the boundary conditions

$$\eta = 0, \quad f = 0, \quad f_{\eta\eta} = 0$$
$$\eta = 1, \quad f = 1, \quad f_\eta = 0 \tag{10}$$

The physical properties of the copper nanoparticles, pure water and kerosene as the base fluids are shown in Table 1.

Table 1: Physical properties of copper nanoparticles, water and kerosene

	Density (kg/m3)	Dynamic viscosity(kg/ms)
Pure water	997.1	0.000891
Kerosene	783.0	0.001640
Copper	8933.0	-

3. Method of Matched Asymptotic Expansion

For small injection and suction at the walls where the permeation Reynolds number is small, the above Eq. (9) can easily be solved using regular perturbation method. It can easily be shown using the regular perturbation method (RPM) that the series solution of Eq. (9), in the absence of magnetic field under a non-porous medium is given as

$$f(\eta)=\frac{\eta}{2}\left(3-\eta^2\right)+\frac{1}{\left(1+\frac{1}{\beta}\right)}Re\left\{\begin{array}{l}\frac{3}{560}\eta^7-\frac{1}{80}\eta^5+\frac{5}{560}\eta^3+\frac{63}{3920}\eta\\+\frac{1}{\left(1+\frac{1}{\beta}\right)}Re\left(\begin{array}{l}\frac{1}{184800}\eta^{11}-\frac{1}{2016}\eta^9+\frac{3}{4900}\eta^7\\+\frac{3}{1400}\eta^5-\frac{3233}{776160}\eta^3+\frac{2459}{1293600}\eta\end{array}\right)\end{array}\right\} \tag{11a}$$

We can also expressed the solution in Eq. (10a) as

$$f(\eta)=\frac{\eta}{2}\left(3-\eta^2\right)-\frac{1}{\left(1+\frac{1}{\beta}\right)}SA(1-\phi)^{2.5}\left\{\begin{array}{l}\frac{3}{560}\eta^7-\frac{1}{80}\eta^5+\frac{5}{560}\eta^3+\frac{63}{3920}\eta\\-\frac{1}{\left(1+\frac{1}{\beta}\right)}SA(1-\phi)^{2.5}\left(\begin{array}{l}\frac{1}{184800}\eta^{11}-\frac{1}{2016}\eta^9+\frac{3}{4900}\eta^7\\+\frac{3}{1400}\eta^5-\frac{3233}{776160}\eta^3+\frac{2459}{1293600}\eta\end{array}\right)\end{array}\right\} \tag{11b}$$

However, for large values of permeation Reynolds number, the solution of the regular perturbation method breaks down. This is because the problem becomes a singular perturbation problem. In order to obtain an analytical solution that is uniformly valid for the whole length of flow, a singular perturbation method, method of matched asymptotic expansion is applied in this work.

Integrating Eq. (9), one arrives at

$$\left(1+\frac{1}{\beta}\right)f_{\eta\eta\eta}+Re\left[\eta f_{\eta\eta}+2f_\eta+ff_{\eta\eta}-\left(f_\eta\right)^2\right]-M^2f_\eta-\frac{1}{Da}f_\eta=\gamma_o \tag{12}$$

where γ_o is space-invariant parameter.

For the purpose of establishing the outer and inner expansions of Eq. (12) subject to the boundary conditions of Eq. (10), Eq. (12) is divided by "*Re*" to have

$$\frac{1}{Re}\left(1+\frac{1}{\beta}\right)f_{\eta\eta\eta}+\eta f_{\eta\eta}+2f_\eta+ff_{\eta\eta}-\left(f_\eta\right)^2-\frac{1}{Re}\left(M^2+\frac{1}{Da}\right)f_\eta=\frac{\gamma_o}{Re} \tag{13}$$

where for large value of $\frac{Re}{\left(1+\frac{1}{\beta}\right)}$, $\frac{1}{Re}\left(1+\frac{1}{\beta}\right)\square\ 1$

Taking $\varepsilon=\frac{1}{Re}\left(1+\frac{1}{\beta}\right)$, Eq. (13) can be written as

$$\varepsilon f_{\eta\eta\eta}+\eta f_{\eta\eta}+2f_\eta+ff_{\eta\eta}-\left(f_\eta\right)^2-\frac{1}{Re}\left(M^2+\frac{1}{Da}\right)f_\eta=\varepsilon\gamma_o \tag{14}$$

For ease of present analysis, Eq. (14) can be re-written as

$$\varepsilon f_{\eta\eta\eta} + \eta f_{\eta\eta} + 2 f_{\eta} + f f_{\eta\eta} - \left(f_{\eta} \right)^2 - \varepsilon^{-\frac{1}{2}} \left[\left(M^2 + \frac{1}{Da} \right) \varepsilon^{\frac{3}{2}} \right] f_{\eta} = -\left[\lambda^2 + \lambda \left[\left(M^2 + \frac{1}{Da} \right) \varepsilon^{\frac{3}{2}} \right] \varepsilon^{-\frac{1}{2}} - 2\lambda \right] \tag{15}$$

Where

$$\varepsilon\gamma_0 = \lambda^2 + \lambda \left[\left(M^2 + \frac{1}{Da} \right) \varepsilon^{\frac{3}{2}} \right] \varepsilon^{-\frac{1}{2}} - 2\lambda$$

Since ε is taken as the small perturbation parameter, it turns out that $\varepsilon^{-\frac{1}{2}} \left[\left(M^2 + \frac{1}{Da} \right) \varepsilon^{\frac{3}{2}} \right] \square\ 1$. Therefore, it is established that the term containing a multiple of $\varepsilon^{-\frac{1}{2}} \left[\left(M^2 + \frac{1}{Da} \right) \varepsilon^{\frac{3}{2}} \right]$ will not disappear in the limiting case as $\varepsilon \to 0.$

Since the small perturbation parameter multiplies the highest derivatives as shown in Eq.(15), then the above problem in Eq. (15) is a singular perturbation problem. Method of matched asymptotic expansion is adopted in the present study to provide an approximate analytical solution to the singular perturbation method. The procedures are given as follows.

3.1 The Outer Solution

Assuming that the outer solution takes the form of a series

$$f = f_0 + f_1 \varepsilon^{\frac{1}{2}} + f_2 \varepsilon + f_3 \varepsilon^{\frac{3}{2}} + \ldots \tag{16}$$

and

$$\lambda = \lambda_0 + \lambda_1 \varepsilon^{\frac{1}{2}} + \lambda_2 \varepsilon + \lambda_3 \varepsilon^{\frac{3}{2}} + \ldots \tag{17}$$

where the coefficients λ_i will be determined by matching the outer solutions with the inner solutions.

Substituting Eq. (16) into Eq. (15), after equating the same power of the coefficient ε, one arrives at:

$$\varepsilon^0 : \qquad \left(f_0^{'} \right)^2 - f_0 f_0^{''} = \lambda_0^2 \tag{18a}$$

$$\varepsilon^{\frac{1}{2}} : \qquad 2 f_0^{'} f_1^{'} - f_0 f_1^{''} - f_0 f_1^{''} = 2\lambda_0 \lambda_1 \tag{18b}$$

$$\varepsilon^{1}: \quad 2f_0^{'}f_2^{'}-f_2^{''}f_0-f_2f_0^{''}=-f_0^{'''}-\eta f_{\eta\eta}+2f_{\eta}-\left(f^{'}\right)^2+f_1f_1^{''} +\left(M^2+\frac{1}{Da}\right)f_0^{'}+2\lambda_0\lambda_2+\lambda_1^2+2Re\lambda_1 \tag{18c}$$

$$\varepsilon^{\frac{3}{2}}: \quad 2f_0^{'}f_3^{'}-f_0^{''}f_3-f_0f_3^{''}=-f_1^{'''}-\eta f_{\eta\eta}+2f_{\eta}-Re\left(\eta f_1^{''}+f_1^{'}\right)-f_3^{*}f_0-f_0^{''}f_3-f_1f_2^{*} -f_2f_1^{''}+2f_1f_2^{'}+2f_0^{'}f_3^{'}+\left(M^2+\frac{1}{Da}\right)f_1^{'}+2Re\lambda_1+2\lambda_1\lambda_2 \tag{18d}$$

With the boundary conditions

$$f_0(0)=f_1(0)=f_2(0)=f_3(0)=0$$
$$f_0^{''}(0)=f_1^{''}(0)=f_2^{''}(0)=f_3^{''}(0)=0 \tag{19}$$

It can easily be shown that the solutions of Eqs. (18a-d) using the above boundary conditions in Eq. (18) are

$$f_0(\eta)=\lambda_0\eta, \quad f_1(\eta)=\lambda_1\eta, \quad f_2(\eta)=\lambda_2\eta, \quad f_3(\eta)=\lambda_3\eta \tag{20}$$

Substituting Eq. (19) into Eq. (15) shows that the outer solution of Eq. (15) is given as

$$f=\left(\lambda_0+\lambda_1\varepsilon^{\frac{1}{2}}+\lambda_2\varepsilon+\lambda_3\varepsilon^{\frac{3}{2}}+\ldots\right)\eta \tag{21}$$

The above outer solution given in Eq. (21) is only valid in the region between the edge of the boundary layer and the center distance between the plates

3.2 The Inner Solution

The inner solution can be developed by applying a stretching transformation $\tau=(1-\eta)\varepsilon^{-\frac{1}{2}}$, which implies that

$$\eta=1-\tau\varepsilon^{\frac{1}{2}} \tag{22}$$

Substituting Eq. (22) into Eq. (15), gives

$$\varepsilon^{\frac{3}{2}}Re\left(2\dot{z}+\tau\ddot{z}\right)-\ddot{z}\left(1+\varepsilon Re\right)+\varepsilon^{\frac{1}{2}}\left(\dddot{z}+\left(\dot{z}\right)^2-z\ddot{z}\right)-\sigma\dot{z}=\lambda^2\varepsilon^{\frac{1}{2}}+\lambda\sigma-2Re\lambda\varepsilon^{\frac{3}{2}} \tag{23}$$

Consequently, the inner boundary conditions are given as

$$z(0)=0, \quad \dot{z}(0)=0 \tag{24}$$

where $\sigma=\left(M^2+\frac{1}{Da}\right)\varepsilon^{\frac{3}{2}}$ and the "dot" shows that the derivative is with respect to τ.

One can assume an inner solution of the form that satisfies the boundary conditions,

$$f(\tau)=1+\sum_{n=0}^{\infty}\varepsilon^{\frac{n+1}{2}}z_n(\tau) \tag{25}$$

$$\varepsilon^{\frac{1}{2}}: \qquad \ddot{z}_0+\dot{z}_0=-\frac{\lambda_0}{\sigma} \tag{26a}$$

$$\varepsilon^{1}: \qquad \ddot{z}_1+\dot{z}_1=-\frac{\lambda_1}{\sigma}+\left(\lambda_0-\left(\frac{\lambda_0}{\sigma}\right)^2\right)e^{-\sigma\tau}-\sigma\left(\frac{\lambda_0}{\sigma}\right)^2\tau e^{-\sigma\tau} \tag{26b}$$

$$\varepsilon^{\frac{3}{2}}: \qquad \ddot{z}_2+\dot{z}_2=-\frac{\lambda_2}{\sigma}+\frac{\alpha\lambda_0}{\sigma}e^{-\sigma\tau}+\left(\frac{\lambda_0}{\sigma}\right)^3e^{-2\sigma\tau}+\left[\begin{array}{l}\lambda_1+\lambda_0\sigma(\sigma\tau-2)-\frac{\lambda_0^2}{2\sigma}\left(3\sigma^2\tau^2-2\sigma\tau-2\right)\\ -\frac{2\lambda_0\lambda_1}{\sigma^2}(\sigma\tau+1)+\frac{1}{2}\left(\frac{\lambda_0}{\sigma}\right)^3\left(\sigma^3\tau^3+\sigma^2\tau^2+2\sigma\tau-2\right)\end{array}\right]e^{-\sigma\tau} \tag{26c}$$

The boundary conditions for these inner solutions are given as:

$$z_0(0)=z_1(0)=z_2(0)=\ldots=z_n(0)=0, \qquad \dot{z}_0(0)=\dot{z}_1(0)=\dot{z}_2(0)=\ldots=\dot{z}_n(0)=0 \tag{27}$$

The solutions of Eq. (26a), (26b) and (26c) using the boundary conditions in Eq. (27) are given as

$$z_0=\frac{\lambda_0}{\sigma}\left(1-\sigma\tau-e^{-\sigma\tau}\right) \tag{28a}$$

$$z_1=\frac{\lambda_0}{\sigma}(1-\sigma\tau)+\lambda_0-2\left(\frac{\lambda_0}{\sigma}\right)^2-\left\{\frac{\lambda_1}{\sigma}+\lambda_0(1+\sigma\tau)-\frac{1}{2}\left(\frac{\lambda_0}{\sigma}\right)^2(2+\sigma\tau)^2\right\}e^{-\sigma\tau} \tag{28b}$$

$$\begin{aligned}z_2=&\frac{\lambda_2}{\sigma}(1-\sigma\tau)+\frac{9}{2}\left(\frac{\lambda_0}{\sigma}\right)^3+\lambda_1-\lambda_0\sigma-\frac{\lambda_0^2}{\sigma}-\frac{4\lambda_0\lambda_1}{\sigma^2}+\frac{\lambda_0 Re}{\sigma}-\frac{\lambda_0 Re}{\sigma}(1+\sigma\tau)e^{-\sigma\tau}\\&-\left\{\frac{\lambda_2}{\sigma}+\lambda_1(1+\sigma\tau)+\frac{1}{2}\lambda_0\sigma\left[(\sigma\tau)^2-2\sigma\tau-2\right]\right\}e^{-\sigma\tau}-\frac{\lambda_0^2}{2\sigma}\left[(\sigma\tau)^3+2(\sigma\tau)^2+2\sigma\tau+2\right]\\&-\frac{\lambda_0\lambda_1}{\sigma^2}\left[(\sigma\tau)^2+4\sigma\tau+4\right]+\frac{1}{24}\left(\frac{\lambda_0}{\sigma}\right)^3\left[3(\sigma\tau)^4+16(\sigma\tau)^3+60(\sigma\tau)^2+96\sigma\tau+120\right]e^{-\sigma\tau}\\&+\frac{1}{24}\left(\frac{\lambda_0}{\sigma}\right)^3e^{-2\sigma\tau}\end{aligned} \tag{28c}$$

On substituting Eqs. (28a-28c) into Eq. (25), gives the second-order inner solution which is valid in the boundary layer region as

$$f(\tau)=1+\varepsilon^{\frac{1}{2}}\left\{\begin{array}{l}\left[\frac{\lambda_0}{\sigma}\left(1-\sigma\tau-e^{-\sigma\tau}\right)\right]+\left\{\begin{array}{l}\frac{\lambda_0}{\sigma}(1-\sigma\tau)+\lambda_0-2\left(\frac{\lambda_0}{\sigma}\right)^2\\-\left\{\frac{\lambda_1}{\sigma}+\lambda_0(1+\sigma\tau)-\frac{1}{2}\left(\frac{\lambda_0}{\sigma}\right)^2(2+\sigma\tau)^2\right\}e^{-\sigma\tau}\end{array}\right\}\varepsilon^{\frac{1}{2}}\\+\left\{\begin{array}{l}\frac{\lambda_2}{\sigma}(1-\sigma\tau)+\frac{9}{2}\left(\frac{\lambda_0}{\sigma}\right)^3+\lambda_1-\lambda_0\sigma-\frac{\lambda_0^2}{\sigma}-\frac{4\lambda_0\lambda_1}{\sigma^2}+\frac{\lambda_0 Re}{\sigma}-\frac{\lambda_0 Re}{\sigma}(1+\sigma\tau)e^{-\sigma\tau}\\-\left\{\frac{\lambda_2}{\sigma}+\lambda_1(1+\sigma\tau)+\frac{1}{2}\lambda_0\sigma\left[(\sigma\tau)^2-2\sigma\tau-2\right]\right\}e^{-\sigma\tau}-\frac{\lambda_0^2}{2\sigma}\left[(\sigma\tau)^3+2(\sigma\tau)^2+2\sigma\tau+2\right]\\-\frac{\lambda_0\lambda_1}{\sigma^2}\left[(\sigma\tau)^2+4\sigma\tau+4\right]+\frac{1}{24}\left(\frac{\lambda_0}{\sigma}\right)^3\left[3(\sigma\tau)^4+16(\sigma\tau)^3+60(\sigma\tau)^2+96\sigma\tau+120\right]e^{-\sigma\tau}\\+\frac{1}{24}\left(\frac{\lambda_0}{\sigma}\right)^3e^{-2\sigma\tau}\end{array}\right\}\varepsilon\end{array}\right\} \tag{29}$$

Alternatively, Eq. (29) can be expressed as

$$f(\tau)=1+\varepsilon^{\frac{1}{2}}\left\{\begin{array}{l}\left[\frac{\lambda_0}{\sigma}\left(1-\sigma\tau-e^{-\sigma\tau}\right)\right]+\left\{\begin{array}{l}\frac{\lambda_0}{\sigma}(1-\sigma\tau)+\lambda_0-2\left(\frac{\lambda_0}{\sigma}\right)^2\\-\left\{\frac{\lambda_1}{\sigma}+\lambda_0(1+\sigma\tau)-\frac{1}{2}\left(\frac{\lambda_0}{\sigma}\right)^2(2+\sigma\tau)^2\right\}e^{-\sigma\tau}\end{array}\right\}\varepsilon^{\frac{1}{2}}\\+\left\{\begin{array}{l}\frac{\lambda_2}{\sigma}(1-\sigma\tau)+\frac{9}{2}\left(\frac{\lambda_0}{\sigma}\right)^3+\lambda_1-\lambda_0\sigma-\frac{\lambda_0^2}{\sigma}-\frac{4\lambda_0\lambda_1}{\sigma^2}-\frac{\lambda_0 SA(1-\phi)^{2.5}}{\sigma}+\frac{\lambda_0 SA(1-\phi)^{2.5}}{\sigma}(1+\sigma\tau)e^{-\sigma\tau}\\-\left\{\frac{\lambda_2}{\sigma}+\lambda_1(1+\sigma\tau)+\frac{1}{2}\lambda_0\sigma\left[(\sigma\tau)^2-2\sigma\tau-2\right]\right\}e^{-\sigma\tau}-\frac{\lambda_0^2}{2\sigma}\left[(\sigma\tau)^3+2(\sigma\tau)^2+2\sigma\tau+2\right]\\-\frac{\lambda_0\lambda_1}{\sigma^2}\left[(\sigma\tau)^2+4\sigma\tau+4\right]+\frac{1}{24}\left(\frac{\lambda_0}{\sigma}\right)^3\left[3(\sigma\tau)^4+16(\sigma\tau)^3+60(\sigma\tau)^2+96\sigma\tau+120\right]e^{-\sigma\tau}\\+\frac{1}{24}\left(\frac{\lambda_0}{\sigma}\right)^3e^{-2\sigma\tau}\end{array}\right\}\varepsilon\end{array}\right\} \tag{30}$$

3.2 Matching criteria

The final complete solution can be established by matching the outer solutions with the inner solutions at the edge of the boundary layer i.e. by imposing continuity between the solutions at different scales. This is done to determine the constants or the coefficients λ_i in the outer solution. Expressing the outer solution in terms of the inner variable τ and matching it with the inner solution as $\tau\to\infty$ gives

$$\lambda_0=1,\quad \lambda_1=\frac{1}{\sigma},\quad \lambda_2=1-\frac{1}{\sigma^2} \tag{31}$$

Therefore, the outer solution can be written as

$$f(\eta)=\left\{\lambda_0+\frac{1}{\sigma}\varepsilon^{\frac{1}{2}}+\left(1-\frac{1}{\sigma^2}\right)\varepsilon+\ldots\right\}\eta \tag{32}$$

The complete solution is given by Eqs. (30) and (32). It should be noted the inner solution given by Eq. (30) is valid even outside the boundary layer region i.e. it is uniformly valid throughout the region of $0<\eta<1$.

Another physical quantity of interest in this analysis is the skin friction coefficient, which can be expressed as

$$C_f = \frac{\mu_{nf}\left(1+\frac{1}{\beta}\right)\left(\frac{\partial u}{\partial y}\right)_{y=h(t)}}{\rho_{nf}V_w^2} \tag{33}$$

Using the dimensionless variables in Eq. (8), the dimensionless form of Eq. (33) is given as

$$C_f^* = \frac{H^2}{x^2\left(1-\alpha t\right)Re_x C_f} = \left(1+\frac{1}{\beta}\right)A\left(1-\phi\right)^{2.5}\ f''(1) \tag{34}$$

It should be noted that developed ordinary non-linear differential equation in Eq. (9b) together with the boundary conditions in Eq. (10) was also solved using shooting method coupled with Runge-Kutta-Fehlberg method. The Runge–Kutta–Fehlberg method is an embedded method from the Runge-Kutta family. In the method, the identical function evaluations are used in conjunction with each other to create methods of varying order and similar error constants. By performing one extra calculation, the error in the solution can be estimated and controlled by using the higher-order embedded method that allows for an adaptive step-size to be determined automatically. The Runge-Kutta-Fehlberg is currently the default method in GNU Octave's ode45 solver.

4. Results and Discussion

For the purpose of demonstrating the accuracy of MMAE and RPM, Tables 1-3 show the comparisons of results of the perturbation methods with the results of the numerical methods for different values of permeation Reynolds and Hartmann numbers. In the perturbation methods, it could be established that there is no additional computational cost in the determination of the coefficients or constants of the outer solution. This shows that the cost of computation of approximate analytical solution using the perturbation methods is lower than using the other approximate analytical methods. Although, the solutions of perturbation methods depend on small parameters, its high accuracy within the vicinity of the small perturbation parameters is well established.

Table 2: Comparison of results of flow for large squeezing number in the absence of magnetic field

f	Squeezing	S= 101	M=0, 1/Da=0
η	NM	MMAE	Residue
0.0	0.00000	0.00000	0.00000
0.1	0.16377	0.16414	0.00037
0.2	0.32193	0.32254	0.00061
0.3	0.46995	0.47078	0.00083
0.4	0.60424	0.60523	0.00099
0.5	0.72190	0.72292	0.00102
0.6	0.82063	0.82154	0.00091
0.7	0.89871	0.89938	0.00067
0.8	0.95498	0.95535	0.00037
0.9	0.98878	0.98890	0.00012
1.0	1.00000	1.00000	0.00000

Table 3: Comparison of results for small squeezing number in the absence of magnetic field

f	Squeezing S = 0.5, M=0, 1/Da=0			Squeezing S = 1.5, M=0, 1/Da=0		
η	NM	MMAE	Residue	NM	MMAE	Residue
0.0	0.00000	0.00000	0.00000	0.00000	0.00000	0.00000
0.2	0.31707	0.29170	0.02537	0.31609	0.29880	0.01720
0.4	0.59972	0.57140	0.02832	0.59818	0.57410	0.02408
0.6	0.81886	0.79940	0.01946	0.81747	0.80190	0.01557
0.8	0.95526	0.95690	0.01640	0.95430	0.95800	0.00370
1.0	1.00000	1.00000	0.00000	1.00000	1.00000	0.00000

The results for small and large values of squeezing number are shown in Tables. It could be depicted from the Tables that for small value of squeezing number, the difference between the results of the numerical method (NM) and that of regular perturbation method (RPM) decreases as the squeezing number decreases. Additionally, it is found that the approximate analytical solutions using RPM are practically equivalent to the exact solution for sufficiently small $|S|$. However, regular perturbation solution becomes less reliable and breaks down when the perturbation parameter, S becomes large i.e. the asymptotic error increases as value of the squeezing number increases. This therefore shows that the accuracy of the RPM is commensurate with the smallness of squeezing number. From the analysis, it is established that the solution of the RPM is a fair approximation to the solution of the NM for $-5 \leq S \leq 5$. It should be pointed out that the asymptotic solutions deteriorate when the preceding term is of the same order as proceeding term. i.e. the perturbation solution breaks downs when second term in the asymptotic solution is of the same magnitude with the first term or when the third term in the solution is quantitatively the same as the second term. Although, the method of matched asymptotic expansion gives accurate results for the large values of the permeation squeezing number, it was found that its analytical solution breaks down when

the perturbation parameter, S, is no longer large. Consequently, the error between the NM and MMAE becomes increasing large when S is not large enough for the singular perturbation solutions.

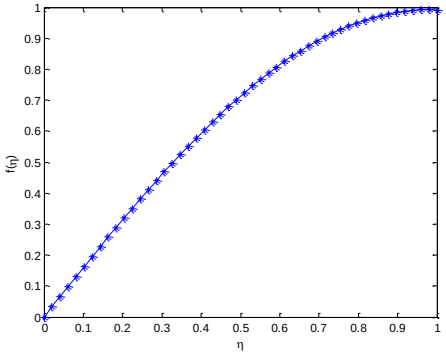

Figure 2a Variation of f(η) with the flow length

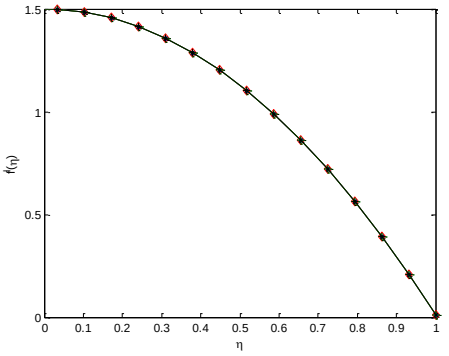

Figure 2b Variation of f'(η) with the flow length

For the value of nanoparticle parameter value, ϕ = 0.15, Figs. 2 and 3 depict the pattern of the flow behavior of the fluid. The figures show that the decrease in the axial velocity of the fluid near the wall region causes an increase in velocity gradient at the wall region. Also, because of the conservativeness of the mass flow rate, the decrease in the fluid velocity near the wall region is compensated by the increasing fluid velocity near the central region.

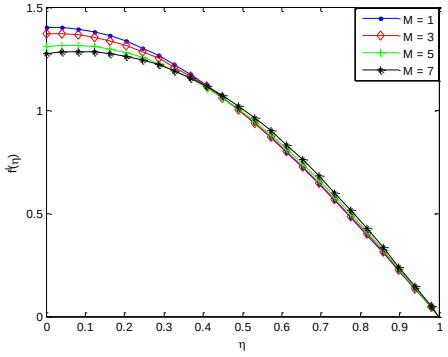

Figure 3 Effects of magnetic number on the velocity of the fluid

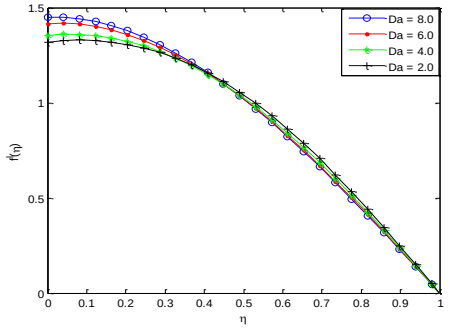

Figure 4 Effects of Darcy number on the velocity

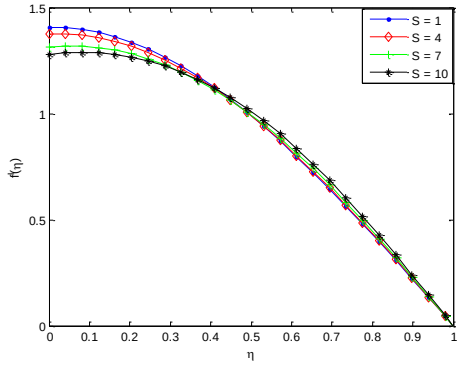

Figure 5 Effects of Squeezing number on the velocity

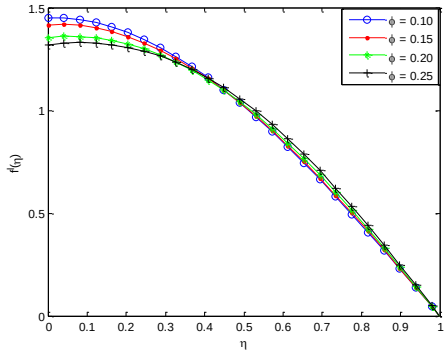

Figure 6 Effects of nanoparticle fraction on the velocity

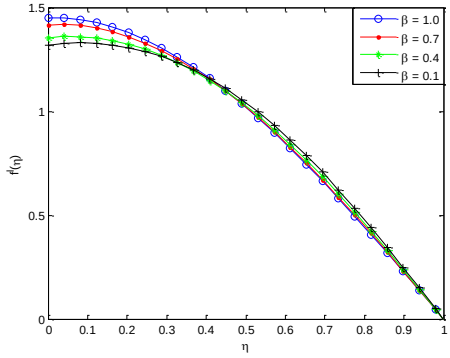

Figure 7 Effects of Casson fluid parameter on the velocity

Fig. 3 which shows the effect of increasing magnetic number or Hartmann parameter (M) on the flow characteristics of the fluid. It is observed that at increasing values of M, the velocity decreases in the range of $0 \leq \eta \leq 0.5$ and then increases in the range $0.5 < \eta \leq 1$. The flow response to the presence of magnetic field is due to the Lorentz force created by the magnetic field which retards the fluid motion at boundary layer during the squeezing flow i.e. when the plates are coming together. It should be noted that during the squeezing flow, especially when the plates are very close to each other, then the flow together with retarding Lorentz force creates adverse pressure gradient. Whenever such forces act over a long time then there might be a point of separation and back flow occurs. The flow velocity of the nanofluids further decreases as the magnetic field parameter increases when the plates move apart. The flow behaviour when the plates move apart are depicted in the figure. This behaviour is as a result of a vacant space occurs and in order not to violate the law of conservation of mass, the fluid in that region moves with high velocity and consequently, an accelerated flow is observed.

Effects of Darcy number on the flow pattern of the Casson nanofluid between the two parallel plates is portrayed in Fig. 4. The figure displays an opposite trend to that of the squeezing number effects on the flow. It could be seen from the figure that as the Darcy number increases, the velocity increases in the range of $0 \leq \eta \leq 0.5$ and then decreases in the range $0.5 < \eta \leq 1$.

Fig. 5 displays the effects of squeezing number on the flow behavior of the fluid. It is clear from the figure that as the squeezing number increases, the velocity decreases in the range of $0 \leq \eta \leq 0.5$ and then increases in the range $0.5 < \eta \leq 1$. Effect of nanoparticle fraction on the fluid velocity is depicted in Fig. 6. The result shows that as the solid volume fraction of the fluid increases the velocity decreases in the range of $0 \leq \eta \leq 0.5$ and then increases in the range $0.5 < \eta \leq 1$. This is because as the nanoparticle volume increases, more collision occurs between nanoparticle and particles with the boundary surface of the plates and consequently the resulting flow retardation which decreases the fluid velocity near the boundary layer. The flow behaviour of the Casson nanofluid to increasing Casson fluid parameter is shown in Fig. 7. The figure depicts the effects of Casson fluid parameter on velocity profile of Casson nanofluid. It is obvious from the figure that Casson the parameter has influence on axial velocity. From the figure, it is clear that the magnitude of velocity of the fluid decreases in the range of $0 \leq \eta \leq 0.5$ and then increases in the range $0.5 < \eta \leq 1$ as the Casson fluid parameter increases.

5. Conclusion

In this work, magnetohydrodynamic squeezing flow of Casson nanofluid between two plates has been analyzed using method of matched asymptotic expansion. The obtained analytical solutions were used to investigate the squeezing phenomena of the nanofluid between the moving plates. Also, the effects of the pertinent flow parameters on the flow process were investigated and discussed. The results of the analytical solutions as developed in this study are good agreement with the results of the numerical method using fourth-fifth order Runge-Kutta-Fehlberg method. The results in this work can be used to further the study of squeezing flow in applications such as power transmission, polymer processing and hydraulic lifts.

Nomenclature

B(t)	Magnetic field strength
Ha	Hartmann parameter
P	Pressure
p_y	Yield stress of the fluid
S	Squeeze Parameter
u	Velocity in x direction
v	Velocity in y Direction
w	Dimensionless velocity in y direction
x	Horizontal axis of flow
y	Perpendicular axis to the flow
k_{nf}	Effective thermal conductivity

Greek Symbol

μ_{nf}	Effective dynamic viscosity
ρ_{nf}	Effective density
η	Dimensionless similarity variable
τ	Hear stress
τ_o	Casson yield stress
μ	Dynamic viscosity
$\dot{\sigma}$	Shear rate
e_{ij}	$(i,j)th$ component of the deformation rate,
π	Product of the component of deformation rate with itself,
π_c	critical value of this product based on the non-Newtonian model,
μ_B	plastic dynamic viscosity of the non-Newtonian fluid

References

[1] M. J. Stefan. Versuch Uber die scheinbare adhesion'', Sitzungsberichte der Akademie der Wissenschaften in Wien. Mathematik-Naturwissen 69, 713–721, 1874.

[2] O. Reynolds. On the theory of lubrication and its application to Mr Beauchamp Tower's experiments, including an experimental determination of the viscosity of olive oil. Philos. Trans. Royal Soc. London 177, 157–234, 1886. https://doi.org/10.1098/rstl.1886.0005

[3] F. R. Archibald, F.R., 1956. Load capacity and time relations for squeeze films. J. Lubr. Technol. 78, A231–A245.

[4] J. D. Jackson. A study of squeezing flow. Appl. Sci. Res. A 11, 148–152, 1962. https://doi.org/10.1007/BF03184719

[5] R. Usha and R. Sridharan, R. Arbitrary squeezing of a viscous fluid between elliptic plates. Fluid Dyn. Res. 18, 35–51, 1996. https://doi.org/10.1016/0169-5983(96)00002-0

[6] Wolfe, W.A., 1965. Squeeze film pressures. Appl. Sci. Res. 14, 77–90. Yang, K.T., 1958. Unsteady laminar boundary layers in an incom- pressible stagnation flow. J. Appl. Math. Trans. ASME 80, 421– 427.

[7] D. C. Kuzma. Fluid inertia effects in squeeze films. Appl. Sci. Res. 18, 15–20, 1968. https://doi.org/10.1007/BF00382330

[8] J. A. Tichy, W. O. Winer. Inertial considerations in parallel circular squeeze film bearings. J. Lubr. Technol. 92, 588–592, 1970. https://doi.org/10.1115/1.3451480

[9] R. J. Grimm. Squeezing flows of Newtonian liquid films: an analysis include the fluid inertia. Appl. Sci. Res. 32 (2), 149–166, 1976. https://doi.org/10.1007/BF00383711

[10] G. Birkhoff. Hydrodynamics, a Study in Logic, Fact and Similitude, Revised ed. Princeton University Press, 137, 1960.

[11] C. Y. Wang. The squeezing of fluid between two plates. J. Appl. Mech. 43 (4), 579–583, 1976. https://doi.org/10.1115/1.3423935

[12] C. Y. Wang, L. T. Watson. Squeezing of a viscous fluid between elliptic plates. Appl. Sci. Res. 35, 195–207, 1979. https://doi.org/10.1007/BF00382705

[13] M. H. Hamdan and R. M. Baron. Analysis of the squeezing flow of dusty fluids. Appl. Sci. Res. 49, 345–354, 1992. https://doi.org/10.1007/BF00419980

[14] P. T. Nhan. Squeeze flow of a viscoelastic solid. J. Non-Newtonian Fluid Mech. 95, 343–362, 2000. https://doi.org/10.1016/S0377-0257(00)00175-0

[15] N. Casson, Rheology of Dispersed System,vol.84,Pergamon Press, Oxford, UK, 1959.

[16]. Casson, N: A flow equation for the pigment oil suspension of the printing ink type. In: Rheology of Disperse Systems, pp. 84-102. Pergamon, New York (1959)

[17] R. K. Dash, K. N. Mehta, and G. Jayaraman, "Casson fluid flow in a pipe filled with a homogeneous porous medium," International Journal of Engineering Science,34(10), 1145–1156, 1996. https://doi.org/10.1016/0020-7225(96)00012-2

[18] H.I.Andersson and B.S.Dandapat,Flow of a power-law fluid over a stretching sheet. Applied Analysis of Continuous Media, 1(339), 1992.

[19] I. M.Sajid, T. A. Hayat and M.Ayub, Unsteadyflow and heat transfer of a second grade fluid over a stretching sheet," Communications in Nonlinear Science and Numerical Simulation,14(1), 96–108, 2009. https://doi.org/10.1016/j.cnsns.2007.07.014

[20] D. A. McDonald. Blood Flows in Arteries, 2nd edn., Chapter 2. Arnold, London (1974)

[21] U. Khan, N. Ahmed, S. I. U. Khan, B. Saima, S. T. Mohyud-din. Unsteady Squeezing flow of Casson fluid between parallel plates. World J. Model. Simul. 10 (4), 308–319, 2014.

[22] M. Mustafa, M, Hayat, T, Pop, I, Aziz, A: Unsteady boundary layer flow of a Casson fluid due to impulsively started moving flat plate. Heat Transf. Asian Res. 40(6), 563-576 (2011) https://doi.org/10.1002/htj.20358

[23]. T. Hayat, S. A. Shehzad, A. Alsaedi, M. S. Alhothuali. Mixed convection stagnation point flow of Casson fluid with convective boundary conditions. Chin. Phys. Lett. 29(11), Article ID 114704 (2012) https://doi.org/10.1088/0256-307X/29/11/114704

[24] S. Mukhopadhyay. Effects of thermal radiation on Casson fluid flow and heat transfer over an unsteady stretching surface subject to suction/blowing. Chin. Phys. B 22(11), Article ID 114702 (2013) https://doi.org/10.1088/1674-1056/22/11/114702

[25] Mukhopadhyay, S, De, PR, Bhattacharyya, K, Layek, GC: Casson fluid flow over an unsteady stretching surface. Ain Shams Eng. J. 4, 933-938 (2013) https://doi.org/10.1016/j.asej.2013.04.004

[26] M. F. Shateyi and W. A. Khanm. Effects of thermal radiation on Casson flow heat and mass transfer around a circular cylinder in porous medium. Eur. Phys. J. Plus 130, 188 (2015) https://doi.org/10.1140/epjp/i2015-15188-y

[27] K. Bhattacharyya. Boundary layer stagnation-point flow of Casson fluid and heat transfer towards a shrinking/stretching sheet. Front. Heat Mass Transf. 4, Article ID 023003 (2013)

[28] S. Pramanik. Casson fluid flow and heat transfer past an exponentially porous stretching surface in presence of thermal radiation. Ain Shams Eng. J. 5, 205-212 (2014) https://doi.org/10.1016/j.asej.2013.05.003

[29] S. Shateyi. A new numerical approach to MHD flow of a Maxwell fluid past a vertical stretching sheet in the presence of thermophoresis and chemical reaction. Bound. Value Probl. 2013, Article ID 196 (2013) https://doi.org/10.1186/1687-2770-2013-196

[30] G. Makanda, S. Shaw, P. Sibanda. Effects of radiation on MHD free convection of a Casson fluid from a horizontal circular cylinder with partial slip in non-Darcy porous medium with viscous dissipation. Bound. Value Probl. 2015, Article ID 75 (2015) https://doi.org/10.1186/s13661-015-0333-5

[31] Khalid, A, Khan, I, Shafie, S: Exact solutions for unsteady free convection flow of Casson fluid over an oscillating vertical plate with constant wall temperature. Abstr. Appl. Anal. 2014, Article ID 946350 (2014)

[32] N. T. M. Eldabe and M. G. E. Salwa, "Heat transfer of mhd non-Newtonian Casson fluid flow between two rotating cylinder," Journal of the Physical Society of Japan,vol.64,p.4164,1995.

[33] S. Nadeem, R. L. Haq, N. S. Akbar, and Z. H. Khan, "MHD three-dimensional Casson fluid flow past a porous linearly stretching sheet", Alexandria. Engineering Journal, Vol. 52, pp. 577582, (2013).

[34] M.M. Rashidi, H. Shahmohamadi and S. Dinarvand, "Analytic approximate solutions for unsteady two dimensional and axisymmetric squeezing flows between parallel plates," Mathematical Problems in Engineering, Vol. (2008), pp. 1-13, 2008.

[35]H.M. Duwairi, B. Tashtoush and R.A. Domesh, "On heat transfer effects of a viscous fluid squeezed and extruded between parallel plates,"Heat Mass Transfer, vol. (14), pp.112-117, 2004.

[36]A. Qayyum, M. Awais, A. Alsaedi and T.Hayat, "Squeezing flow of non-Newtonian second grade fluids and micro polar models, "Chinese Physics Letters, vol. (29), 034701, 2012

[37]M.H Hamdam and R.M. Baron, "Analysis of squeezing flow of dusty fluids," Applied Science Research, 49, 345-354, 1992. https://doi.org/10.1007/BF00419980

[38]M.Mahmood,S.Assghar and M.A. Hossain, "Squeezed flow and heat transfer over a porous surface for viscous fluid," Heat and mass Transfer, 44, 165-173. https://doi.org/10.1007/s00231-006-0218-3

[39]M. Hatami and D.Jing, "Differential Transformation Method for Newtonian and non-Newtonian nanofluids flow analysis: Compared to numerical solution, "Alexandria Engineering Journal, vol. (55), 731-729.

[40] S. T. Mohyud-Din, Z. A. Zaidi, U. Khan, N. Ahmed. On heat and mass transfer analysis for the flow of a nanofluid between rotating parallel plates, Aerospace Science and Technology, 46, 514-522, 2014. https://doi.org/10.1016/j.ast.2015.07.020

[41] S. T. Mohyud-Din, S. I. Khan. Nonlinear radiation effects on squeezing flow of a Casson fluid between parallel disks, Aerospace Science & Technology, Elsevier 48, 186-192, 2016 https://doi.org/10.1016/j.ast.2015.10.019

[42] M. Qayyum, H. Khan, M. T. Rahim, I. Ullah. Modeling and Analysis of Unsteady Axisymmetric Squeezing Fluid Flow through Porous Medium Channel with Slip Boundary. PLoS ONE 10(3), 2015 https://doi.org/10.1371/journal.pone.0117368

[43] M. Qayyum and H. Khan. Behavioral Study of Unsteady Squeezing Flow through Porous Medium, Journal of Porous Media, pp: 83-94, 2016. https://doi.org/10.1615/JPorMedia.v19.i1.60

[44]M. Mustafa, Hayat and S. Obaidat "On heat and mass transfer in the unsteady squeezing flow between parallel plates," Mechanica, vol. (47), pp.1581-1589, 2012.

[45] A.M. Siddiqui, S. Irum, and A.R. Ansari, "Unsteady squeezing flow of viscous MHD fluid between parallel plates," Mathematical Modeling Analysis, vol. (2008), 565-576, 2008.

[46]G. Domairry and A. Aziz, "Approximate analysis of MHD squeeze flow between two parallel disk with suction or injection by homotopy perturbation method," Mathematical Problem in Engineering, 603-616,2009.

[47]N. Acharya, K. Das and P.K. Kundu, "The squeezing flow of Cu-water and Cu-kerosene nanofluid between two parallel plates," Alexandria Engineering Journal, vol. (55), 1177-1186.

[48] N. Ahmed, U. Khan, X. J. Yang, S. I. U. Khan, Z.A. Zaidi, S. T. Mohyud-Din. Magneto hydrodynamic (MHD) squeezing flow of a Casson fluid between parallel disks. Int. J. Phys. Sci. 8 (36), 1788–1799, 2013.

[49] N. Ahmed, U. Khan, Z. A. Zaidi, S. U. Jan, A. Waheed, S. T. Mohyud-Din. MHD Flow of a Dusty Incompressible Fluid between Dilating and Squeezing Porous Walls, Journal of Porous Media, Begal House, 17 (10), 861-867, 2014.

[50] U. Khan, N. Ahmed, S. I. U. Khan, Z. A. Zaidi, X. J. Yang, S. T. Mohyud-Din. On unsteady two-dimensional and axisymmetric squeezing flow between parallel plates. Alexandria Eng. J. 53, 463–468, 2014a. https://doi.org/10.1016/j.aej.2014.02.002

[51] U. Khan, N. Ahmed, Z. A. Zaidi, M. Asadullah, S. T. Mohyud-Din. MHD squeezing flow between two infinite plates. Ain Shams Eng. J. 5, 187–192, 2014b. https://doi.org/10.1016/j.asej.2013.09.007

[52]T. Hayat, A. Yousaf, M. Mustafa and S.Obadiat, "MHD squeezing flow of second grade fluid between parallel disks," International Journal of Numerical Methods, vol. (69), pp.399-410, 2011.

[53] H. Khan, M. Qayyum, O. Khan, and M. Ali. Unsteady Squeezing Flow of Casson Fluid with Magnetohydrodynamic Effect and Passing through Porous Medium," Mathematical Problems in Engineering, vol. 2016, Article ID 4293721, 14 pages, 2016.

[54] I. Ullah, M.T. Rahim, H. Khan, M. Qayyum. Analytical Analysis of Squeezing Flow in Porous Medium with MHD Effect, U.P.B. Sci. Bull., Series A, 78, Iss. 2, 2016.

[55] M. Qayyum, H. Khan, M. T. Rahim, and I. Ullah. Analysis of Unsteady Axisymmetric Squeezing Fluid Flow with Slip and No-Slip Boundaries Using OHAM, Mathematical Problems in Engineering, vol. 2015 (2015). https://doi.org/10.1155/2015/860857

[56] M. Qayyum, H. Khan and O. Khan. Slip Analysis at Fluid-Solid Interface in MHD Squeezing Flow of Casson Fluid through Porous Medium, Results in Physics, 7(2017), 732-750. https://doi.org/10.1016/j.rinp.2017.01.033

[57] O. Khan, M. Qayyum, H. Khan and A. Ali. Improved Analysis for Squeezing of Newtonian Material Between Two Circular Plates, Advances in Materials Science and Engineering, vol. 2017 (2017). https://doi.org/10.1155/2017/5703291

[58] M. Qayyum, H. Khan and M. T. Rahim. A Novel Approach to Approximate Unsteady Squeezing Flow through Porous Medium, Journal of Prime Research in Mathematics, Vol.12 (1) (2016), 91-109.

[59] M.G. Sobamowo and A. T. Akinshilo . On the analysis of squeezing flow of nanofluid between two parallel plates under the influence of magnetic field. Article in Press in Alexandra Engineering Journal. Publication of Elsevier.

[60] M. G. Sobamowo (2017). On the analysis of laminar flow of viscous fluid through a porous channel with suction/injection at slowly expanding or contracting walls. Journal of Computational Applied Mechanics. Vol. 48(2), Article in Press. Journal of Faculty of Engineering, University of Tehran, Iran.

[61] M. G. Sobamowo and L. O. Jayesimi . Squeezing flow analysis of nanofluid under the effects of magnetic field and slip boundary using Chebychev spectral collocation method. Fluid Mechanics, Vol. 3(6)(2017). Article in Press, Science Publishing Group.

[62] M. G. Sobamowo, O. A. Adeleye and J. D. Femi-Oyetoro. Unsteady two-dimensional flow analysis of nanofluid through a porous channel with expanding or contracting walls using Adomian decomposition method. Journal of Engineering Research. Accepted Article. Publication of Faculty of Engineering, University of Lagos, Nigeria, 2017.

[63] A. T. Akinshilo and M. G. Sobamowo. Perturbation Solutions for the Study of MHD Blood as a Third Grade Nanofluid Transporting Gold Nanoparticles through a Porous Channel. Journal of Applied and Computational Mechanics. Vol. 3(2) (2017), 103-113. Publication of Shahid Chamran University of Ahvaz, Iran.

[64] M. G. Sobamowo, L.O. Jayesimi and M. A. Waheed (2017). Magnetohydrodynamic squeezing flow analysis of nanofluid under the effect of slip boundary conditions using variation of parameter. Karbala International Journal of Modern Science. 4(1) (2018), 107-118.

[65] B. Y. Ogunmola, A. T. Akinshilo and M. G. Sobamowo. Perturbation solutions for Hagen-Poiselle flow and Heat transfer of Third-grade fluid with temperature-dependent viscosities and internal heat generation. International Journal of Engineering Mathematics, 2016, Article ID 8915745, 12 pages.

[66] M. G. Sobamowo. Singular perturbation and differential transform methods to two-dimensional flow of nanofluid in a porous channel with expanding/contracting walls subjected to a uniform tranverse magnetic field. Thermal Science and Engineering Progress. 4(2017), 71-84. https://doi.org/10.1016/j.tsep.2017.09.001

[67] U. H. Filobello-Ni-o, Vazquez-Leal, Y. Khan, A. Yildirim, V.M. Jimenez-Fernandez, A. L Herrera May, R. Casta-eda-Sheissa, and J.Cervantes Perez. Perturbation Method and Laplace-Padé

Approximation to solve nonlinear problems. Miskolc Mathematical Notes, 14(1) (2013) 89-101.

[68] U. H. Filobello-Ni-o, Vazquez-Leal, K. Boubaker, Y. Khan, A. Perez-Sesma, A.Sarmiento Reyes, V.M. Jimenez-Fernandez, A Diaz-Sanchez, A. Herrera-May, J. Sanchez-Orea and K. Pereyra-Castro, Perturbation Method as a Powerful Tool to Solve Highly Nonlinear Problems: The Case of Gelfand,s Equation. Asian Journal of Mathematics and Statistics, (2013) 7 pages, DOI: 10.3923 /ajms.2013.

[69] R. Lewandowski. Analysis of strongly non-linear free vibration of beams using perturbation method. Civil and Environmental Reports

[70] Y. K. Cheung, S. H. Chen, S. L. Lau. A modified Lindsteadt-Poincare method for certain strongly non-linear oscillators, International Journal of Non-Linear Mechanics, 26 (1991) 367-378. https://doi.org/10.1016/0020-7462(91)90066-3

[71] C. W. Lim., B. S. Wu. A modified Mickens procedure for certain non-linear oscillators, Journal of Sound and Vibration, 257 (2002) 202-206. https://doi.org/10.1006/jsvi.2001.4233

[72] H. Hu A classical perturbation technique which is valid for large parameters, Journal of Sound and Vibration, 269 (2004) 409-412. https://doi.org/10.1016/S0022-460X(03)00318-3

Research on Engineering Structures & Materials
journal homepage: http://jresm.org
Research Group

Research Article

The design of multi-sample flexural fatigue device and fatigue behavior of glass/epoxy laminated composites

H Ersen Balcıoğlu*,[1], Raif Sakin[2], Halit GÜN[1]

[1] *Department of Mechanical Engineering, Faculty of Engineering, Uşak University, Turkey*
[2] *Department of Machine and Metal Technologies, Edremit Vocational School of Higher Education, Balıkesir University, Turkey*

Article Info

Article history:
Received 17 Sep 2018
Revised 01 Nov 2018
Accepted 02 Nov 2018

Keywords:

Glass/epoxy;
S-N curves;
Fixed-end type flexural fatigue;
Multi sample test machine;
Displacement controlled fatigue

Abstract

Due to fiber reinforced polymer composite materials have a brittle structure, it is important to know their behavior under dynamic loads. Therefore, it is necessary to know the S-N curve that characterizes the fatigue life of the composite material, when selecting and sizing the material. In this study, fatigue behavior of glass/epoxy laminated composites was investigated under flexural loading. For this aim, computer controlled fixed end type flexural fatigue test machine was developed and glass/epoxy test samples were tested under flexural stress corresponding to 80%, 70%, %60, %50, and %40 of the static 3-point bending strength. In addition, the static strengths of the epoxy-laminated composites under tensile, compressive and flexural loads were also determined. It has been observed that the damage such as matrix and fiber cracks and delamination in the glass/epoxy laminated composites, which were exposed to flexural deformation. Also, it has been seen that, the developed fixed end type flexural fatigue test machine can be used to determine fatigue behavior of thin-walled composite materials.

1. Introduction

Composite materials are formed by combining two different components called fibers and matrices at the macro level. The occurred new material has superior mechanical and physical properties than both fiber and matrix material. Composite materials have come to the forefront by result of studies, which were did in order to meet the economical, high strength and very light material needs that required by the development of technology. So that, they have become an alternative to traditional building materials and their usage has become increasingly widespread, due to their superior mechanical and physical properties.

Many building elements are subjected to repetitive loads or repetitive elastic deformations during their usage. As a result of repetitive loads, the materials lose their rigidity over time and damage at the stress values under yield strength. This phenomenon is called fatigue. Fatigue behavior of composite materials detection is more difficult unlike isotropic materials. The reason for this, the number of parameters handled during the design of composite materials is high. Composite materials tend to accumulate damages in structures and damage does not always occur in a macroscopic dimension. Some damage mechanism such as fiber damage, separation, reverse layer cracks and matrix cracks can occur in laminated composites, during fatigue. Several studies have been carried out to

*Corresponding author: ersen.balcioglu@usak.edu.tr
DOI: http://dx.doi.org/10.17515/resm2018.67me0917

understand this complex damage mechanism under fatigue loading of layered composite materials.

Shenoi et al. [1] have presented an investigation on the fatigue behavior of sandwich beams with fiber reinforced polymer (FRP) skins and PVC foam core. Their study revealed core shear as dominant failure mode via gradual loss in foam core stiffness and concluded that beam fatigue life of sandwich is dictated by the core fatigue life. Nikforooz et al. [2] have investigated the fatigue performance of laminated glass fiber polyamide having eight layers under tension-tension loading. The test results showed that the fiber orientation and layer thickness were effective on fatigue behavior of glass/polyamide and glass/epoxy composites. Bureau and Denault [3] produced woven glass/polypropylene laminates using different process parameters. Flexural fatigue tests showed a general decrease of the life to final failure and increase in the stiffness drop in the presence of porosity. Dickson et al. [4] studied the fatigue behavior of cross ply 0/90 and ±45 carbon/PEEK and carbon/epoxy. They found that 0/90 lay-up for both materials had comparable fatigue resistance while ±45 carbon/PEEK laminates had better fatigue resistance than carbon/epoxy laminates. The other result obtained from fatigue test that the fatigue response of a cross-plied carbon/PEEK laminate in the $\pm 45^{o}$ orientation is much better than that of equivalent carbon/epoxy composites, again because the superior properties of the thermoplastic matrix.

Belingardi et al. [5] conducted a detailed material characterization and study of bending fatigue property of relatively complex un-notched intra-ply hybrid composite that consists of distinct layers of biaxial glass-fiber-reinforced composite and biaxial carbon fiber-reinforced composites as well as biaxial layers of bundles of carbon and glass fibers mixed within a single layer. Beyene et al. [6] have investigated the effect of notch on flexural fatigue performance of twill glass/epoxy composite. Displacement-controlled flexural fatigue tests have been conducted on the specimens and damage in the composite has been continuously monitored during cycling. Test results showed that it is observed that different notched geometry behave differently for quasi-static and fatigue loading. Koricho et al. [7] have investigated the fatigue behavior of glass/epoxy laminated composites by using displacement controlled flexural fatigue test machine. Test results showed that when the fatigue load level increases, the fatigue life decreases is short and the extent of damaged zone prior to catastrophic failure becomes smaller. Also, at low fatigue load level, the fatigue life is long and the extent of damaged zone becomes wider. Sakin et al. [8] investigated flexural fatigue behavior of glass fiber reinforced polyester composite materials, glass-fiber woven and randomly distributed glass-fiber mat samples with polyester resin. According to the test results, the highest fatigue life has been obtained from 800 g/m^2 fiber glass woven specimens with 0/90 lay-up. Liang et al. [9] conduced an experimental investigations of tension–tension fatigue tests on flax/epoxy and glass/epoxy composites specimens with $[0/90]_{3S}$ and $[\pm 45]_{3S}$ stacking sequences. The stiffness degradation of both composites exhibits similar trend despite the loading level. Ellyin and Kujawski [10] investigated the frequency effect on the tensile fatigue performance of angle-ply glass fiber reinforced laminate and concluded that there was a considerable influence of test loading frequency. Especially for matrix dominated laminates and loading condition, frequency becomes important due to the general sensitivity of the matrix to the loading rate and because of the internal heating generation and associated temperature raise.

Fatigue tests are performed in loading conditions such as tensile, compressive, flexural and torsion, which is at the stress values below the static strengths of the material. Fatigue test machine, which can test under different load conditions with load control or displacement control, have been developed for fatigue tests. Kulkarni et al. [11] have developed plane

flexural fatigue testing machine for composite material. Gheilmetti et al. [12] have developed flexural fatigue test machine for high frequency applications of flat aluminum specimens. Mokhtarnia et al. [13] have developed an original flexural fatigue test machine, which have capable of applying stress control load in different loading waveforms, frequencies, and stress ratios, for fatigue characterization of composite materials. Balcioglu et al. [14] have developed a multi-sample fatigue test machine, which characterizes the flexural fatigue behavior of fiber-reinforced composite sheets, wooden sheets, plastic-based sheets and light metal sheets.

In this study, a displacement controlled fatigue device capable of testing 10 samples at the same time was developed to characterize flexural fatigue behavior of composite materials. The flexural fatigue behaviors of glass/epoxy laminated composites were investigated by the developed device. The three-point bending strength and three-point bending modulus were statically calculated to determine the displacement values to be applied to the glass/epoxy samples during the fatigue test. After that, the fatigue test specimens were subjected to fatigue tests at loading values corresponding to 80%, 70%, 60%, 50% and 40% of the static three-point bending strengths in order to obtain the S-N curve characterizing the glass/epoxy composite fatigue behavior. In addition, tensile and compressive behavior of glass/epoxy laminated composites were determined within static tests.

2. Fatigue Test Machine

In fatigue tests, the two most important parameters that determining fatigue life of the material are amplitude and frequency. In addition, the test frequency of the fatigue device and the resonance frequency of the material under the actual loading conditions must be the same. It is not right to choose a material, which work under low frequency, according to the high frequency fatigue test results and It is not right to interpret the fatigue life of that material. Since heterogeneous materials such as composites are anisotropic, it is difficult to characterize fatigue behavior parameters with conventional fatigue devices and methods. The standard test frequency range for polymer matrix composites is frequency as low as 1-10 Hz. The temperature increases during the test due to hysteretic heating at higher frequencies and in this case the isothermal behavior of the composite changes [8,13].

Almost all of the fatigue testing machines are tested at the same time as the single sample. However, in order to obtain the S-N curves characterizing the fatigue strength limit of the material, it is necessary to test at least 5 samples in response to each deformation or stress value. Generally; fatigue tests are performed to accurately form the S-N curve at 7-8 different stress values that below the static strength of the material. In this case, an average of 35-40 samples must be subjected to the fatigue test to obtain the S-N curve for a single material parameter. In a fatigue test performed on a classical fatigue testing machine, it is necessary to use a total of 80 samples if considered 2 different material parameters and 5 repetitions for each stress value. Assuming the fatigue test frequency is 10Hz, the total test duration for our high cycle fatigue test, which we plan to continue to 10 million load cycles, is approximately 146 days. In this study, it was aimed to develop a new multi-samples fatigue testing machine to investigate the fatigue behavior of fiber reinforced composite plates when considering limitations and disadvantages of previous fatigue test machines, such as total test time, mechanical efficiency, low production cost.

There are very few multi-sample fatigue testing machines available for lightweight plate materials [15–17]. In this study, differential from literature, a flexural fatigue test machine

was developed, which has a remotely controllable, user-friendly interface, take instantaneous fatigue data for each sample without loss even at high frequencies. Computer-controlled fixed-end type flexural fatigue testing machine is fully computer controlled thanks to the developed software. Fatigue testing of viscoelastic materials is carried out in two different modes, either as a displacement-controlled or stress-controlled test [13,18]. The main feature of the fatigue testing device in this study is the ability to perform a constant displacement-controlled test (Figure 1).

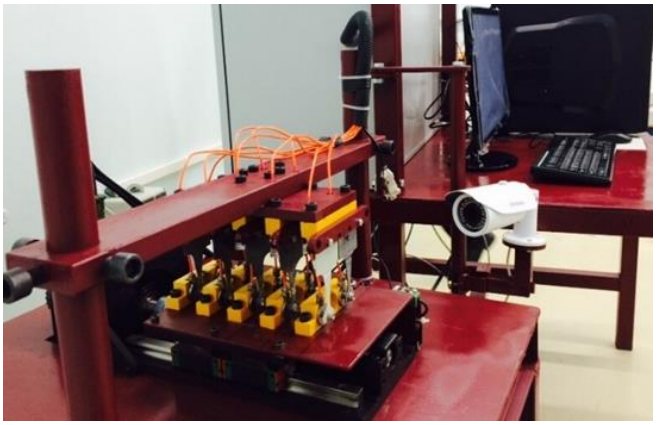

Fig. 1 Displacement controlled multi-sample fixed-end type flexural fatigue tester

In most of the classical flexural fatigue test machines, the displacement value is obtained by the crank-pinch mechanism. The maximum and minimum displacement values are usually adjusted manually by means of mechanical construction. In this case, it is difficult to obtain a precise value. In addition, the effect of centrifugal force come in view due to high frequency in the fatigue tests that performed on these types of test machine. The displacement value is provided with 5μm accuracy by means of the linear screw moving table which is moved forward/backward by helping of servo-motor controlled by software in the developed fatigue test machine. In classical fatigue testing machines, defining and setting the initial zero position is another important challenge. If the initial zero position cannot be precisely determined in the fixed-end type fatigue devices, it will occur pre-tensioning at sample due to the momentum which occurs by axis misalignment. In this case, the true S-N curve that express the fatigue behavior of the material cannot be determined. In the developed fatigue testing machine, the initial zero position was defined once to the device precisely. The device comes to the initial zero position with a single button fall in to the software interface and each test starts from the same zero position. In order to better understand the working principle of the fatigue device, the parts of the machine are numbered and given definitions in Figure 2.

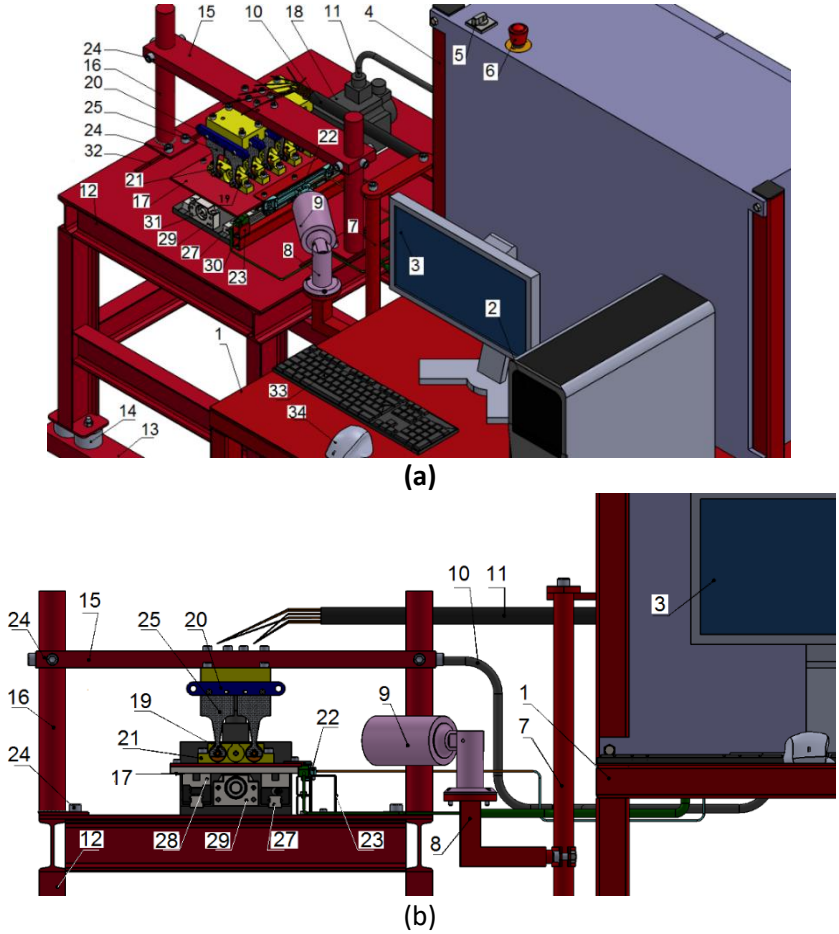

1. Chassis-1
2. PC
3. Software interface
4. Main control panel
5. System start / stop button
6. Emergency stop-switch
7. Rotating camera holder
8. Camera adjustment mechanism
9. IP camera
10. Load cell cabling
11. Power cable
12. Chassis-2
13. Lower fixing U profile
14. Rubber shock absorbers
15. Height adjustment block
16. Holding arms
17. Linear sliding table
18. Servo-motor
19. Load cell
20. Holder -1 (sample fixture)
21. Holder -2 (sample movement area)
22. Magnetic readers and linear encoder
23. Sensor holder
24. Distance adjustment screws
25. Test samples
26. Couplings
27. Linear cradles
28. Linear rails
29. Bearings
30. Limit safety sensors
31. Screw shaft (step = 20mm)
32. Sliding base plate
33. Keyboard
34. Mouse

Fig. 2 The components of multi-sample fixed-end type flexural fatigue test machine [14]

3. Experimental Studies

The tests carried out in the scope of the study were carried out in two stages; as static and dynamic. In the first stage, the tensile strength, tensile modulus, compressive strength, three-point bending strength and bending modulus of the glass/epoxy composite were determined under static loads. Then the fatigue behavior of glass/epoxy composite were determined by using the stress and strain values obtained from the three-point bending test data.

3.1. Static Tests

In the study, glass/epoxy laminated composite materials were produced by hand lay-up methods. The stacking sequence of $[0/90]_4$ laminate consists of 8 layers of biaxial fabrics having 300g/m^2 weight. The matrix material was procured from Duratek Epoxy and Polyurethane System in Turkey. It has two components as DTE 1100 epoxy and DST 1105 hardener. They were prepared by mixing 74/26 in weight, respectively. Glass/epoxy laminated composites, which manufactured by hand lay-up method, were cured at 100^{o}C under pressure of 6MPa for 100min, by using temperature–time–pressure controlled hydraulic press.

The test specimens were sized according to ASTM D 3039M-93 standard to determine the tensile strength of the produced sandwich composites [19]. Longitudinal Young modulus (E_1) and longitudinal tensile strength (X_t) were obtained by using longitudinal direction of glass/epoxy composite specimens (Figure 3(a)). Transverse Young modulus (E_2) and transverse tensile strength (Y_t) were also obtained by using transverse direction of glass/epoxy laminated composite specimens (Figure 3(b)). The tensile strengths in the longitudinal and transverse directions (Xt and Yt) were determined by dividing the failure load by the cross-sectional area of the longitudinal and transverse specimens, respectively.

Shear properties were determined according to the ASTM D3518M-13 standard test method [20]. This test method determines the in-plane shear response of polymer matrix composite materials reinforced by high modulus fibers (Figure 3(c)). The composite material form is limited to a continuous-fiber-reinforced composite ±45° laminate capable of being tension tested in the laminate x direction. The in-plane shear modulus (G_{12}), was defined by using Eq. 1, where E_{45} is elasticity modulus in 45^o fiber direction and ϑ_{12} is major Poisson's ratio [21]. Poisson's ratio ϑ_{12} was accepted as 0.32 according to studies in the literature [22].

Compressive properties were determined according to the ASTM D3410-87 standard test method [20]. Longitudinal and transverse compressive strength of glass/epoxy composite specimens (X_c and Y_c) were calculated by dividing the failure load to the cross-sectional area of the specimens in longitudinal and transverse direction, respectively (Figure 3(d)).

$$G_{12} = \frac{1}{\frac{4}{E_{45}} - \frac{1}{E_1} - \frac{1}{E_2} + \frac{2\vartheta_{12}}{E_1}} \tag{1}$$

The flexural strength and flexural modulus of the glass/epoxy composites were determined according to ASTM D7264 test standard [24] . According to this standard span-to-thickness ratio is 32:1, the standard specimen thickness is 4 mm, and the standard specimen width is 13 mm with the specimen length being about 20% longer than the support span (Figure 3(e)).

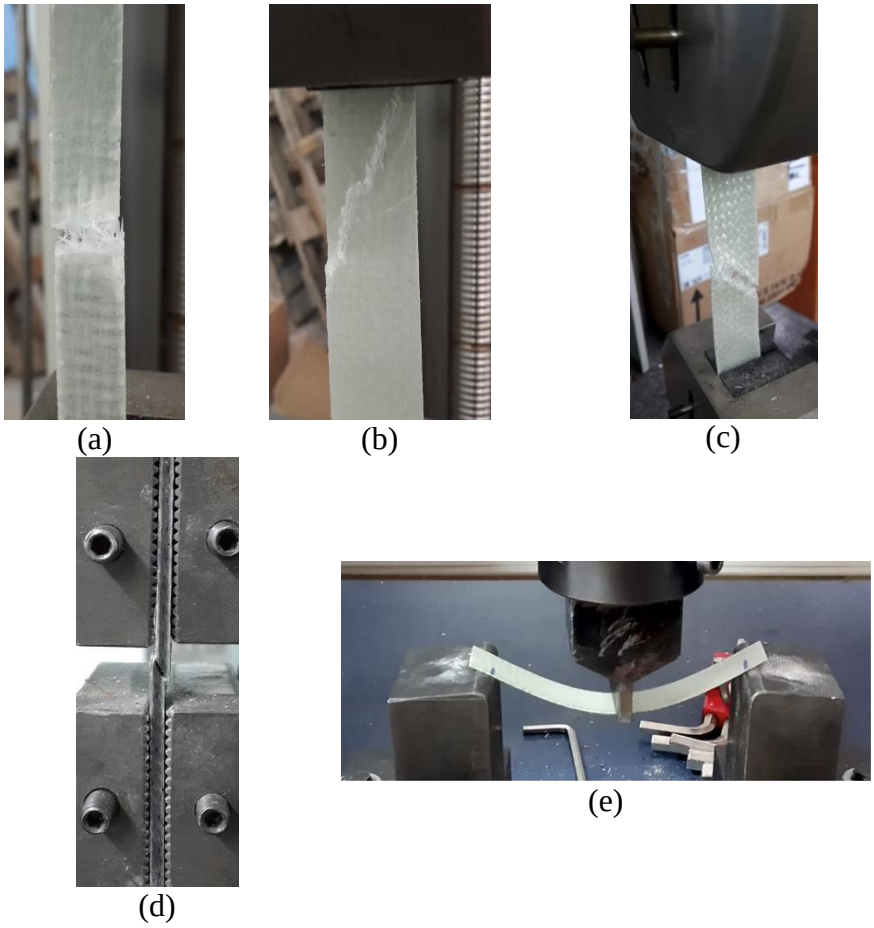

Fig. 3 Static test set up (a-c) tensile test, (d) compression test and (e) flexural tests

The load-displacement graph of each test sample was drawn thanks to the computer-controlled software of the test device. Then, three-point bending strength and flexural modulus was calculated by using data, which was obtained from the graphs, in Equations 2-3.

$$\sigma_f = \frac{3PL}{2bh^2} \tag{2}$$

$$E_f = \frac{L^3 m}{4bh^3} \tag{3}$$

where, P maximum load, L support span, b width of specimen, h thickness of beam, m slope of the load-displacement curve. Three specimens were tested for each material parameters and average of the obtained three test results was accepted as main value.

3.2. Fatigue Tests

Fatigue tests are repeated for lower stress levels starting from stress values at least 20% below the static strength of the material. The device manufactured within the scope of the study is displacement controlled. For this reason, it is necessary to calculate the value of the strain (displacement) which will occur the desired level of stress. In this context, the Hooke law, which expresses the relationship between the stress and stress of the material, has been utilized. The displacement values which will give the desired stress value were calculated by using the equation (4-5) given below [24];

$$\sigma_f = \varepsilon . E_f \tag{4}$$

$$\varepsilon = \frac{6\delta h}{L^2} \tag{5}$$

In these equations, "ε", "E_f", and "δ" denotes the unit flexural deformation, flexural modulus, and the maximum flexural deformation value, respectively. The maximum flexural strength value obtained from each composite sample was used as one cyclic flexural strength in the fatigue test. The displacement value (δ) required for the desired stress value was calculated separately for each test parameter. This value was transferred to the developed multi-sample flexural fatigue device by its servo motor software.

Test sample that were prepared according to the ASTM D671-93 test standard shown in Figure 4 was used for the fatigue tests. This test method covers the determination of the effect of repetitions of the same magnitude of flexural stress on plastics by fixed-end type testing machines, designed to produce a constant-amplitude-of-force on the test specimen each cycle [25]. To prevent hysteretic heating, fatigue tests were carried out at a test frequency of 5Hz and under a R = ±1 strain rate.

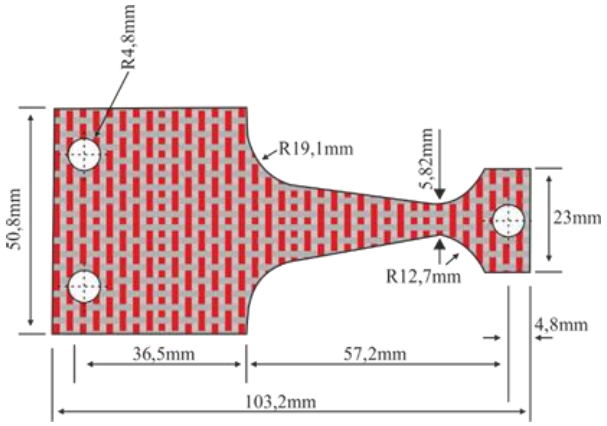

Fig. 4 Fatigue test specimen and dimensions

Fatigue behavior of a material is usually characterized by S-N diagram, showing the relationship between the stress amplitude or maximum stress and number of cycles to failure on a semi logarithmic scale. This diagram is obtained by testing a number of specimens at various stress levels. S-N diagram is of considerable value to the designer especially when the structure contains a critical component where any failure is catastrophic. In order to obtain S-N curves characterizing the fatigue strength-fatigue life behavior of the glass/epoxy composite material, the test specimens were exposed to

fatigue at stress level of 80%, 70%, 60%, 50% and 40%, which correspond to the static three-point flexural strength of the material. Fatigue stress (σ_F), which causes fatigue fracture or fatigue damage during flexural load, was determined according to equation 6 given below;

$$\sigma_F = \frac{6PL}{bh^2} \tag{6}$$

where, P is the force read from the load cell, L is the distance from the load applied site to the fatigue damage region, b is the width of the sample damage region, and h is the sample thickness. In order to draw the S-N curve of the material, the force value on the sample was read and recorded once per 1000 cycles via the load cell. Then, the fatigue strength corresponding to the relevant cycle value is calculated using Equation 6. The stress when the test sample was subjected to fatigue damage was considered as fatigue damage strength (σ_{FD}). Five samples were tested for each stress level and the average of the obtained values was taken as the main fatigue life.

4. Results and Discussions

4.1. Static Test Results

Static tests were achieved at U-Test brand 50kN capacity universal tensile test machine at room temperature. Totally three samples were tested from each type of test. The average of the results obtained from the three samples was accepted as a main mechanical property value. The load-displacement curves of glass/epoxy laminated composites in tensile tests are shown in Figure 5. Accordingly, the glass/epoxy composites showed similar behavior by damage as brittle in the longitudinal fiber direction and transverse fiber direction. Matrix cracking and fiber breaking under tensile loading are successive damage mechanisms (Figure 3(a)). In addition, the fracture progressed angularly rather than linearly, depending on the orientation of the fiber in the sample (Figure 3(b-c)).

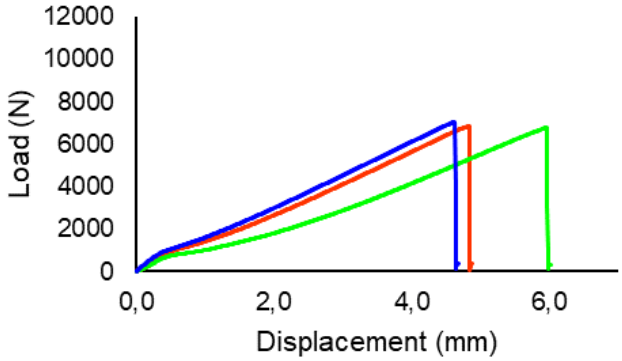

(a)

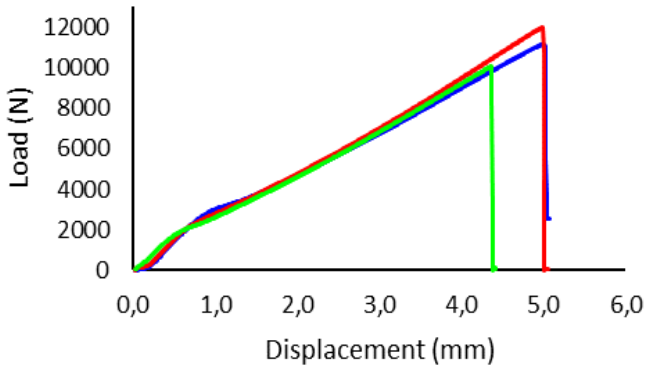

(a)

Fig. 5 Load-displacement curve obtained from tensile test (a) longitudinal fiber direction and (b) transverse fiber direction

Compression tests were carried out longitudinal fiber direction and transverse fiber direction as being in tensile test. The load-displacement curve obtained from the compression tests is given in Figure 6. As a result of the compression loading, fiber breakage and shear failure occurred fractionally. The ultimate damage ensured by breaking of fiber brittle (Figure 3 (d)).

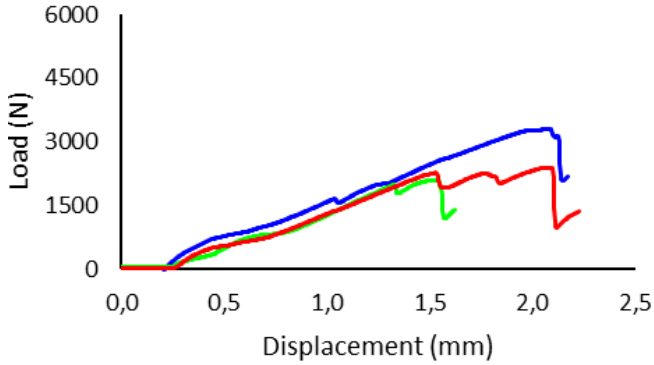

(a)

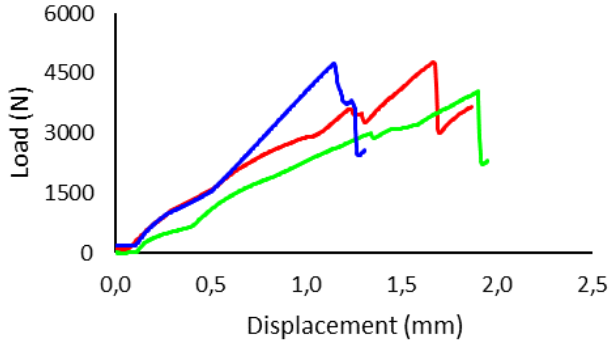

(b)

Fig. 6 Load-displacement curve obtained from compression test (a) longitudinal fiber direction and (b) transverse fiber direction

Flexural strength (σ_f) and flexural modulus (E_f) of glass/epoxy laminated composites were investigated under three-point bending load. The load-displacement curve obtained from the three-point bending test of glass/epoxy laminated composites was given in Figure 7. All results were plotted in terms of applied load versus center displacement of the sample under the crosshead of the electronic universal tester machine.

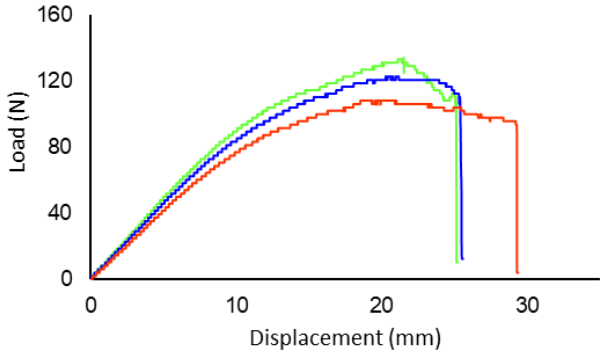

Fig. 7 Load-displacement curve of glass/epoxy laminated composite obtained from three-point bending test

The obtained curves were divided into three stages. The first stage, which is appearance in linear, can explain the elastic deformation of the glass/epoxy composite laminate. There is no linear relationship between displacement and load in the second stage. The load increase was less relative to displacement and the sample reached at maximum flexural load that it can bear in this stage. Also, micro matrix cracks and delaminations occurred in this stage. In spite of the increasing of displacement the increase in the load was inevitably diminished or becomes a flat form in the third region. In the third stage, previous peak load can never reach because the load that ensure in this stage was carried by only the reinforcement element. At the end, the fibers break apart and the sample cracked as brittle. The flexural strength (σ_f) and flexural modulus (E_f) values obtained from the three point bending tests are given in Table 1 together with the standard deviations.

When the values given for the mechanical properties in Table 1 are examined, it is seen that the values were close to each other in longitudinal fiber and transverse fiber direction. However, the values in longitudinal fiber direction were higher for each mechanical property. In this case it can be said that, similar glass filaments were used in each two directions for glass woven fabric and the number of filaments in the longitudinal fiber direction was many.

Table 1. Mechanical properties of glass/epoxy laminated composites with standard deviation under tensile, compression and three-point bending loading

Test Type	Mechanical Properties Value (MPa)	Standard Deviation Value (MPa)
Longitudinal direction elasticity modulus (E1)	32636.45	580.80
Transverse direction elasticity modulus (E2)	30326.93	780.78
Tensile strength in longitudinal direction (Xt)	360.67	12.19
Tensile strength in transverse direction (Yt)	348.07	7.59
In-plane shear modulus (G12)	2849.50	-
Compression strength in longitudinal direction (Xc)	244.56	15.44
Compression strength in transverse direction (Yc)	238.23	20.70
Flexural modulus (Ef)	30952.65	2823.46
Flexural strength (σ_f)	495.45	11.34

4.2. Fatigue Test Results

Glass/epoxy laminated composites with thermoset matrix structure have a brittle structure. However, depending on loading conditions, brittle fracture damage may not always occur under variable loads. During the flexural fatigue tests, two different damage forms were observed in glass/epoxy laminated composites. Fracture damage occurred in test specimens which were forced to fatigue at the level of stress near the static three-point bending strength. The matrix cracks propagated rapidly by the result of high bending stress and the fiber matrix interface connection weakened. Fatigue damage was spread to the fiber matrix interface by the increase in the number of cycles and caused separation of layers (delamination). Finally, the glass/epoxy composite sample was fractured in a brittle manner. (Figure 8a). The number of cycles until fracture failure was considered as the fatigue life (N_f).

Although, the specimens were forced to fatigue at low stresses until number of cycles of 10^6, which was accepted as theoretical fatigue life for this study, but they did not show any breakage in the samples. In the event of such damage, the stiffness of the test sample decreases as the number of cycles increases. This means that less strain is applied for the same displacement. The loss of rigidity that occur by the time in specimens was taken as the criterion of fatigue, because fatigue fracture was not observed in specimens forced to fatigue at low stress levels. According to the ISO 13003 standards, stiffness reduction between 5% and 20% can be accepted as the fatigue failure in FRP composites [26]. So that 20% stiffness loss was considered as the fatigue damage criterion for non-fractured specimens in the fatigue test. The stress value on the specimen was accepted as fatigue damage stress (σ_{FD}) when 20% stiffness loss occurred. For non-fractured samples, the number of cycles passed for a 20% stiffness loss was considered as fatigue life (N_f).

Matrix cracks and fiber-matrix interface damage progress more slowly in variable loads at low stress levels. Tensile and compressive stresses, which were occurred by bending, cause stiffness loss in the sample. However, delamination damage take place with starting from weak edges of the test sample to center of sample. Despite of the losing the strength

of the composite specimen with delamination, low stress does not cause fracture of the fibers, radically (Figure 8b).

Fig. 8 Fatigue damage of glass/epoxy composite (a) crack and (b) delamination

Load value that corresponding to each cycle was recorded, thanks to the software of the developed fatigue device. So that, the fatigue strength corresponding to each cycle was calculated with the help of Equation (6). In figure 9 have presented loss of stiffness that occurred with the increasing of number of cycles in the test specimen. Accordingly, the decrease in stiffness loss is clearly seen by increasing of the stress amplitude. Such that, in 50,000 cycles, the glass / epoxy specimen lost 7%, 18%, 20%, 26% and 29% of the stiffness at 40%, 50%, 60%, 70% and 80% of stress amplitude, respectively.

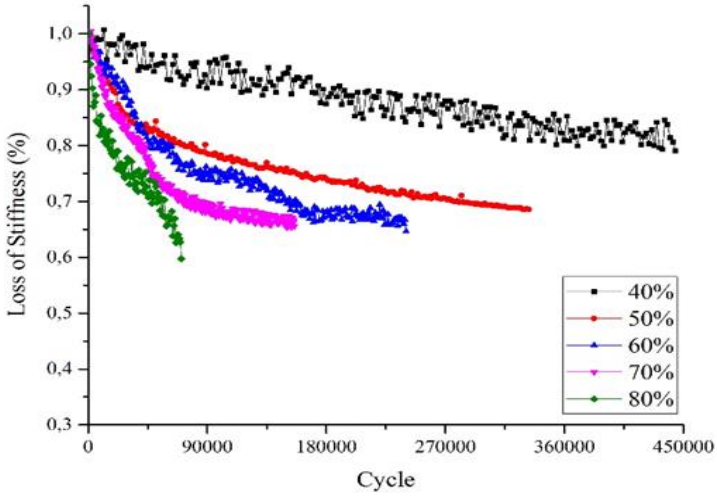

Fig. 9 Stiffness losses of glass/epoxy test samples

Laminated composites are thin-walled structures and thin-walled structural elements are more susceptible to bending and buckling loads. Table 2 shows the flexural strength and fatigue life of layered composites which were loaded static and dynamically at different stress levels with the standard deviations. Hereunder, glass/epoxy composite material has

a maximum fatigue life of 354800 cycles under a full variable loading of 218.64 MPa. According to the static situation, the glass/epoxy composite sample lost 55.96% of its strength at the end of the cycle of 354800. If similar comparison is performed for glass/epoxy test specimen that loaded dynamically at a stress level of 80% of static strength, the test specimen is damaged by breaking when the flexural strength of the specimen lost 18.18%. This means that the damage tolerances of the brittle glass / epoxy composites are very low in the dynamic stresses at high stress amplitudes.

The fatigue strength increased by the stress amplitude increased and nevertheless fatigue life decreased. When stress amplitude reached from 40% to 80%, the fatigue strength increased by 85%, while the fatigue life decreased by 557%.

Table 2. The fatigue life corresponding to the fatigue stress in different stress amplitude

Stress Level (%)	**Stress (σ_{FD}) (MPa)**	***Cycle(N_F)***	**Loss of Rigidity According to Static Loading (%)**
40	218.64 (22.17)	354800 (25440.13)	55.96
50	256.78 (17.71)	271100 (19122.63)	48.28
60	308.36 (26.96)	165240 (5035.18)	37.78
70	367.34 (25.97)	113700 (23145.19)	25.86
80	405.70 (23.17)	54000 (4662.62)	18.18
100 (Static)	495.45 (11.34)	1	-

*(Standard deviation)

The S-N curve representing the relation of fatigue strength-fatigue life under different stress amplitude of glass/epoxy laminated composite was given in Figure 10. For glass/epoxy samples, breakage of samples or loss of 20% rigidity was accepted as fatigue damage in this scope of study. Even if the breaking was not observed on samples, the experiment was not continued after 20% rigidity loss. The theoretical fatigue life for polymer matrix composites is 10^6 cycles [8]. The fatigue strength corresponding to the theoretical life was expressed by the Power Law function. The Power Law function, which expresses mathematically the fatigue mechanism, was indicated on the graph. As shown in Fig. 10, the Power Law equation for glass/epoxy samples is expressed in;

$$\sigma_F = 15791N^{-0.33}$$

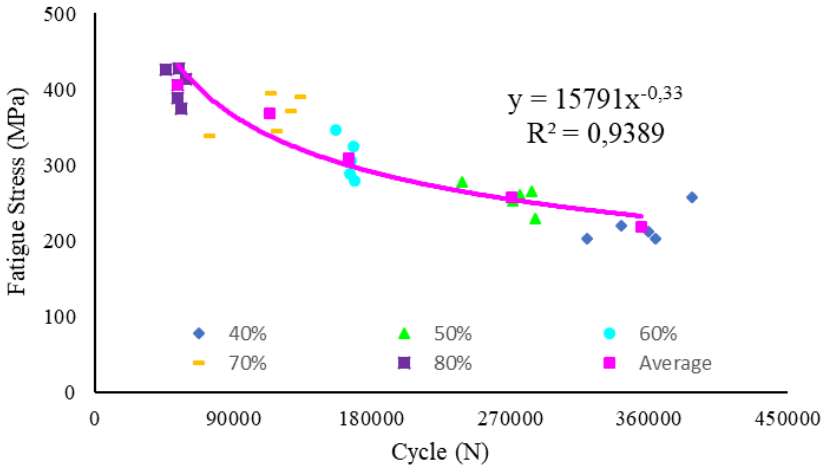

Fig. 10 S-N curve of glass/epoxy laminated composites

Table 3 shows the comparison of fatigue strength values corresponding to the number of different cycles estimated by the Power Law function with experimental data. When look at the error percentages in Table 3, it seen that the maximum error percentage for predicted values was 7.76%.

Table 3. Comparison of experimental and predictive values

Cycle	Power Law Func.		Fatigue Strength (Experimental)	Fatigue Strength (Prediction)	Error (%)
	A	B			
354800	15791	-0,33	218.64	232.76	6.46
271100			256.78	254.38	0.94
165240			308.36	299.52	2.87
113700			367.34	338.85	7.76
54000			405.7	433.23	6.79

Figure 11 showed the S-N curves obtained by experimental and the Power Law function. If assume there was no breakage, the maximum flexural fatigue stress that the glass/epoxy laminated composite could hold would have been 165.35MPa. In this case, the glass/epoxy laminated composites which were subjected to full variable bending loading up to 106 cycles lost 66.67% of their static bending strength.

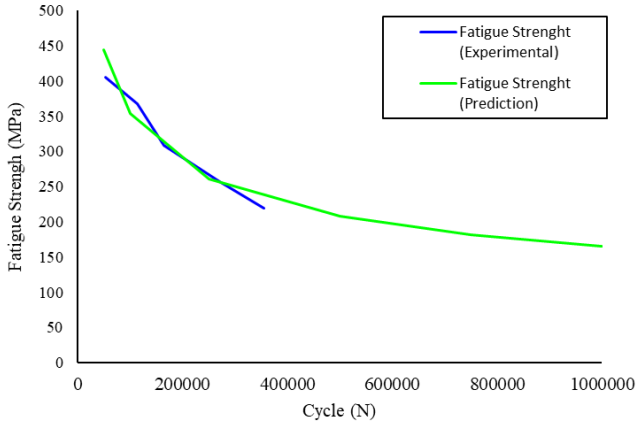

Fig. 11 Comparison of experimental and predictive of S-N curve

5. Conclusion

In this study, the static and dynamic behavior of glass/epoxy laminated composites were investigated. Tensile, compressive and flexural behavior were determined in static tests. Computer-controlled multi sample fatigue test machine, which can tire ten fatigue samples at the same time under flexural loading, have been developed for dynamic tests. Flexural fatigue strength, stiffness loss and fatigue life were determined in fatigue tests. In addition,

The general evaluations obtained in this context were given below.

- When the standard deviation values of the data obtained from the static tests were examined, it is seen that the scattering values of the data for the same experiment type are at acceptable levels. The standard deviation results show that hand lay-up is suitable for laminated composites.
- It has been found that fiber orientation directly influences the tensile and compressive strength of the material according to the tensile and compression tests. The reason for that, the density of fiber in the structure of the woven glass fabric reinforcement material is different along fiber and transverse fiber directions.
- According to the fatigue test results, it was seen that the designed flexural fatigue device is practicable for the low frequency fatigue test of plastic and composites materials. The test time per unit sample was shortened due to fatigue test capacity for 10 samples at the same time and useful software interface.
- According to the results obtained from the dynamic tests, the fatigue life decreases as the applied stress amplitude value increases. The high stress amplitude forces the material to more deformation. The increase in the amount of deformation causes the weakening of the bonds at the fiber-matrix interface. The cracks starting from the matrix material are progressed over time, causing the material to get tired earlier. In addition, the stress amplitude directly affects the form of fatigue damage such as fatigue fracture or delamination.

- Material constants for S–N power equation have been estimated for the two composite types and the agreement between this equation and the experimental data has been noticed. Based on 20% reduction of initial flexural stiffness taken as a failure criterion, the safe fatigue life areas representing the fatigue workability for glass/epoxy composite laminates have been determined.
- The Power Law function was found to be successful in predicting experimental fatigue data. It is foreseen that glass / epoxy composites which continue to 10^6 cycles without breakage damage can carry fatigue load of 165,35 MPa.

Acknowledgment

This study was sponsored by Usak University Scientific Research Coordination Agency (BAP Project Number: UBAP012014/MF013).

References

[1] Shenoi RA, Aksu S, Allen HG. Flexural fatigue characteristics of FRP sandwich beams. Fatigue Fract Eng Mater Struct 1993;16:649–662. https://doi.org/10.1111/j.1460-2695.1993.tb00109.x

[2] Nikforooz M, Montesano J, Golzar M, Shokrieh MM. Fatigue behavior of laminated glass fiber reinforced polyamide. Procedia Eng 2018;213:816–23. https://doi.org/10.1016/j.proeng.2018.02.077

[3] Bureau M., Denault J. Fatigue resistance of continuous glass fiber/polypropylene composites: consolidation dependence. Compos Sci Technol 2004;64:1785–94. https://doi.org/10.1016/j.compscitech.2004.01.016

[4] Dickson RF, Jones CJ, Harris B, Leach DC, Moore DR. The environmental fatigue behaviour of carbon fibre reinforced polyether ether ketone. J Mater Sci 1985;20:60–70. https://doi.org/10.1007/BF00555899

[5] Belingardi G, Cavatorta MP, Frasca C. Bending fatigue behavior of glass–carbon/epoxy hybrid composites. Compos Sci Technol 2006;66:222–32. https://doi.org/10.1016/j.compscitech.2005.04.031

[6] Beyene AT, Belingardi G, Koricho EG. Effect of notch on quasi-static and fatigue flexural performance of Twill E-Glass/Epoxy composite. Compos Struct 2016;153:825–42. https://doi.org/10.1016/j.compstruct.2016.05.094

[7] Koricho EG, Belingardi G, Beyene AT. Bending fatigue behavior of twill fabric E-glass/epoxy composite. Compos Struct 2014;111:169–78. https://doi.org/10.1016/j.compstruct.2013.12.032

[8] Sakin R, Ay İ, Yaman R. An investigation of bending fatigue behavior for glass-fiber reinforced polyester composite materials. Mater Des 2008;29:212–7. https://doi.org/10.1016/j.matdes.2006.11.006

[9] Liang S, Gning PB, Guillaumat L. A comparative study of fatigue behaviour of flax/epoxy and glass/epoxy composites. Compos Sci Technol 2012;72:535–43. https://doi.org/10.1016/j.compscitech.2012.01.011

[10] Ellyin F, Kujawski D. Tensile and fatigue behaviour of glassfibre/epoxy laminates. Constr Build Mater 1995;9:425–430. https://doi.org/10.1016/0950-0618(95)00073-9

[11] Kulkarni PV, Sawant PJ, Kulkarni VV. Design and Development of Plane Bending Fatigue Testing Machine for Composite Material. Mater Today Proc 2018;5.

[12] Ghielmetti C, Ghelichi R, Guagliano M, Ripamonti F, Vezzù S. Development of a fatigue test machine for high frequency applications. Procedia Eng 2011;10:2892–7. https://doi.org/10.1016/j.proeng.2011.04.480

[13] Mokhtarnia B, Layeghi M, Rasouli SH, Soltangheis B. Development of a New Device for Bending Fatigue Testing. J Test Eval 2016;44:20140347. https://doi.org/10.1520/JTE20140347

[14] Balcioğlu HE, Sakin R, Dumanay A, Gün H. Kompozit Levhalar için Ankastre-Tip Eğilmeli, Çok Numuneli Yorulma Test Makinesinin GeliştirilmesiKompozit Levhalar için Çok Numuneli Ankastre-Tip Eğilmeli. Gümüşhane Üniversitesi Fen Bilim Enstitüsü Derg 2018;8:1–17.

[15] Sakin R. Fatigue-life estimation and material selection for commercial-purity aluminum sheets. Res Eng Struct Mater 2016. https://doi.org/10.17515/resm2015.30me1205

[16] Waring G, Hofer KE, Brown I, Trabocco RE. Design and operation of multi-specimen fully reversed fatigue systems for advanced composite materials. Exp Mech 1980;20:153–161. https://doi.org/10.1007/BF02327118

[17] Yun GJ, Abdullah ABM, Binienda W. Development of a Closed-Loop High-Cycle Resonant Fatigue Testing System. Exp Mech 2012;52:275–88. https://doi.org/10.1007/s11340-011-9486-z

[18] Roudet F. Fatigue of glass/epoxy composite in three-point-bending with predominant shearing. Int J Fatigue 2002;24:327–37. https://doi.org/10.1016/S0142-1123(01)00088-3

[19] ASTM I. Standard Test Method for Tensile Properties of Polymer Matrix Composite Materials. PA 19428-2959, United States: ASTM International; 2008.

[20] ASTM D 3518/D 3518M. Standard Test Method for In-Plane Shear Response of Polymer Matrix Composite Materials by Tensile Test of a ±45° Laminate 1994.

[21] Balcioğlu HE, Aktaş M. An investigation on lateral buckling of laminated composites with delamination 2013.

[22] Kaman MO. Effect of fiber orientation on fracture toughness of laminated composite plates [0°/θ°]s. Eng Fract Mech 2011;78:2521–34. https://doi.org/10.1016/j.engfracmech.2011.06.005

[23] ASTM I. Standard Test Method for Compressive Properties of Polymer Matrix Composite Materials with Unsupported Gage Section by Shear Loading. Pennsylvania 19428-2959, United States: ASTM International; 2003.

[24] ASTM D7264/D7264M – 07. Standard Test Method for Flexural Properties of Polymer Matrix Composite Materials. ASTM International: 2015.

[25] ASTM D671-93. Standard Test Method for Flexural Fatigue of Plastics by Constant-Amplitude-of- Force 1993.

[26] Stoll MM, Weidenmann KA. Fatigue of fiber-metal-laminates with aluminum core, CFRP face sheets and elastomer interlayers (FMEL). Int J Fatigue 2018;107:110–8. https://doi.org/10.1016/j.ijfatigue.2017.10.017

Research on
Engineering
Structures & Materials
journal homepage: http://jresm.org

RESEARCH GROUP

Research Article

Natural frequencies, modes and critical velocities of top tensioned cantilever pipes conveying pressurized steady two-phase flow under thermal loading

Adeshina S. Adegoke, Ayo A. Oyediran*

Department of Mechanical Engineering, University of Lagos, Nigeria

Article Info

Article history:
Received 1 Mar 2017
Revised 14 Sep 2017
Accepted 16 Nov 2017

Keywords:
Hamilton's principle,
Cantilever pipe conveying two-phase flow,
Critical velocity,
Natural frequency,
Multiple scale perturbation technique

Abstract

This paper studied the planar dynamics of top tensioned cantilevered pipes conveying pressurized steady two-phase flow under thermal loading. The governing equations of motions were derived based on Hamilton's principle, the centerline is assumed to be extensible in order to account for possible thermal expansion; resulting to a set of coupled axial and transverse partial differential equations. Analytical approach was used to resolve the governing equations using the multiple scale perturbation technique, which aided the development of theoretical schemes for estimating the natural frequencies and mode shapes. Numerical results were presented for a case study of two phase flow of water and air with the stability and dynamic behavior of the system studied linearly via Argand diagrams which were constructed as the mixture flow velocity is increased for various void fractions. The Argand diagram assessment of the axial vibration natural frequencies shows that the attainment of the critical velocity is delayed for a cantilever pipe conveying two phase flow compared to when the pipe is conveying single phase flow. The result of the linear analysis of the transverse vibration reveals that at the critical mixture velocity, the system loses stability through Hopf bifurcation. Similarly, to the axial vibration, the attainment of the critical velocity was observed to be at higher velocities for a cantilever pipe conveying two phase flow as compared to when the pipe is conveying single phase flow. In addition to, the critical velocity is observed to be increasing as the void fraction of the two phase flow increases. The assessment of the effect of thermal loading, pressurization and top tension on the attainment of the critical velocity shows that thermal loading, pressurization and compression at the tip hastens the attainment of the critical velocity while tensioning top tension delays the attainment of the critical velocity.

1. Introduction

Instability of pipes conveying fluid are mainly of two different cases, the first is as a result of the unstable vibration caused by the fluid flow when the flow velocity surpasses a critical value and the other is a vibration due to oscillating fluid flow (Pulsating Flows). Vast publications exist on the study of the effect of internal flow on the dynamics of cantilever pipes, with most of the earlier work focusing on the linear dynamics of the pipe emphasizing on the determination of the critical velocity for the onset of flutter [1-5] for a single phase fluid. Sequel to these works, the nonlinear dynamics of pipes captivated the minds of many curious researchers which resulted to various publications on the subject; notable among these is the detail theoretical work by Semler et al [6] where a

*Corresponding author: ayooyediran@hotmail.com
DOI: http://dx.doi.org/10.17515/resm2017.16en0301

comprehensive nonlinear equation was derived for a cantilever pipe based on inextensible theory. However, existing publications on the dynamics of fluid-conveying cantilevered pipes taking into account extensibility is rare with the pioneering work by Ghayesh et al [7], where he studied the nonlinear dynamics of cantilevered extensible pipe conveying single phase fluid without thermal loading, he observed that conversely to inextensible pipe, an extensible pipe elongates in the axial direction as the flow velocity increases.

The combined thermal and pressurization effect on the instability of pipes is not an area with vast historical research trends. However, recent findings on the contributions of transient temperature to pipe walking prompted some studies on this subject, Qian et al. [8], studied the instability of simply supported pipes conveying fluid under thermal loads and discovered that the critical fluid velocity decreases with increasing temperature. Another interesting result of Marakala et al [9] reveals that the frequency of vibration increases with increase in pressure and decreases with increase in temperature. The increase in pressure increases the velocity of the fluid flow and reduces the damping effect. Temperature has an effect on displacement as well as frequency, since thermal contraction and expansion increases due to high heat transfer rate at high velocity. As the temperature of the fluid increases, the frequency decreases due to softening effect of tube. However, these publications were on the dynamics of a simply supported pipe.

Two phase flow is a common flow phenomenon in various industrial pipes, but very few publications exist on the instability behavior of pipes conveying two phase flow. Miwa et al [10] did an in-depth review of the extent of existing work on two-phase flow induced vibrations, stating that there exist very few researches on the instability behavior of pipes due to internal two phase flow. In his review, Miwa et al explains that internal two phase flow induced vibration can be initiated by various hydrodynamic phenomena, depending on the geometrical configurations of the flow channels and operating conditions, gas-liquid two phase flow may create vibrations with various modes of amplitude and frequency. Young and Qiang [11] highlighted that in gas and liquid transportation, the gas and the liquid normally do not travel at the same velocity in the pipeline because of difference in viscosities, for an upward flow in a vertical pipe, the gas phase will flow at higher velocity than the liquid because it is denser and less viscous while in a downward flow, the gas is slower as a result of variation in densities. Monette and Pettigrew [12] presents an excellent experimental paper on the fluidelastic instability of flexible tubes subjected to two-phase flow which might be one of the premier paper on the dynamics of pipe conveying two phase flow, where experimental results were compared with the theoretical estimations and also reveals the relationship between the void fraction and the dynamics of the pipe for a two phase liquid-gas flow.

Majority of the existing publications focused on single phase flow, not many considered thermal effect, and most of the existing equations of motion for cantilever pipe conveying fluids are based on the inextensible theory. However, there seems to be some gaps on the study of combined effect of Multiphase flow and thermal effect on the dynamics of cantilever pipes conveying fluids. This present study investigates the dynamics of top tensioned cantilever pipes conveying pressurized steady two-phase flow under thermal loading. Approximate analytical approach is used to resolve the governing equations by imposing the method of multiple scales perturbation technique directly to the systems equations (direct-perturbation method).

2. Problem Formulation and Modelling

Considering a system of cantilever cylindrical pipe of length (L), having a cross-sectional area (A), mass per unit length (m_p) and flexural rigidity (EI), conveying multiphase flow, and flowing parallel to the pipe's center line.

The center line axis of the pipe in its undeformed state is assumed to overlaps with the Y axis and the cylinder is assumed to vibrate in the (Y, X) plane (see fig. 1). To derive the system's governing equations of motion, the following basic assumptions were made for the cylinder and the fluid: (i) the mean flow velocity is constant; (ii) the cylinder is slender, so that the Euler–Bernoulli beam theory is applicable; (iii) although the deflections of the cylinder may be large, the strains are small; (iv) the cylinder centreline is extensible.

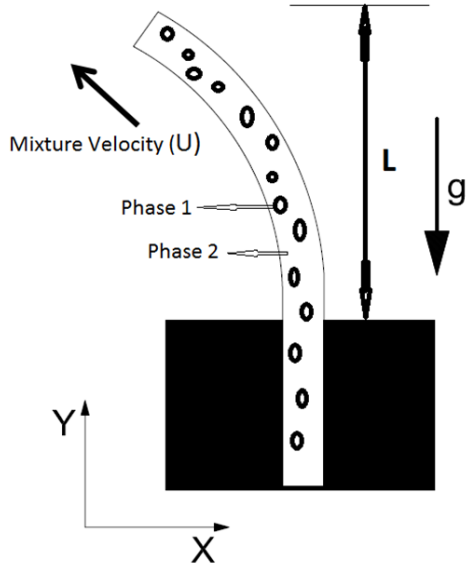

Fig. 1 System's Schematics

The centerline of the cantilever pipe is assumed extensible so as to account for possible expansion due to the high temperature of the fluid content. Semler et al [6] expressed the geometric relation of the centerline of an extensible pipe as:

$$1+\epsilon(\mathrm{Y})=\sqrt{\left[1+\frac{\partial \mathrm{u}}{\partial \mathrm{Y}}\right]^{2}+\left[\frac{\partial \mathrm{v}}{\partial \mathrm{Y}}\right]^{2}} \tag{1}$$

$\epsilon(\mathrm{Y})$ is the axial strain along the pipe's centerline.

Assuming θ to be the angle between the pipe's centerline and the Y- axis, this can be defined as:

$$\cos\theta=\frac{1+\partial \mathrm{u}/\mathrm{dY}}{1+\epsilon(\mathrm{Y})}, \qquad \sin\theta=\frac{\partial \mathrm{v}/\mathrm{dY}}{1+\epsilon(\mathrm{Y})} \tag{2}$$

The curvature k is related to the geometry as:

$$\mathrm{k}=\frac{1}{1+\epsilon}\frac{\partial\theta}{\partial \mathrm{Y}} \tag{3}$$

The derivative in Eq. (3) can be obtained from Eq. (2) as:

$$\frac{\partial\theta}{\partial Y}=\frac{\left[\frac{\partial^2 v}{\partial Y^2}\left(1+\frac{\partial u}{\partial Y}\right)-\frac{\partial v}{\partial Y}\frac{\partial^2 u}{\partial Y^2}\right]}{(1+\epsilon)^2} \tag{4}$$

The second derivative is expressed adopting Lagrange notations as:

$$\left(\frac{\partial\theta}{\partial Y}\right)^2 = v''^2 - 2v''^2u' - 2v''^2u''^2 - 2v'v''u'' \tag{5}$$

2.1. Derivation of the Equation of Motion

The equations of motion are derived using the energy method. The energy method is based on the Hamilton's principle, which is defined as the variations of the time derivative of the Lagrangian. This can be mathematically expressed as:

$$\delta\int_{t1}^{t2}\mathcal{L}\,dt=\int_{t1}^{t2}\sum_{j=1}^{n}M_jU_j\left(\dot{r}_L+\sum_{j=1}^{n}U_j\tau_L\right)\delta r_L\,dt, \tag{6}$$

Where

n is the number of phases in the fluid, which will be 2 for a two phase flow

M_j is the mass of the phases in the fluid

U_j is the flow velocity of the phases in the fluid

$\mathcal{L}$ is the Lagrangian operator which is expressed as:

$$\mathcal{L}=\mathcal{T}_f+\mathcal{T}_p-\mathcal{V}_f-\mathcal{V}_{p,} \tag{7}$$

$\mathcal{T}_p$ and $\mathcal{V}_p$ are the kinetic and potential energies of the pipe, and $\mathcal{T}_f$ and $\mathcal{V}_f$ are the kinetic and potential energies associated with the conveyed fluid.

The following expressions hold:

$\dot{r}_L=\dot{u}_Li+\dot{v}_Lk$ and $\tau_L=u'_Li+v'_Lk$

2.1.1. Kinetic Energy

The total kinetic energy of the system is the summation of the kinetic energy of the pipe and the kinetic energies of the phases/components of the flowing fluid.

The velocity vector of the pipe's centerline is expressed as:

$$\vec{V}_p=\frac{\partial u}{\partial t}\hat{i}+\frac{\partial v}{\partial t}\hat{j} \tag{8}$$

Therefore, the kinetic energy of the pipe is expressed as:

$$\mathcal{T}_p=\frac{1}{2}m_p\int_0^L\left[\left(\frac{\partial u}{\partial t}\right)^2+\left(\frac{\partial v}{\partial t}\right)^2\right]dx \tag{9}$$

As illustrated by Semler et al [6], the axial elongation of the pipe is complemented by a lateral contraction, due to the Poisson effect. This will impact the flow velocity of the fluid phases/components such that:

$$\sum_{j=1}^{n} U_j = [(1+\epsilon)/(1+a\epsilon)] \sum_{j=1}^{n} U_{0_j} \tag{10}$$

Where U_{0_j} and U_j are the flow velocities before and after elongation, the subscript (j) is used to identify the various phases/components of the conveyed fluid, (ϵ) is the axial strain and (a) relates to the Poisson ratio (v) as $a = 1 - 2v$; for an extreme case $v = 0.5$ and a becomes zero Ghayesh [7].

The flow velocity relative to the centerline axis of the pipe is expressed as:

$$\vec{V}_f = \left\{\frac{\partial u}{\partial t} + \sum_{j=1}^{n} U_j(1-a\epsilon)\left(1+\frac{\partial u}{\partial x}\right)\right\}\hat{\imath} + \left\{\frac{\partial v}{\partial t} + \sum_{j=1}^{n} U_j(1-a\epsilon)\left(\frac{\partial v}{\partial x}\right)\right\}\hat{\jmath} \tag{11}$$

Therefore, the Kinetic energy of the conveyed fluid is expressed as:

$$\mathcal{T}_f = \frac{1}{2}\sum_{j=1}^{n} M_j \int_0^L \left\{\left(\frac{\partial u}{\partial t}\right)^2 + \left(\frac{\partial v}{\partial t}\right)^2 + U_j{}^2\left[1 + 2\frac{\partial u}{\partial x} + \left(\frac{\partial u}{\partial x}\right)^2 - 2a\left(\frac{\partial u}{\partial x} + \frac{1}{2}\left(\frac{\partial v}{\partial x}\right)^2\right) + \left(\frac{\partial v}{\partial x}\right)^2\right] + 2U_j\left[\frac{\partial u}{\partial t}\left(1+\frac{\partial u}{\partial x}\right) + \frac{\partial v}{\partial t}\frac{\partial v}{\partial x}\right]\right\} dx \tag{12}$$

Summing Eq. (9) and Eq. (12) to have the total kinetic energy of the system and then considering the variations:

$$\begin{aligned}\delta\int_{t1}^{t2}(KE)dt = {} & \left(m_p + \sum_{j=1}^{n} M_j\right)\iint\left(\frac{\partial u}{\partial t}\delta\left(\frac{\partial u}{\partial t}\right) + \frac{\partial v}{\partial t}\delta\left(\frac{\partial v}{\partial t}\right)\right)dxdt \\ & + \sum_{j=1}^{n} M_j \iint\left(U_j{}^2\left[\delta\left(\frac{\partial u}{\partial x}\right) + \frac{\partial u}{\partial x}\delta\left(\frac{\partial u}{\partial x}\right)\right.\right. \\ & \left. - a\left(\delta\left(\frac{\partial u}{\partial x}\right) + \frac{\partial v}{\partial x}\delta\left(\frac{\partial v}{\partial x}\right)\right) + \frac{\partial v}{\partial x}\delta\left(\frac{\partial v}{\partial x}\right)\right] \\ & + 2U_j\left[\delta\left(\frac{\partial u}{\partial t}\right) + \frac{\partial u}{\partial t}\delta\left(\frac{\partial u}{\partial x}\right) + \frac{\partial u}{\partial x}\delta\left(\frac{\partial u}{\partial t}\right) + \frac{\partial v}{\partial t}\delta\left(\frac{\partial v}{\partial x}\right)\right. \\ & \left.\left. + \frac{\partial v}{\partial x}\delta\left(\frac{\partial v}{\partial t}\right)\right]\right)dxdt\end{aligned} \tag{13}$$

Integrating Eq. (13) and adopting the Lagrange notations for the variations in space and Newton notations for the variations in time, the terms varying in space and time are grouped as;

$$\delta\int_{t1}^{t2}(KE)dt = \iint\left[-\left(m_p+\sum_{j=1}^{n}M_j\right)(\ddot{u}\delta u+\ddot{v}\delta v) - \sum_{j=1}^{n}M_j{U_j}^2(u''\delta u - av''\delta v + v''\delta v) - \sum_{j=1}^{n}M_j\dot{U}_j\delta u - \sum_{j=1}^{n}2M_jU_j\dot{u}'\delta u - \sum_{j=1}^{n}M_j\dot{U}_ju'\delta u - \sum_{j=1}^{n}2M_jU_j\dot{v}'\delta v - \sum_{j=1}^{n}M_j\dot{U}_jv'\delta v\right]dxdt + \sum_{j=1}^{n}M_jU_j\int_{t1}^{t2}[\dot{u}_L\delta u+\dot{v}_L\delta v]dt \quad (14)$$

2.1.2. Potential Energy

Semler et al [6] highlighted that the potential energy is as a result of the elastic deformation of the pipe and the effect of gravity. The deformation from elastic behavior of the pipe can be linked to the strain energy, which is expressed by Semler at al [6] as:

$$\mathcal{V}_p = \frac{1}{2}EA\int_0^L\epsilon^2dx + \frac{1}{2}EI\int_0^L(1+\epsilon)^2k^2dx \quad (15)$$

This is clearly the combinations of the axial strain effect and the bending strain effect where (E) denotes the Young's modulus, (I) denotes the pipe moment of inertia, (A) denotes the cross-sectional area, (ϵ) is the axial strain and (k) is the curvature term as expressed in Eq. (3).

The thermal effect can be introduced by considering the linear strain tensor as a sum of the strain contributions from the mechanical stress and the thermal effect. Semler et al [6] further decomposed the axial strain into a steady strain component due to externally applied tension (T_0) and pressure force component ($P = pA$) and an oscillatory strain component due to the oscillations of the pipe. These can be expressed as:

$$\epsilon_{ij} = {\epsilon_{ij}}^{\sigma} + {\epsilon_{ij}}^{\Delta} + \frac{T_0 - P}{EA} \quad (16)$$

While the stress contributing strain component can be obtained through the binomial expansion of Eq. (1) as:

$${\epsilon_{ij}}^{\sigma} = \frac{\partial u}{\partial x} - \frac{1}{2}\left(\frac{\partial u}{\partial x}\right)\left(\frac{\partial v}{\partial x}\right)^2 + \frac{1}{2}\left(\frac{\partial v}{\partial x}\right)^2 - \frac{1}{8}\left(\frac{\partial v}{\partial x}\right)^4 \quad (17)$$

Considering that the gradient of the transverse displacement of the pipe is far greater than the gradient of the longitudinal displacement $\left(\frac{\partial v}{\partial x} > \frac{\partial u}{\partial x}\right)$. Also, the thermal contributing strain component can be expressed in terms of the thermal expansively (α) and the difference in temperatures (ΔT) as:

$${\epsilon_{ij}}^{\Delta} = (-\alpha\Delta T) \quad (18)$$

Substituting Eq. (17) and Eq. (18) into Eq. (16) and then substituting Eq. (16), Eq. (3) and Eq. (5) in to Eq. (15) resulting to:

$$\mathcal{V}_p = \frac{1}{2}EA\int_0^L \left[\left(u' - \frac{1}{2}u'v'^2 + \frac{1}{2}v'^2 - \frac{1}{8}v'^4\right) + \frac{T_0 - P}{EA} + (-\alpha\Delta T)\right]^2 dx + \frac{1}{2}EI\int_0^L \left[v''^2 - 2v''^2u' - 2v''^2u''^2 - 2v'v''u''\right]dx \tag{19}$$

With the reference plane in the same direction as the gravitational acceleration, the effect of gravity can be expressed as:

$$\mathcal{V}_g = g\left(\sum_{j=1}^{n} M_j + m\right)\int_0^L (x+u)dx \tag{20}$$

Combining equations (19) and (20), the potential energy of the system is expressed as:

$$\begin{aligned}\delta\int_{t1}^{t2}(PE)dt = EA\iint &\left[\left(\frac{T_0 - P}{EA} - (\alpha\Delta T)\right)\left(\delta u' - u'v'\delta v' - \frac{1}{2}v'^2\delta u' + v'\delta v' - \frac{1}{2}v'^3\delta v'\right)\right.\\ &+ \left(u' - \frac{1}{2}u'v'^2 + \frac{1}{2}v'^2 - \frac{1}{8}v'^4\right)\left(\delta u' - u'v'\delta v' - \frac{1}{2}v'^2\delta u' + v'\delta v' - \frac{1}{2}v'^3\delta v'\right)\Big]dxdt\\ &+ EI\iint\left[v''\delta v'' - v''\delta u' - 2u'v''\delta v'' - 2v''^2v'\delta v' - 2v'^2v''\delta v'' - v'v''\delta u'' - v'u''\delta v'' - v''u''\delta v'\right]dxdt\\ &+ g\left(\sum_{j=1}^{n} M_j + m\right)\int_0^L(\delta u)dxdt\end{aligned} \tag{21}$$

According to Semler at al [6], for a pipe of length L=1, with $|u|\sim 0.01, and\ |v|\sim 0.1$, neglecting terms of the order 0.0001 and below.

Integrating Eq. (21) and collecting terms that varies in time and space as:

$$\begin{aligned}\delta\int_{t1}^{t2}(PE)dt = \iint &(-EAu''\delta u - EA(u'v'' + v'u'')\delta v\\ &- EA\left(\frac{3}{2}v'^2v''\right)\delta v\\ &+ (T_0 - P - EA(\alpha\Delta T))(u'v'' + v'u'')\delta v\\ &+ (T_0 - P - EA(\alpha\Delta T))\left(\frac{3}{2}v'^2v''\right)\delta v - EAv'v''\delta u\\ &+ (T_0 - P - EA(\alpha\Delta T))v''\delta v\\ &+ (T_0 - P - EA(\alpha\Delta T))v'v''\delta u + EIv''''\delta v\\ &- EI(v''''v' + v''v''')\delta u\\ &- EI\left(3u'''v'' + 4v'''u'' + 2u'v'''' + 2v'^2v'''' + 8v'v''v''' + 2v''^3\right)\delta v - (T_0 - P - EA(\alpha\Delta T))'\delta u\\ &+ \left(m + \sum_{j=1}^{n} M_j\right)g\delta u)dxdt\end{aligned} \tag{22}$$

2.1.3. Non-Conservative Work Done

As illustrated by Sinir [13], the damping effect can be accounted for by taking the first variations of the non-conservative force:

$$\int_{t1}^{t2} \delta W_{nc} = \int_{t1}^{t2} c\dot{v}\delta v dt \tag{23}$$

where c is the coefficient of viscous damping. Also, the right hand side term of the Hamilton's equation (6):

$$\text{rhs} = \sum_{j=1}^{n} M_j U_j \int_{t1}^{t2} \left[\left(\dot{u}_L + \sum_{j=1}^{n} U_j u'_L \right) \delta u + \left(\dot{v}_L + \sum_{j=1}^{n} U_j v'_L \right) \delta v \right] dt = 0 \tag{24}$$

$$= \sum_{j=1}^{n} M_j U_j \int_{t1}^{t2} (\dot{u}_L \delta u + \dot{v}_L \delta v) dt + \sum_{j=1}^{n} M_j U^2{}_j \int_{t1}^{t2} \left(u'_L \delta u + v'_L \delta v \right) dt \tag{25}$$

The first term of equation (25) is identical to the last term of equation (14), therefore the rhs becomes:

$$\sum_{j=1}^{n} M_j U^2{}_j \int_{t1}^{t2} \left(u'_L \delta u + v'_L \delta v \right) dt \tag{26}$$

Physically, this implies a non-classical boundary condition at the free end for a discharging cantilever pipe:

$$EI v'''_L = \sum_{j=1}^{n} M_j U^2{}_j \int_{t1}^{t2} v'_L \delta v dt \tag{27}$$

Thus, a force is imposed at the free end if the velocity of the exiting fluid is not tangential to the pipe. However this study assumes that the exiting flow remains tangential to the pipe at the free end, therefore classical boundary condition holds at the free end.

2.2. Equation of Motion for Multiphase Flow

Summing equations (14), (22), (23) and (25), the system's equation of motion can be expressed as:

$$\begin{aligned} &\left(m + \sum_{j=1}^{n} M_j \right) \ddot{u} + \sum_{j=1}^{n} M_j \dot{U}_j + \sum_{j=1}^{n} 2 M_j U_j \dot{u}' + \sum_{j=1}^{n} M_j U_j{}^2 u'' + \sum_{j=1}^{n} M_j \dot{U}_j u' \\ &- EAu'' - EI\left(v'''' v' + v'' v''' \right) \\ &+ (T_0 - P - EA(\alpha \Delta T) - EA) v' v'' \\ &- \left(T_0 - P - EA(\alpha \Delta T) \right)' + \left(m + \sum_{j=1}^{n} M_j \right) g = 0 \end{aligned} \tag{28}$$

$$\left(m+\sum_{j=1}^{n}M_j\right)\ddot{v}+\sum_{j=1}^{n}2M_jU_j\dot{v}'+\sum_{j=1}^{n}M_j\,{U_j}^2v''-\sum_{j=1}^{n}aM_j\,{U_j}^2v''+\sum_{j=1}^{n}M_j\dot{U}_jv' + EIv'''' - \left(T_0-P-EA(\alpha\Delta T)\right)v'' + C\dot{v} - EI\left(3u'''v''+4v'''u''+2u'v''''+2{v'}^2v''''+8v'v''v'''+2{v''}^3\right) + (T_0-P-EA(\alpha\Delta T)-EA)\left(u'v''+v'u''+\frac{3}{2}{v'}^2v''\right)=0 \tag{29}$$

The associated boundary conditions are:

$$v(0)=v'(0)\ and\ v''(L)=v'''(L)=0 \tag{30}$$

$$u(0)=u'(L)=0 \tag{31}$$

Where the terms represent:

The inertia force terms: $\left(m+\sum_{j=1}^{n}M_j\right)\ddot{u}\ and\ \left(m+\sum_{j=1}^{n}M_j\right)\ddot{v}$

The Coriolis force: $\sum_{j=1}^{n}2M_jU_j\dot{u}'\ \ and\ \sum_{j=1}^{n}2M_jU_j\dot{v}'$

The centrifugal force: $\sum_{j=1}^{n}M_j\,{U_j}^2u''\ and\ a\sum_{j=1}^{n}M_j\,{U_j}^2v''$

The forces due to gravity:$\left(m+\sum_{j=1}^{n}M_j\right)g$

The bending stiffness term: EIv''''

The axial stiffness term: EAu''

The damping term: $C\dot{v}$

The forces due to unsteady flow: $\sum_{j=1}^{n}M_j\dot{U}_j$

The gradient terms: $\left(T_0-P-EA(\alpha\Delta T)\right)'$

Equations (28), (29), (30) and (31) are the governing equations and boundary conditions for a tensioned cantilever pipe conveying pressurized unsteady multiphase flow under thermal loading.

2.2.1. Dimensionless Equation of Motion for Multiphase Flow

The equation of motion may be rendered dimensionless to make the analysis of the system more robust and not constraint to one specific system by introducing the following non-dimensional quantities;

$$\bar{u}=\frac{u}{L}\ ,\quad \bar{v}=\frac{v}{L}\ ,\quad \bar{t}=\left[\frac{EI}{\sum M_j+m}\right]^{1/2}\frac{t}{L^2}\ ,\quad \bar{U}_j=\left[\frac{M_j}{EI}\right]^{1/2}UL\ , \qquad \gamma=\frac{\sum M_j+m}{EI}L^3g, \tag{32}$$

$$\beta_j=\frac{M_j}{\sum M_j+m},\quad \Psi_j=\frac{M_j}{\sum M_j},\ Damping\ term:\mu=\frac{CL^2}{\sqrt{\sum(M_j+m)EI}}$$

$$Tension:\Pi_0=\frac{T_oL^2}{EI}\ ,Flexibility:\Pi_1=\frac{EAL^2}{EI},\qquad Presure:\Pi_2=\frac{PL^2}{EI}$$

$$\begin{aligned}\ddot{\bar{u}} + \sum_{j=1}^{n} \dot{\bar{U}}_j \sqrt{\Psi_j}\sqrt{\beta_j} + 2\sum_{j=1}^{n} \bar{U}_j \sqrt{\Psi_j}\sqrt{\beta_j}\dot{\bar{u}}' + \sum_{j=1}^{n} \Psi_j \bar{U}_j{}^2 \bar{u}'' + \sum_{j=1}^{n} \dot{\bar{U}}_j \sqrt{\Psi_j}\sqrt{\beta_j}\bar{u}' \\ - \Pi_1 \bar{u}'' - \left(\bar{v}''''\bar{v}' + \bar{v}''\bar{v}'''\right) \\ + (\Pi_0 - \Pi_2 - \Pi_1(\alpha\Delta T) - \Pi_1)\bar{v}'\bar{v}'' \\ - \left(\Pi_0 - \Pi_2 - \Pi_1(\alpha\Delta T)\right)' + \gamma = 0\end{aligned}$$

$$\begin{aligned}\ddot{\bar{v}} + 2\sum_{j=1}^{n} \bar{U}_j \sqrt{\Psi_j}\sqrt{\beta_j}\dot{\bar{v}}' + \sum_{j=1}^{n} \Psi_j \bar{U}_j{}^2 \bar{v}'' - a\sum_{j=1}^{n} \Psi_j \bar{U}_j{}^2 \bar{v}'' + \sum_{j=1}^{n} \dot{\bar{U}}_j \sqrt{\Psi_j}\sqrt{\beta_j}\bar{v}' \\ - \left(\Pi_0 - \Pi_2 - \Pi_1(\alpha\Delta T)\right)v'' + \bar{v}'''' + \mu\dot{v} \\ - \left(3\bar{u}''''\bar{v}'' + 4\bar{v}''''\bar{u}'' + 2\bar{u}'\bar{v}'''' + 2\bar{v}'^2\bar{v}'''' + 8\bar{v}'\bar{v}''\bar{v}'''\right. \\ \left. + 2\bar{v}''^3\right) \\ + (\Pi_0 - \Pi_2 - \Pi_1(\alpha\Delta T) - \Pi_1)\left(\bar{u}'\bar{v}'' + \bar{v}'\bar{u}'' + \frac{3}{2}\bar{v}'^2\bar{v}''\right) \\ = 0\end{aligned} \tag{33}$$

The dimensionless boundary conditions are:

$$\bar{v}(0) = \bar{v}'(0) \; and \; \bar{v}''(L) = \bar{v}'''(L) = 0 \tag{34}$$

$$\bar{u}(0) = \bar{u}'(L) = 0 \tag{35}$$

In these equations, $\bar{u}$ *and* $\bar{v}$ are respectively, the dimensionless displacements in the longitudinal and transverse direction, $(\bar{U}_j)$ is the flow velocities of the constituent phases/components used in the parametric studies of the dynamics of the system, (β_j) is the mass ratio same as in single phase flows as derived by Semler et al [6] and Paidoussis [20], (Ψ_j) is another mass ratio which is unique to multiphase flow relating the fluid mass independent of the mass of the pipe, (γ) is the gravity term, (μ) is the damping term and (Π_0, Π_1, Π_2) represent the Tension term, Flexibility term and the pressurization term respectively.

2.2.2. Dimensionless Equation of Motion for Two Phase Flow

The governing equation can be reduced to that of a two phase as:

$$\begin{aligned}\ddot{\bar{u}} + \dot{\bar{U}}_1\sqrt{\Psi_1}\sqrt{\beta_1} + \dot{\bar{U}}_2\sqrt{\Psi_2}\sqrt{\beta_2} + 2\bar{U}_1\sqrt{\Psi_1}\sqrt{\beta_1}\dot{\bar{u}}' + 2\bar{U}_2\sqrt{\Psi_2}\sqrt{\beta_2}\dot{\bar{u}}' \\ + \Psi_1\bar{U}_1{}^2\bar{u}'' + \Psi_2\bar{U}_2{}^2\bar{u}'' + \dot{\bar{U}}_1\sqrt{\Psi_1}\sqrt{\beta_1}\bar{u}' \\ + \dot{\bar{U}}_2\sqrt{\Psi_2}\sqrt{\beta_2}\bar{u}' - \Pi_1\bar{u}'' - \left(\bar{v}''''\bar{v}' + \bar{v}''\bar{v}'''\right) \\ + (\Pi_0 - \Pi_2 - \Pi_1(\alpha\Delta T) - \Pi_1)\bar{v}'\bar{v}'' \\ - \left(\Pi_0 - \Pi_2 - \Pi_1(\alpha\Delta T)\right)' + \gamma = 0\end{aligned} \tag{36}$$

$$\begin{aligned}\ddot{\bar{v}} + 2\bar{U}_1\sqrt{\Psi_1}\sqrt{\beta_1}\dot{\bar{v}}' + 2\bar{U}_2\sqrt{\Psi_2}\sqrt{\beta_2}\dot{\bar{v}}' + \Psi_1\bar{U}_1{}^2\bar{v}'' + \Psi_2\bar{U}_2{}^2\bar{v}'' - a\Psi_1\bar{U}_1{}^2\bar{v}'' \\ - a\Psi_2\bar{U}_2{}^2\bar{v}'' + \mu\dot{v} + \dot{\bar{U}}_1\sqrt{\Psi_1}\sqrt{\beta_1}\bar{v}' + \dot{\bar{U}}_2\sqrt{\Psi_2}\sqrt{\beta_2}\bar{v}' \\ - \left(\Pi_0 - \Pi_2 - \Pi_1(\alpha\Delta T)\right)v'' + \bar{v}'''' \\ - \left(3\bar{u}''''\bar{v}'' + 4\bar{v}''''\bar{u}'' + 2\bar{u}'\bar{v}'''' + 2\bar{v}'^2\bar{v}'''' + 8\bar{v}'\bar{v}''\bar{v}'''\right. \\ \left. + 2\bar{v}''^3\right) \\ + (\Pi_0 - \Pi_2 - \Pi_1(\alpha\Delta T) - \Pi_2)\left(\bar{u}'\bar{v}'' + \bar{v}'\bar{u}'' + \frac{3}{2}\bar{v}'^2\bar{v}''\right) \\ = 0\end{aligned} \tag{37}$$

The associated boundary conditions are:

$$\bar{v}(0) = \bar{v}'(0) \; and \; \bar{v}''(L) = \bar{v}'''(L) = 0 \tag{38}$$

$$\bar{u}(0) = \bar{u}'(L) = 0 \tag{39}$$

2.2.3. Governing Equation for a steady two phase flow

$$\ddot{\bar{u}} + \bar{U}_1 C21\dot{\bar{u}}' + \bar{U}_2 C22\dot{\bar{u}}' + C31\overline{U_1}^2\bar{u}'' + C32\overline{U_2}^2\bar{u}'' - C5\bar{u}'' - \left(\bar{v}''''\bar{v}' + \bar{v}''\bar{v}'''\right) + C6\bar{v}'\bar{v}'' - C7' + \gamma = 0 \tag{40}$$

$$\ddot{\bar{v}} + \bar{U}_1 C21\dot{\bar{v}}' + \bar{U}_2 C22\dot{\bar{v}}' + C31\overline{U_1}^2\bar{v}'' + C32\overline{U_2}^2\bar{v}'' - aC31\overline{U_1}^2\bar{v}'' - aC32\overline{U_2}^2\bar{v}'' + Cm\dot{v} - C7v'' + \bar{v}'''' - \left(3\bar{u}'''\bar{v}'' + 4\bar{v}'''\bar{u}'' + 2\bar{u}'\bar{v}'''' + 2\bar{v}'^2\bar{v}'''' + 8\bar{v}'\bar{v}''\bar{v}''' + 2\bar{v}''^3\right) + C6\left(\bar{u}'\bar{v}'' + \bar{v}'\bar{u}'' + \frac{3}{2}\bar{v}'^2\bar{v}''\right) = 0 \tag{41}$$

For a steady flow, velocities are not changing with time, therefore;

$$\dot{\overline{U_1}} = \dot{\overline{U_2}} = 0 \tag{42}$$

The associated boundary conditions are:

$$\bar{v}(0) = \bar{v}'(0) \; and \; \bar{v}''(L) = \bar{v}'''(L) = 0 \tag{43}$$

$$\bar{u}(0) = \bar{u}'(L) = 0 \tag{44}$$

Equations (40) to (44) are obtained using the notations:

$C21 = 2\sqrt{\Psi_1}\sqrt{\beta_1}$

$C22 = 2\sqrt{\Psi_2}\sqrt{\beta_2}$

$C31 = \Psi_1$

$C32 = \Psi_2$

$C41 = C11$

$C42 = C12$

$C5 = \Pi_1$

$C6 = \Pi_0 - \Pi_2 - \Pi_1(\alpha\Delta T) - \Pi_1$

$C7 = \Pi_0 - \Pi_2 - \Pi_1(\alpha\Delta T)$

$Cm = \mu$

2.3. Empirical Gas–Liquid Two-Phase Flow Model

The components velocities in terms of the superficial velocities are expressed as:

$$V_g = U_g vf, \quad V_l = U_l(1 - vf) \tag{45}$$

Where U_g and U_l are the superficial flow velocities. Adopting the Chisholm empirical relations Woldesemayat and Ghajar [14], Void fraction:

$$vf = \left[1 + \sqrt{1 - \mathrm{x}\left(1 - \frac{\rho_l}{\rho_g}\right)}\left(\frac{1-\mathrm{x}}{\mathrm{x}}\right)\left(\frac{\rho_g}{\rho_l}\right)\right]^{-1} \tag{46}$$

Slip Ratio:

$$S = \frac{V_g}{V_l} = \left[1 - \mathrm{x}\left(1 - \frac{\rho_l}{\rho_g}\right)\right]^{1/2} \tag{47}$$

The vapour quality: (x) The densities of the liquid and gas phases respectively: (ρ_l and ρ_g)
Mixture Velocity:

$$V_T = U_g vf + U_l(1 - vf) \tag{48}$$

Individual Velocities:

$$V_l = \frac{V_T}{S+1}, V_g = \frac{SV_T}{S+1} \tag{49}$$

For various void fractions (0.1, 0.3, 0.5, 0.7 and 0.9) and a series of mixture velocities, the corresponding slip ratio and individual velocities are estimated and used for numerical calculations.

Single phase flow velocity can be recovered by making the slip ratio to be zero.

3. Method of Solution

Exact solutions of nonlinear equations are almost not available; an approximate solution will be sought for by utilizing the multiple time scale perturbation technique. This approach is applied directly to the partial differential equations (40) and (41), given that the common method of discretizing the equations first and then applying perturbation method yields less accurate results for finite mode truncations and higher order perturbation schemes [15-18].

Adopting perturbation techniques, it is necessary to decide the terms to be considered small or weak. However, the study considers the contributions of the nonlinear terms, damping term, gradient term and gravity term to be small compared to the linear terms.

The damping coefficient is ordered so that the effect of damping and nonlinearity appear in the same perturbation equation.

$$\begin{aligned} \ddot{\bar{u}} + \bar{U}_1 C21\dot{\bar{u}}' + \bar{U}_2 C22\dot{\bar{u}}' + C31\overline{U_1}^2\bar{u}'' + C32\overline{U_2}^2\bar{u}'' - C5\bar{u}'' \\ + \varepsilon\left(-\left(\bar{v}''''\bar{v}' + \bar{v}''\bar{v}'''\right) + C6\bar{v}'\bar{v}'' - C7' + \gamma\right) = 0 \end{aligned} \tag{50}$$

$$\begin{aligned} \ddot{\bar{v}} + \bar{U}_1 C21\dot{\bar{v}}' + \bar{U}_2 C22\dot{\bar{v}}' + C31\overline{U_1}^2\bar{v}'' + C32\overline{U_2}^2\bar{v}'' - aC31\overline{U_1}^2\bar{v}'' \\ - aC32\overline{U_2}^2\bar{v}'' + \varepsilon Cm\dot{v} - C7v'' + \bar{v}'''' \\ + \varepsilon\left(-\left(3\bar{u}'''\bar{v}'' + 4\bar{v}'''\bar{u}'' + 2\bar{u}'\bar{v}'''' + 2\bar{v}'^2\bar{v}'''' \right.\right. \\ \left.\left. + 8\bar{v}'\bar{v}''\bar{v}''' + 2\bar{v}''^3\right) + C6\left(\bar{u}'\bar{v}'' + \bar{v}'\bar{u}'' + \frac{3}{2}\bar{v}'^2\bar{v}''\right)\right) \\ = 0 \end{aligned} \tag{51}$$

We seek an approximate solution for $\bar{u}$ *and* $\bar{v}$ of the form:

$$\bar{u} = \bar{u}_0(T_0, T_1) + \varepsilon\bar{u}_1(T_0, T_1) + \varepsilon^2\bar{u}_2(T_0, T_1) + \cdots \quad (52)$$

$$\bar{v} = \bar{v}_0(T_0, T_1) + \varepsilon\bar{v}_1(T_0, T_1) + \varepsilon^2\bar{v}_2(T_0, T_1) + \cdots \quad (53)$$

Two time scales are needed $T_0 = t$ and $T_1 = \varepsilon t$

Where ε is a small dimensionless measure of the amplitude of $\bar{u}$ and $\bar{v}$, used as a book-keeping parameter. Then, the time derivatives are:

$$\frac{d}{dt} = D_0 + \varepsilon D_1 + \varepsilon^2 D_2 + \ldots \quad (54)$$

$$\frac{d^2}{dt^2} = {D_0}^2 + 2\varepsilon D_0 D_1 + \varepsilon^2({D_1}^2 + 2D_0 D_2) + \ldots \quad (55)$$

$Where\ D_n = \frac{\partial}{\partial T_n}$

Substituting Eq. (55), Eq. (54), Eq. (53) and Eq. (52) into Eq. (50) and Eq. (51) and equating the coefficients of (ε) to zero and are respectively:

U-Equation:

$$O(\varepsilon^0). \quad {D_0}^2\bar{u}_0 + C21D_0{\bar{u}_0}'\bar{U}_1 + C22D_0{\bar{u}_0}''\bar{U}_2 + C31{\bar{u}_0}''{\bar{U}_1}^2 + C32{\bar{u}_0}''{\bar{U}_2}^2 - C5{\bar{u}_0}'' = 0 \quad (56)$$

$$O(\varepsilon^1). \quad {D_0}^2\bar{u}_1 + C21D_0{\bar{u}_1}'\bar{U}_1 + C22D_0{\bar{u}_1}'\bar{U}_2 + 2D_1D_0\bar{u}_0 + C31{\bar{u}_1}''{\bar{U}_1}^2 + C32{\bar{u}_1}''{\bar{U}_2}^2 + C21D_0{\bar{u}_0}'\bar{U}_1 + C22D_0{\bar{u}_0}'\bar{U}_2 - C5{\bar{u}_1}'' - {\bar{v}_0}''''{\bar{v}_0}' - C7' - \gamma - {\bar{v}_0}''{\bar{v}_0}''' + C6{\bar{v}_0}'{\bar{v}_0}'' = 0 \quad (57)$$

V-Equation:

$$O(\varepsilon^0). \quad {D_0}^2\bar{v}_0 - C7{\bar{v}_0}' + {\bar{v}_0}'''' + C21D_0{\bar{v}_0}'\bar{U}_1 + C22D_0{\bar{v}_0}'\bar{U}_2 + C31{\bar{v}_0}''{\bar{U}_1}^2 + C32{\bar{v}_0}''{\bar{U}_2}^2 - aC31{\bar{v}_0}''{\bar{U}_1}^2 - aC32{\bar{v}_0}''{\bar{U}_2}^2 = 0 \quad (58)$$

$$O(\varepsilon^1). \quad {D_0}^2\bar{v}_1 - C7{\bar{v}_1}'' + {\bar{v}_1}'''' + 2{\bar{u}_0}'{\bar{v}_0}'''' + 4{\bar{u}_0}''{\bar{v}_0}''' + 3{\bar{v}_0}''{\bar{v}_0}''' + 2{\bar{v}_0}^{3''} + 2D_0D_1\bar{v}_0 + C31{\bar{v}_1}''{\bar{U}_1}^2 + C32{\bar{v}_1}''{\bar{U}_2}^2 + 8{\bar{v}_0}'{\bar{v}_0}''{\bar{v}_0}''' + C6{\bar{u}_0}'{\bar{v}_0}'' + C6{\bar{u}_0}''{\bar{v}_0}' + CmD_0\bar{v}_0 + \frac{3}{2}C6{\bar{v}_0}^{2'}{\bar{v}_0}'' + C21D_0{\bar{v}_0}'\bar{U}_1 + C22D_0{\bar{v}_0}'\bar{U}_2 + C21D_1{\bar{v}_0}'\bar{U}_1 + C22D_1{\bar{v}_0}'\bar{U}_2 - aC31{\bar{v}_1}''{\bar{U}_1}^2 - aC32{\bar{v}_1}''{\bar{U}_2}^2 = 0 \quad (59)$$

The order zero problems for both the axial and transverse vibration of the cantilever pipe have the form of an undamped and unforced flow induced vibration problem. This will be used to estimate the linear natural frequencies and mode shapes.

3.1. Natural Frequencies and Modal Functions

Estimation of the Natural frequencies and modal function is an order zero problem that can be determined by resolving Eq. (56) and Eq. (58).

The homogeneous solution of the leading order equations Eq. (56) and Eq. (58) can be expressed as:

$$\bar{u}(x,T_0,T_1)_0 = \phi(x)_n\, exp(i\omega_n T_0) + CC \tag{60}$$

$$\bar{v}(x,T_0,T_1)_0 = \eta(x)_n\, exp(i\lambda_n T_0) + CC \tag{61}$$

Where (CC) is the complex conjugate, $\phi(x)_n$ *and* $\eta(x)_n$ are the modal functions for the axial and transverse vibrations for each mode (n) and ω_n *and* λ_n are the eigenvalues for the axial and transverse vibrations for each mode (n).The eigenvalues are complex values with complex conjugate pair of solutions. Substituting Eq. (60) and Eq. (61) into Eq. (56) and Eq. (58) results to:

$$\left(C31\bar{U}_1{}^2 + C32\bar{U}_2{}^2 - C5\right)\phi(x)_n{}'' + (C21\bar{U}_1 + C22\bar{U}_2)i\omega_n\phi(x)_n{}' - \phi(x)_n\omega_n{}^2 = 0 \tag{62}$$

$$\eta(x)_n{}'''' + \left(C31\bar{U}_1{}^2 + C32\bar{U}_2{}^2 - C7 - aC31\bar{U}_1{}^2 - aC32\bar{U}_2{}^2\right)\eta(x)_n{}'' + (C21\bar{U}_1 + C22\bar{U}_2)i\lambda_n\eta(x)_n{}' - \eta(x)_n\lambda_n{}^2 = 0 \tag{63}$$

The general solution to the ordinary differential equations Eq. (62) and Eq. (63) are expressed as:

$$\phi(x)_n = G1_n\, exp(ik_1x) + G2_n\, exp(ik_2x) \tag{64}$$

$$\eta(x)_n = H1(exp(iz_1x) + H2exp(iz_2x) + H3\, exp(iz_3x) + H4ex\, p(iz_4x) \tag{65}$$

3.1.1. Solution to axial vibration problem

Substituting Eq. (64) into Eq. (62) gives a quadratic relation of the form:

$$\left(C5 - C31\bar{U}_1{}^2 - C32\bar{U}_2{}^2\right)k^2 - (C21\bar{U}_1 + C22\bar{U}_2)i\omega_n k - \omega_n{}^2 = 0 \tag{66}$$

Solving the quadratic equation (66) for the wave numbers (k) as a function of the eigenvalue (ω_n):

$$k_1 = \omega_n\left[\frac{\frac{C21\bar{U}_1}{2} + \frac{C22\bar{U}_2}{2} + \frac{\sqrt{C21^2\bar{U}_1{}^2 + 2C21C22\bar{U}_1\bar{U}_2 + C22^2\bar{U}_2{}^2 - 4C31\bar{U}_1{}^2 - 4C32\bar{U}_2{}^2 + 4C5}}{2}}{C5 - C31\bar{U}_1{}^2 - C32\bar{U}_2{}^2}\right] \tag{67}$$

$$k_2 = \omega_n\left[\frac{\frac{C21\bar{U}_1}{2} + \frac{C22\bar{U}_2}{2} - \frac{\sqrt{C21^2\bar{U}_1{}^2 + 2C21C22\bar{U}_1\bar{U}_2 + C22^2\bar{U}_2{}^2 - 4C31\bar{U}_1{}^2 - 4C32\bar{U}_2{}^2 + 4C5}}{2}}{C5 - C31\bar{U}_1{}^2 - C32\bar{U}_2{}^2}\right] \tag{68}$$

In order to obtain the eigenvalue, Eq. (64) is substituted into the boundary conditions in Eq. (44):

$$\frac{\partial\phi(l,t)}{\partial x} = 0 \; and \; \phi(0,t) = 0 \tag{69}$$

$$G1 + G2 = 0 \tag{70}$$

$$G1k_1 i\, exp(iLk_1) + G2k_2 i\, exp(iLk_2) = 0 \tag{71}$$

In matrix form:

$$\underbrace{\begin{pmatrix} 1 & 1 \\ ik_1 exp(iLk_1) & ik_2 exp(iLk_2) \end{pmatrix}}_{D} \begin{pmatrix} G1 \\ G2 \end{pmatrix} = 0 \tag{72}$$

For a non-trivial solution, the determinant of (D) must varnish;

$$-ik_1\, exp(iLk_1) + ik_2\, exp(iLk_2) = 0 \tag{73}$$

Substituting Eq. (67) and Eq. (68) into Eq. (73) and solving for the eigenvalue:

$$\omega_n = \frac{2\pi n - i.ln\left(\frac{b}{a}\right)}{(a-b)L}, \qquad n = 1,2,3,\ldots \tag{74}$$

$$a = \frac{\frac{C21\bar{U}_1}{2} + \frac{C22\bar{U}_2}{2} + \frac{\sqrt{C21^2\bar{U}_1{}^2 + 2C21C22\bar{U}_1\bar{U}_2 + C22^2\bar{U}_2{}^2 - 4C31\bar{U}_1{}^2 - 4C32\bar{U}_2{}^2 + 4C5}}{2}}{C5 - C31\bar{U}_1{}^2 - C32\bar{U}_2{}^2}$$

$$b = \frac{\frac{C21\bar{U}_1}{2} + \frac{C22\bar{U}_2}{2} - \frac{\sqrt{C21^2\bar{U}_1{}^2 + 2C21C22\bar{U}_1\bar{U}_2 + C22^2\bar{U}_2{}^2 - 4C31\bar{U}_1{}^2 - 4C32\bar{U}_2{}^2 + 4C5}}{2}}{C5 - C31\bar{U}_1{}^2 - C32\bar{U}_2{}^2}$$

Eq. (74) is the pipe's axial vibration eigenvalue. Solving Eq. (70) and Eq. (71) gives the constants G1 and G2. Therefore, the modal function for the axial vibration of the pipe is expressed as:

$$\phi(x)_n = G1_n\, exp(ik_1 x) + G2_n\, exp(ik_2 x) \tag{75}$$

Substituting Eq. (64) into Eq. (60) yields:

$$\begin{aligned} \bar{u}(x,T_0)_0 &= \sum_{j=1}^{2} G_{jn}\, exp\left(ik_{jn}x\right) exp(i\omega_n T_0) \\ &= \sum_{j=1}^{2} G_{jn}\, exp\left(-Im\left(k_{jn}x\right) - Im(\omega_n T_0)\right) exp\big(i(\mathrm{Re}\left(k_{jn}x\right) \\ &\quad + Re(\omega_n T_0))\big) \end{aligned} \tag{76}$$

It is clear from Eq. (76) that the real part is the natural frequency and the imaginary part is the amplitude. However, a marginally negative value of the imaginary part of any of the eigenvalue (ω_n) will cause the axial displacement ($\bar{u}$) to grow exponentially in time and this signifies the onset of the system's instability.

3.1.2. Solution to Transverse Vibration Problem

Substituting Eq. (65) into Eq. (63) gives a quartic relation:

$$z^4{}_{jn} + \left(C7 - C31\bar{U}_1{}^2 - C32\bar{U}_2{}^2 + aC31\bar{U}_1{}^2 + aC32\bar{U}_2{}^2\right) z^2{}_{jn} - (C21\bar{U}_1 + C22\bar{U}_2) z_{jn}\lambda_n - \lambda^2{}_n = 0 \tag{77}$$

$j = 1,2,3,4\ and\ n = 1,2,3,4,5 \ldots$

In order to obtain the eigenvalue, Eq. (65) is substituted into the boundary conditions in Eq. (43):

$$\eta(0) = \eta^{'}(0)\ and\ \eta^{''}(L) = \eta^{'''}(L) = 0 \tag{78}$$

This gives four algebraic equations which can be expressed in matrix form as:

$$\underbrace{\begin{bmatrix} 1 & 1 & 1 & 1 \\ z_{1n} & z_{2n} & z_{3n} & z_{4n} \\ (z_{1n})^2.\exp(i.z_{1n}) & (z_{2n})^2.\exp(i.z_{2n}) & (z_{3n})^2.\exp(i.z_{3n}) & (z_{4n})^2.\exp(i.z_{4n}) \\ (z_{1n})^3.\exp(i.z_{1n}) & (z_{2n})^3.\exp(i.z_{2n}) & (z_{3n})^3.\exp(i.z_{3n}) & (z_{4n})^3.\exp(i.z_{4n}) \end{bmatrix}}_{G} \cdot \begin{bmatrix} 1 \\ H2_n \\ H3_n \\ H4_n \end{bmatrix} . H1_n = \begin{pmatrix} 0 \\ 0 \\ 0 \\ 0 \end{pmatrix}$$

For a non-trivial solution, the determinant of (G) must varnish, That is:

$$DET(G) = 0 \tag{79}$$

In order to find modal solutions of (λ), Eq. (77) and Eq. (79) must be solve simultaneously, this can be solved numerically using nonlinear numerical routine.

The mode function of the transverse vibration corresponding to the nth eigenvalue is expressed as:

$$\eta(x)_n = H1_n.[e^{x.z_{1n}.i} - (A + B + C + D) - E] \tag{80}$$

$$A = \frac{e^{x.z_{4n}.i}.\ [e^{z_{1n}.i}.(z_{1n})^3.z_{2n} - e^{z_{1n}.i}.(z_{1n})^3.\ z_{3n} - e^{z_{1n}.i}.\ z_{4n}.(z_{1n})^2.z_{2n}}{(z_{2n} - z_{4n}).(z_{3n} - z_{4n}).[e^{z_{2n}.i}.(z_{2n})^2 - e^{z_{3n}.i}.(z_{3n})^2]}$$

$$B = \frac{e^{x.z_{4n}.i}.\ [e^{z_{1n}.i}.z_{4n}.(z_{1n})^2.z_{3n} - e^{z_{2n}.i}.z_{1n}.(z_{2n})^3 + e^{z_{2n}.i}.\ z_{4n}.\ z_{1n}.(z_{2n})^2}{(z_{2n} - z_{4n}).(z_{3n} - z_{4n}).[e^{z_{2n}.i}.(z_{2n})^2 - e^{z_{3n}.i}.(z_{3n})^2]}$$

$$C = \frac{e^{x.z_{4n}.i}.\ [e^{z_3.i}.z_{1n}.(z_{3n})^3 - e^{z_3.i}.z_{4n}.z_{1n}.(z_{3n})^2 + e^{z_{2n}.i}.(z_{2n})^3.z_{3n}}{(z_{2n} - z_{4n}).(z_{3n} - z_{4n}).[e^{z_{2n}.i}.(z_{2n})^2 - e^{z_{3n}.i}.(z_{3n})^2]}$$

$$D = \frac{e^{x.z_{4n}.i}.\ [-e^{z_{2n}.i}.z_{4n}.(z_{2n})^2.z_{3n} - e^{z_3.i}.z_{2n}.(z_{3n})^3 + e^{z_3.i}.z_{4n}.z_{2n}.(z_{3n})^2}{(z_{2n} - z_{4n}).(z_{3n} - z_{4n}).[e^{z_{2n}.i}.(z_{2n})^2 - e^{z_{3n}.i}.(z_{3n})^2]}$$

$$E = \frac{e^{x.z_{2n}.i}.(z_{1n} - z_{4n}).[e^{z_1.i}.\ (z_{1n})^2 - e^{z_3.i}.(z_{3n})^2]}{(z_{2n} - z_{4n}).\ [e^{z_2.i}.(z_{2n})^2 - e^{z_3.i}.(z_{3n})^2]} + \frac{e^{x.z_3.i}.(z_{1n} - z_{4n}).[e^{z_{1n}.i}.\ (z_{1n})^2 - e^{z_2 i}.(z_{2n})^2]}{(z_{3n} - z_{4n}).\ [e^{z_2.i}.(z_{2n})^2 - e^{z_3.i}.(z_{3n})^2]}$$

Substituting Eq. (65) into Eq. (61) yields:

$$\bar{v}(x,T_0)_0 = \sum_{j=1}^{4} H_{jn}\, exp\left(iz_{jn}x\right) exp(i\lambda_n T_0) = \sum_{j=1}^{4} H_{jn}\, exp\left(-Im\left(z_{jn}x\right) - Im(\lambda_n T_0)\right) exp\left(i(Re\left(z_{jn}x\right) + Re(\lambda_n T_0))\right) \quad (81)$$

It can be observed from Eq. (81) that the real part is the natural frequency and the imaginary part is the amplitude. However, a marginally negative value of the imaginary part of any of the eigenvalue (λ_n) will cause the transverse displacement ($\bar{v}$) to grow exponentially in time and this signifies the onset of the system's flutter instability.

4. Numerical Solution

This section presents the numerical solutions of the governing equations for a cantilever pipe conveying steady pressurized air/water two-phase flow under thermal loading. The air density and water density are considered as 1.225 kgm^{-3} and 1000 kgm^{-3} respectively.

4.1. Axial Natural Frequency

Equation (66) relates the flow parameters, pipe properties and the linear axial natural frequency. It can be seen from the equation that the linear axial natural frequency is independent of the effect of thermal loading, pressurization and top tension. However, variations in the flow velocities and the flexibility of the pipe will alter the linear axial natural frequencies. From equation (74), analytical solutions of the axial complex frequencies are solved for varying velocity and plotting the Argand diagram of the imaginary against the real for the various velocities, Figure 2 and 3 are obtained.

Individual velocity is considered for single phase flow while mixture velocity is considered for two phase flows. Adopting the Chisholm empirical relations as presented in equations (45) to (49), the slip ratio is estimated for the selected void fraction of 0.3 and the mixture velocity is disintegrated into the component velocities in the motion equation (66).

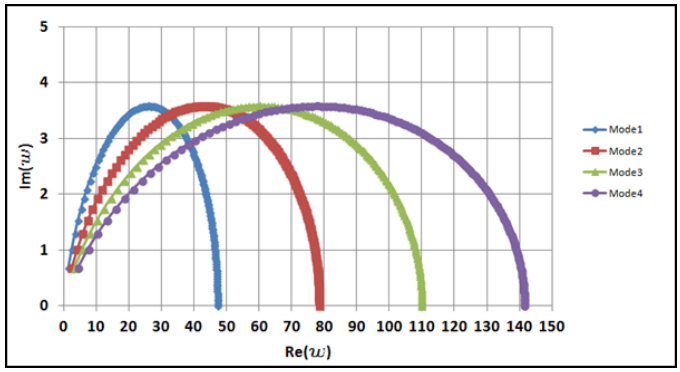

Fig. 2 First four modes axial dimensionless complex frequency as a function of dimensionless single phase flow velocity for β=0.2 and Π1=100

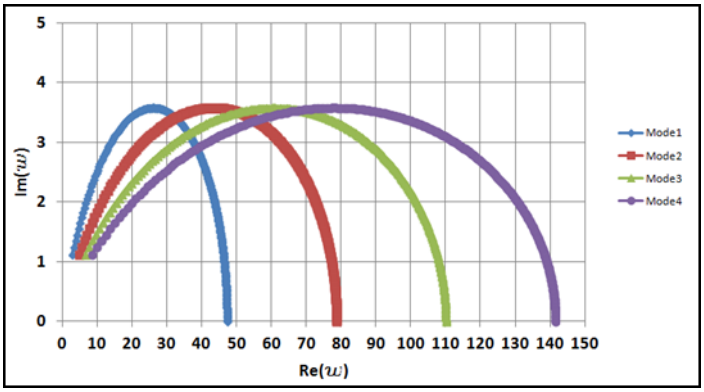

Fig. 3 First four modes axial dimensionless complex frequency as a function of dimensionless two phase flow mixture velocity for β (liquid) =0.19998, ψ (liquid) =0.9995, β (gas) =0.000105, ψ (gas) =0.0005, void fraction =0.3 and Π1=100.

For both the single phase and two phase flow, the flow velocity is used as a parametric variant gradually increasing from zero. At zero velocity, the natural frequency is that of a cantilever beam with the fluid mass as added mass. The path of the Argand diagram has a similar trend. As the fluid velocity tends towards the critical velocity; all the paths move towards the origin of the Argand diagram, which is similar to the observation by Kuiper [19].

From equation (66), the two phase flow critical velocity can be expressed as:

$$Vc = \sqrt{\frac{C5(S+1)}{C32.S^2 + C31}} \tag{83}$$

Single phase Vc can be recovered by setting S=0, which is seen to have a lesser value as compared with the two phase critical velocity.

As explained earlier, the system will be linearly unstable if the imaginary part of any of the Eigen-frequencies is less than zero. The results show that all paths possess a positive imaginary part. This signifies a stable system for flow velocities lesser than the critical velocity for a pipe discharging fluid. Comparing the Argand diagrams, it can be observed in Figure 3 that for a two phase flow the plot points cumulates to a denser plot path which signifies that more plot points are required for the convergence of the paths of the plots to the origin as compared to single phase flow in Figure 2 with sparse plot points. This observation indicates that for cantilevered pipe conveying two phase flow, the critical velocity which signifies the onset of instability is delayed and occurs at higher velocities as compared to when the pipe is conveying single phase flow.

4.2. Transverse Natural Frequency

The transverse natural frequency of the cantilever pipe as seen in equation (77) is a function of the flow parameters, pipe properties, thermal loading, pressurization and top tension. Solving the dispersive quartic equation (77) with the condition for a non-trivial solution in equation (79) simultaneously using nonlinear numerical routine written in Matlab, the complex eigenvalues are obtained.

4.2.1. The Effect of Flow Parameters

Although not the focal topic of this study, results were obtained for a simplest system with β=0.2 and Π0=Π1=Π2=0, a=αΔT=0 for a single phase flow through the pipe and compared to previous results published by Paidoussis [20] in order to demonstrate the validity of the present study.

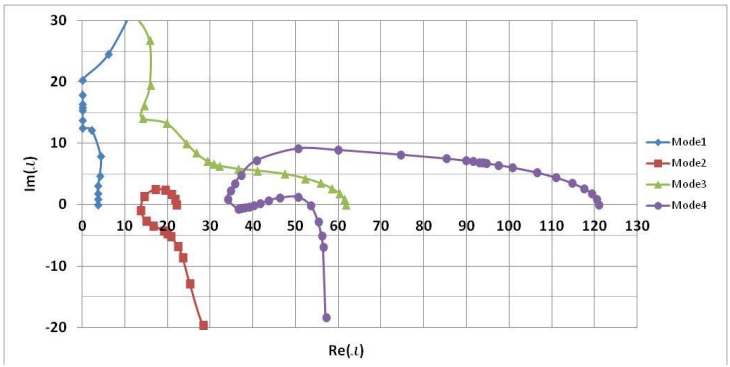

Fig. 4 First four modes transverse dimensionless complex frequency as a function of dimensionless single phase flow velocity for β=0.2 and Π0=Π1=Π2=0, a=αΔT=0

The Argand diagram presented in Figure 4 is similar to the Figure 5 obtained by Gregory & Paidoussis in 1966 as published by Paidoussis [20].

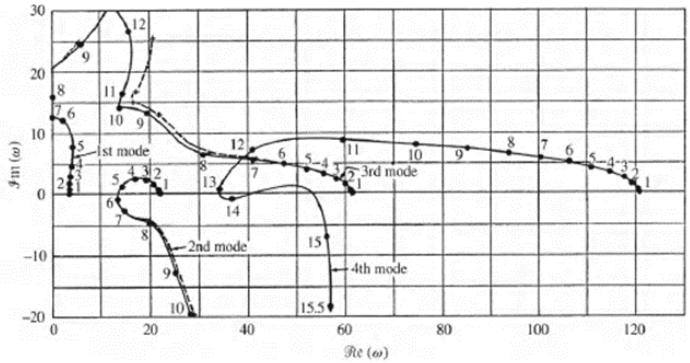

Fig 5. The dimensionless complex frequency of the four lowest modes of the cantilevered as a function of the dimensionless flow velocity, u, for β = 0.2: ——, exact analysis; – – –, four-mode Galerkin approximation [20]

Similar to the study on the axial natural frequency, the flow velocity is used as a parametric variant gradually increasing from zero. At zero velocity, the natural frequency is that of a cantilever beam with the fluid mass as added mass. However, as the velocity attains higher values, the $Im(\omega)$ in the second mode of the system starts to diminish and in time becomes negative; Therefore, a Hopf bifurcation occurs at an approximate dimensionless velocity of 5.65 which is the critical velocity at which the systems becomes transversely unstable. Also, a fourth-mode oscillatory instability is observed through Hopf bifurcation at an approximate dimensionless velocity of 13.58 as obtained by Paidoussis [20].

In this present study, various void fractions (0.1, 0.3, 0.5, 0.7 and 0.9) are considered with the corresponding slip ratios estimated from the Chisholm empirical relations presented in equations (44) and (49) the linear dynamic behavior of the two phase air and water flow is studied as follow with Π0=Π1= Π2=0, a=αΔT=0:

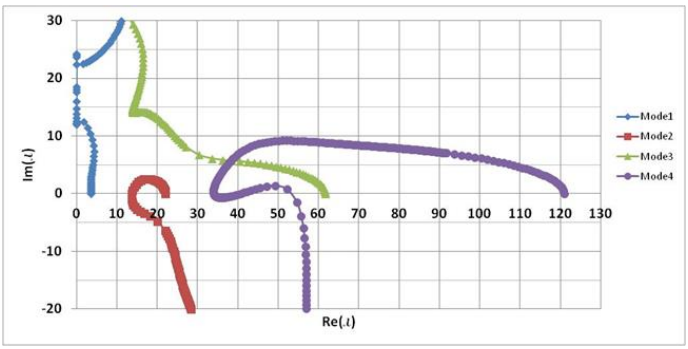

Fig. 6 First four modes transverse dimensionless complex frequency as a function of dimensionless two phase flow mixture velocity for β (liquid) =0.19999, ψ (liquid) =0.99986, β (gas) =0.0000272, ψ (gas) =0.00014, void fraction =0.1

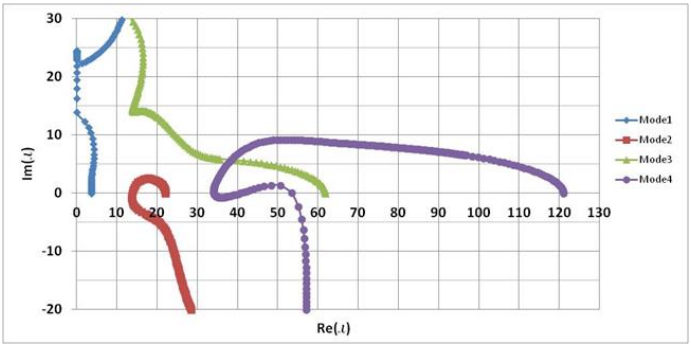

Fig. 7 First four modes transverse dimensionless complex frequency as a function of dimensionless two phase flow mixture velocity for β (liquid) =0.19998, ψ (liquid) =0.99948, β (gas) =0.000105, ψ (gas) =0.00052, void fraction =0.3

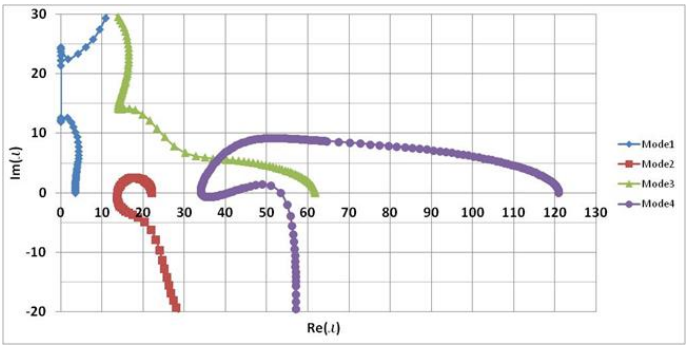

Fig 8 First four modes transverse dimensionless complex frequency as a function of dimensionless two phase flow mixture velocity for β (liquid) =0.19995, ψ (liquid) =0.99878, β (gas) =0.000245, ψ (gas) =0.00122, void fraction =0.5

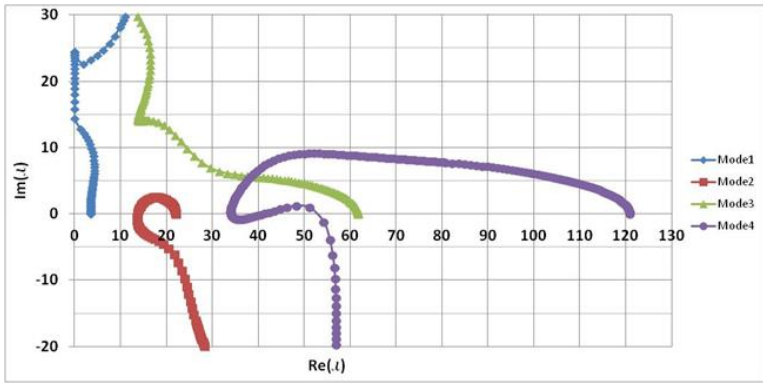

Fig. 9 First four modes transverse dimensionless complex frequency as a function of dimensionless two phase flow mixture velocity for β (liquid) =0.19989, ψ (liquid) =0.99715, β (gas) =0.0005713, ψ (gas) =0.00285, void fraction =0.7

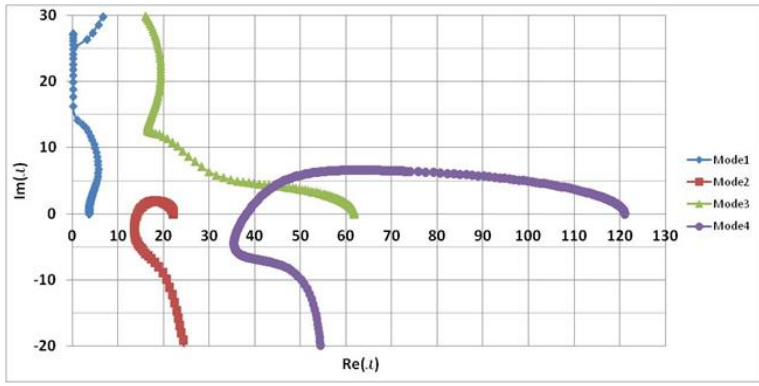

Fig. 10 First four modes transverse dimensionless complex frequency as a function of dimensionless two phase flow mixture velocity for β (liquid) =0.19956, ψ (liquid) =0.98910, β (gas) =0.0022, ψ (gas) =0.0109, void fraction =0.9.

Similar to the trend observed in Figure 4 for a single phase flow, Figure 6 to Figure 10 reveals that for the various void fractions considered, Hopf bifurcation occurred at the second mode which signifies the onset of instability transversely, the velocities at which this occurred is the critical velocity for the various void fractions. In addition, oscillatory instability is observed through Hopf bifurcation for the fourth-modes for void fractions 0.1, 0.3, 0.5 and 0.7 as revealed in Figure 6 to Figure 9, the implication of this is that for these void fractions, the fourth mode, the pipe loses stability and regains it and loses it again at some velocities. However, this did not occur in when the void fraction is 0.9 as shown in Figure 10, at the forth mode the pipe loses stability and did not regain it again.

Table 1: Summary of the dimensionless critical velocities for various void fractions

Void Fraction	Slip ratio	Dimensionless Mode 2 Hopf bifurcation velocity (Critical Velocity)	Dimensionless Mode 4 Hopf bifurcation velocity	Dimensionless Superficial critical velocity		Dimensionless critical velocity	
				Liquid	Gas	Liquid	Gas
0.1	1.057	11.502	27.392	6.213	59.104	5.592	5.910
0.3	1.237	12.505	29.782	7.988	23.046	5.591	6.914
0.5	1.616	14.613	34.804	11.173	18.053	5.587	9.026
0.7	2.685	20.382	48.524	18.436	21.216	5.531	14.851
0.9	8.351	35.338	86.671	37.791	35.065	3.779	31.559

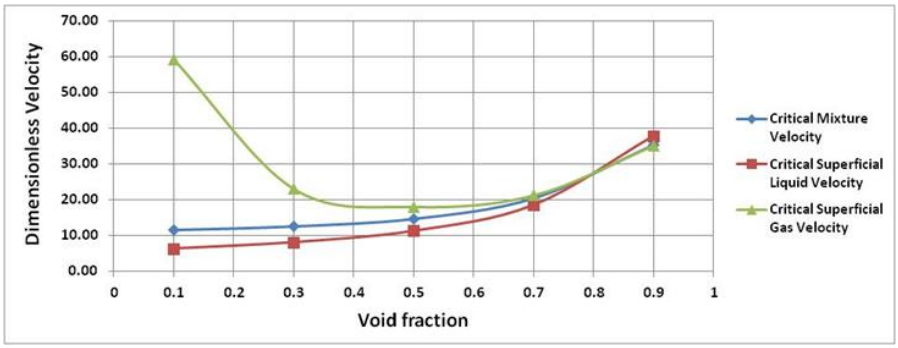

Fig. 11 Dimensionless superficial critical velocities for various void fraction

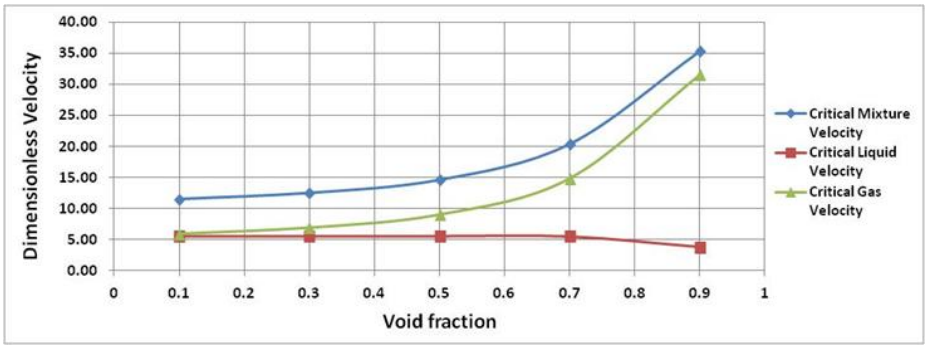

Fig. 12 Dimensionless critical velocities for various void fractions

Figure 11 and Figure 12 show that the attainment of the critical mixture velocity is delayed as the void fraction increases. Comparing the obtained critical velocity of the pipe conveying single phase flow as obtained in Figure 4 to that obtained for the various void fractions, it can be seen that the presence of the two phase flow delays the attainment of the critical velocity. This can be attributed to the fact that all the velocity dependent terms increases for a two phase flow as compared to a single phase flow (Centrifugal term and the Coriolis term). However the Coriolis term is a damping term Paidoussis [20], the additional Coriolis damping imposed by the two phase flow damps the system and makes the critical velocity of the two phase flow higher than that of a single phase flow. Also, this term increases as the void fraction increase and accounts for the increase in the value of the critical velocity as the void fraction increases.

4.2.2. The Effect of Pressurization

The effect of the pressure term is seen to make the second mode Hopf bifurcation to occur at a lower dimensionless mixture velocity of 8.238 as seen in Figure 13 as compared to the dimensionless critical mixture velocity of 12.505 obtained in Figure 7. As seen in equation (78) it is obvious that the pressure term acts similarly to the centrifugal term (MU^2) and contributes to the buckling force which hastens the onset of instability of the pipe. This observation is in line with Paidoussis [20], which highlighted that given sufficient pressurization, divergence may be induced by pressure alone.

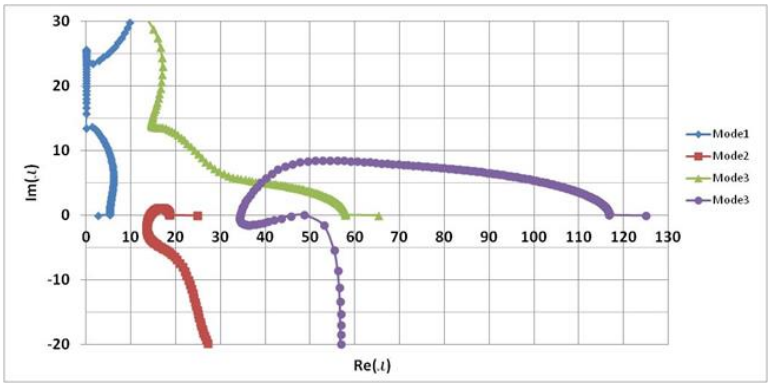

Fig. 13 First four modes transverse dimensionless complex frequency as a function of dimensionless two phase flow mixture velocity for β (liquid) =0.19998, ψ (liquid) =0.99948, β (gas) =0.000105, ψ (gas) =0.00052, void fraction =0.3, Π2 =10, Π1=Π0=a=αΔT=0

4.2.3. The Effect of Top Tension

The effect of tension term can be in two ways, depending on if it is positive or negative. A tension value less than zero indicates a compressing effect which will contributing to the buckling force in the same manner as pressurization, However, for values of tensions higher than zero as depicted in Figure 14, the observed trend is opposite to that of the pressurization effect. The positive tensioning effect is observed to have delayed the attainment of the onset of instability to a higher dimensionless mixture critical velocity of 15.637 as compared to the dimensionless critical mixture velocity of 12.505 obtained in Figure 7.

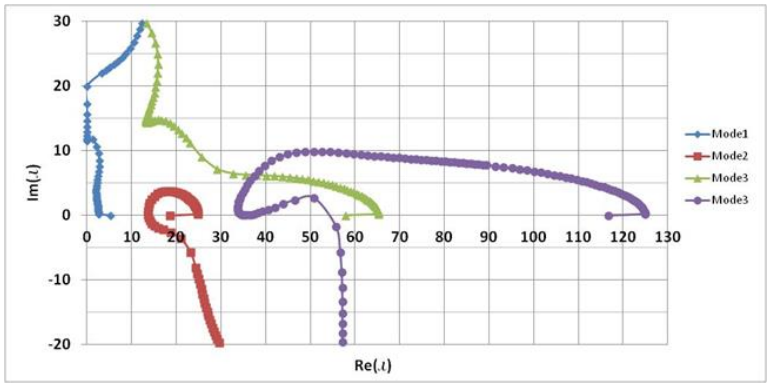

Fig. 14 First four modes transverse dimensionless complex frequency as a function of dimensionless two phase flow mixture velocity for β (liquid) =0.19998, ψ (liquid)

=0.99948, β (gas) =0.000105, ψ (gas) =0.00052, void fraction =0.3, Π0 =10, Π1=Π2=a=αΔT=0

4.2.4. The Effect of Thermal Loading

Linearly, the effect of thermal loading is akin to that of pressurisation, it can be observed from equation (78) that thermal loading term will also contribute to the buckling force and this will aid the divergence of the pipe. Figure 15 shows that the onset of instability occurred at a lower dimensionless critical velocity of 7.071 as compared to the dimensionless critical mixture velocity of 12.505 obtained in Figure 7. This corroborates the softening effect highlighted by Marakala et al [9].

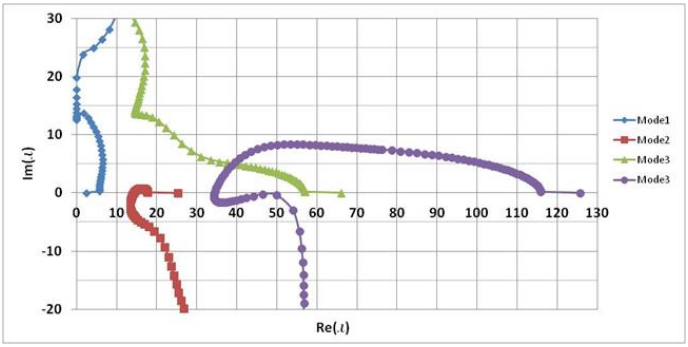

Fig. 15 First four modes transverse dimensionless complex frequency as a function of dimensionless two phase flow mixture velocity for β (liquid) =0.19998, ψ (liquid) =0.99948, β (gas) =0.000105, ψ (gas) =0.00052, void fraction =0.3, α=0.002, ΔT=60, Π1 =100, Π0=Π2=a=0

4.2.5. The Effect of Poisson Ratio

Figure 16 show that the modelling the effect of Poisson ratio delays the instability of the pipe. The dimensionless critical velocity is obtained to be 14.576 which is a higher velocity as compared to the dimensionless critical mixture velocity of 12.505 obtained in Figure 7. Also, the 4th mode Hopf bifurcation disappears with inclusion of the Poisson ratio.

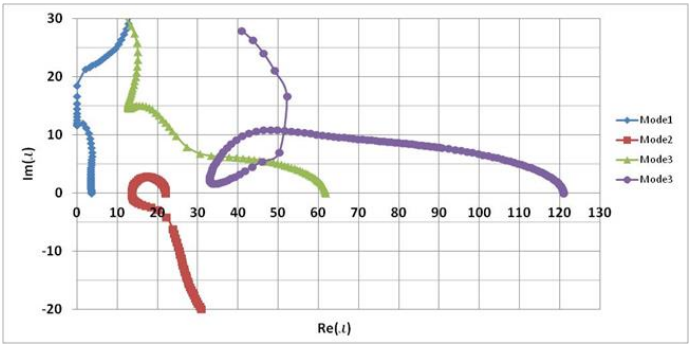

Fig. 16. First four modes transverse dimensionless complex frequency as a function of dimensionless two phase flow mixture velocity for β (liquid) =0.19998, ψ (liquid) =0.99948, β (gas) =0.000105, ψ (gas) =0.00052, void fraction =0.3, α=0, ΔT=0, Π1 = Π0=Π2=0, a=0.3.

Table 2: Summary of the effect of various parameters on critical flow velocity

Cases	Dimensionless Mode 2 Hopf bifurcation velocity (Critical Velocity)	Dimensionless Mode 4 Hopf bifurcation velocity	Dimensionless Superficial critical velocity		Dimensionless critical velocity	
			Liquid	Gas	Liquid	Gas
Mass parameters only	12.505	29.782	7.988	23.046	5.591	6.914
Effect of Pressurization	8.238	28.280	5.262	15.182	3.683	4.555
Effect of Top Tension	15.637	34.025	9.988	28.818	6.992	8.645
Effect of Thermal Loading	7.071	27.991	4.517	13.032	3.162	3.909
Effect of Poisson ratio	14.576	NA	9.310	26.862	6.517	8.059

5. Conclusion

The uniqueness and contribution of this work is the derivation of the governing equations and the study of the fluid elastic instability behaviour of extensible cantilever pipes conveying multiple phase flow as compared to previous works on pipes conveying single phase flows. This study examines the instability of a top tensioned cantilever pipe conveying pressurized two phase flow. Taking into consideration the extensible theory, nonlinear equations of motion and boundary conditions were obtained for a cantilever pipe conveying multiple phase flow using Hamilton's principle. The equations were made to be non-dimensional so as to remove the dependence on geometric and dimensional parameters. Using the method multiple scale perturbation technique, approximate solutions were obtained for a case study of a cantilever pipe conveying two phase flow of gas and liquid mixture. The leading order equation is a linear equation with the form of an undamped and unforced flow induced vibration problem. Resolution of the leading order equation resulted to the development of analytical scheme for estimating the axial and transverse natural frequencies. Numerical calculations were done to find the first four axial and transverse natural frequencies; Argand diagrams were generated for varying flow velocities. In order to assess the validity of the study, single phase results were compared with results in literature and the comparison was good. The two phase flow was modelled using the Chisholm empirical relations for various void fractions; the flow velocity was modelled as a mixture velocity accounting for the slip ratio of the phases. The axial natural frequency plot for both the single phase and two phase flow exhibits similar trends, with all the paths moving towards the origin of the Argand diagram. The velocity at which the curve intersects with the abscissa is the critical velocity of the axial vibration, which was observed to have a higher value for two phase flow as compared with the single phase flow. For the transverse natural frequencies, the Argand diagrams reveals that as the increase in flow velocity progresses gradually, a value was attained when Hopf bifurcation occurred, which is considered as the transverse vibration's critical flow velocity. The attainment of this critical flow velocity was examined for various void fractions and it was observed that the attainment of the critical velocity is delayed as the void fraction increases. A study of the effect of top tension, pressurization, thermal loading and Poisson ratio reveals that the critical velocity is attained earlier when pressurization is considered, while the effect of tension is in two ways either compressing or tensioning, a value of force less than zero will create a compression effect and acts in the same way as pressurization which aids divergence while a tensioning effect will delay the attainment of the critical velocity, the linear effect of thermal loading is akin to that of pressurisation, it hastens the attainment of the critical velocity and inclusion of the Poisson ratio in the model delays the attainment of the critical velocity of the pipe similar to the tensioning effect.

References

[1] Benjamin TB. Dynamics of a system of articulated pipes conveying fluid. I. Theory. Proceedings of the Royal Society of London. Series A. Mathematical and Physical Sciences 261; 1961:457–486. https://doi.org/10.1098/rspa.1961.0090

[2] Benjamin TB. Dynamics of a system of articulated pipes conveying fluid. II. Experiments. Proceedings of the Royal Society of London. Series A, Mathematical and Physical Sciences 261; 1961:487–499. https://doi.org/10.1098/rspa.1961.0091

[3] Gregory R W, Païdoussis M P. Unstable oscillation of tubular cantilevers conveying fluid. I. Theory, Proceedings of the Royal Society of London. Series A. Mathematical and Physical Sciences 293;1966:512–527. https://doi.org/10.1098/rspa.1966.0187

[4] Païdoussis M P, Issid N T. Dynamic stability of pipes conveying fluid. Journal of Sound and Vibration, 33(3); 1974: 267–294. https://doi.org/10.1016/S0022-460X(74)80002-7

[5] Shilling R, Lou Y K. An Experimental Study on the Dynamic Response of a Vertical Cantilever Pipe Conveying Fluid. Journal of Energy Resource Technology 102(3); 1980: 129–135. https://doi.org/10.1115/1.3227862

[6] Semler C, Li G X, Païdoussis M P. The Nonlinear Equations of Motion of Pipes Conveying Fluid. Journal of Sound and Vibration, 169; 1994:577–599. https://doi.org/10.1006/jsvi.1994.1035

[7] Ghayesh M H, Païdoussis M P, Amabili M. Nonlinear dynamics of cantilevered extensible pipes conveying fluid. Journal of Sound and Vibration, 332;2013:6405–6418. https://doi.org/10.1016/j.jsv.2013.06.026

[8] Qian Q, Lin W, Ni Q., Instability of Simply Supported Pipes Conveying Fluid under Thermal Loads. Mechanical Research Communications, 36;2009:413–417. https://doi.org/10.1016/j.mechrescom.2008.09.011

[9] Marakala N, Kuttan A K K, Kadoli R. Experimental and theoretical investigation of combined effect of fluid and thermal induced vibration on vertical thin slender tube. IOSR Journal of Mechanical and Civil Engineering, 2008:457-464.

[10] Miwa S, Mori M, Hibiki T. Two-phase flow induced vibration in piping systems. Progress in Nuclear Energy, 78; 2015:270–284. https://doi.org/10.1016/j.pnucene.2014.10.003

[11] Bai Y, Bai Q. Subsea Pipelines and Risers. Elsevier Science ISBN- 9780080445663, 2005.

[12] Monette C, Pettigrew M J. Fluid elastic instability of flexible tubes subjected to two – phase internal flow. Journal of Fluids and Structures, 19; 2004:943–956. https://doi.org/10.1016/j.jfluidstructs.2004.06.003

[13].B.G. Sinir Bifurcation and chaos of slightly curved pipes Mathematical and Computational Applications 15 (2010) 490–502. https://doi.org/10.3390/mca15030490

[14].M.A. Woldesemayat and A.J Ghajar, Comparison of void fraction correlations for different flow patterns in horizontal and upward inclined pipes International Journal of Multiphase Flow 33 (2007) 347–370. https://doi.org/10.1016/j.ijmultiphaseflow.2006.09.004

[15] Oz H R, Pakdemirli M. Vibrations of an axially moving beam with time-dependent velocity. Journal of Sound and Vibration, 227(3); 1999:239–257. https://doi.org/10.1006/jsvi.1999.2247

[16] Oz H R, Boyaci H. Transverse vibrations of tensioned pipes conveying fluid with time-dependent velocity. Journal of Sound and Vibration, 236(3); 2000:259–276. https://doi.org/10.1006/jsvi.2000.2985

[17] Oz H R, Evrensel C A. Natural frequencies of tensioned pipes conveying fluid and carrying a concentrated mass. Journal of Sound and Vibration, 250(2); 2002:368–377. https://doi.org/10.1006/jsvi.2001.3764

[18] Kesimli A, Bağdatlı S M, Çanakcı S. Free vibrations of fluid conveying pipe with intermediate support. Research on Engineering Structures and Materials, 2(2); 2016:75–87.
[19] Kuiper G L. Stability of offshore risers conveying fluid. Eburon Academic Publishers, ISBN-9789058722361,2008.
[20] Païdoussis M P. Fluid-Structure Interactions: Slender Structures and Axial Flow Vol. 1, Elsevier Academic Press, London, ISBN- 9780125443616, 2003.

CONTENT

R E S M

www.jresm.org

Research on Engineering Structures & Materials

Published by
MIM RESEARCH GROUP